8-28-2012

Indirect detection signals beyond the simplest supersymmetric dark matter

Katherine Richardson

Recommended Citation

Richardson, Katherine. "Indirect detection signals beyond the simplest supersymmetric dark matter." (2012).
https://digitalrepository.unm.edu/phyc_etds/58

Katherine Richardson

Candidate

Physics & Astronomy

Department

This dissertation is approved, and it is acceptable in quality and form for publication:

Approved by the Dissertation Committee:

Dr. Rouzbeh Allahverdi, Chairperson

Dr. Alexander Friedland

Dr. Michael Gold

Dr. Julia Fulghum

Dr. Dinesh Loomba

Dr. Mousumi Roy

Indirect Detection Signals Beyond the Simplest Supersymmetric Dark Matter

by

Katherine Anne Richardson

B.S., California Institute of Technology, 2005
M.S., University of California at Irvine, 2008

DISSERTATION

Submitted in Partial Fulfillment of the
Requirements for the Degree of

Doctor of Philosophy
Physics

The University of New Mexico

Albuquerque, New Mexico

July 2012

Dedication

The work of this thesis could not have been completed in happiness without the loving support of many friends and family, but its dedication is:

To Ralph and Jeanette Richardson

For believing in the wonder of the world, books and me for as long as I can remember.

Acknowledgments

This work was supported by a Graduate Research Fellowship from the New Mexico Space Grant Consortium and a grant from the Institute of Geophysics and Planetary Physics at Los Alamos National Laboratory.

The author wishes to thank Drs. Bernd Bassalleck, Bernard Becker, Tyce DeYoung, Arman Esamili, Yasaman Farzan, Doug Fields, Alexander Friedland, Michael Gold, Paolo Gondolo, Francis Halzen, Spencer Klein, Robert Lauer, Danny Marfatia, John Matthews, Irina Mocioiu, Ylva Pihlström, Stefano Profumo, Carsten Rott, Pearl Sandick, Jennifer Siegal-Gaskins and Greg Taylor for valuable discussions relating to this work.

The author is grateful to her collaborators and mentors who include Drs. Rouzbeh Allahverdi, Bhaskar Dutta and Yudi Santoso with whom Chapter 3 and 4 were previously published in Physical Review D [1] and Physics Letters B [2]. Chapter 5 was created from a close collaboration with Drs. Rouzbeh Allahverdi, Sascha Bornhauser and Bhaskar Dutta and was published in Physical Review D [3]. Chapter 6 is from work published in Physical Review D completed with Dr. Rouzbeh Allahverdi [4].

The author extends her gratitude to Drs. Alexander Friedland, Julia Fulghum, Michael Gold, Dinesh Loomba and Mousumi Roy for agreeing to serve on her dissertation committee and for their careful review of this work.

The author also wishes to thank the dedicated professors who have been instrumental in the preparation for my PhD pursuit, especially Drs. Jonas Schultz (Particle Physics), Myron Bander (Quantum Field Theory), Yuri Shirman (Supersymmetry) and Dinesh Loomba (Cosmology).

Life as a graduate student in the Physics & Astronomy building was made infinitely easier by the following dedicated staff: Alisa Gibson, Jaye Jensen, Sandra Ortiz, Daniel Sandoval and Lina Sandve.

Eternal gratitude is reserved for Dr. Rouzbeh Allahverdi, who has been unwavering in providing his time, support, patience and encouragement from my arrival at UNM until now. It has been an honor and a pleasure to learn from and work with Dr. Allahverdi. He taught me the methodological practice of physics research that will carry me throughout my career. I could not have been blessed with a better mentor.

The author is particularly indebted to the dedicated students of the Graduate and Professional Student Association who, through their examples and friendship, have provided my true higher education.

Finally the author wishes to express her constant love to Ryan McDaniel without whom there could be no fullness of time.

Indirect Detection Signals Beyond the Simplest Supersymmetric Dark Matter

by

Katherine Anne Richardson

B.S., California Institute of Technology, 2005
M.S., University of California at Irvine, 2008

Ph.D., Physics, University of New Mexico, 2012

Abstract

Indirect detection of gamma rays, neutrinos and charged cosmic rays from dark matter annihilation sheds light on the identity of dark matter and compliments direct detection and collider dark matter searches. By testing for the annihilation rate as well as the elastic scattering cross section of dark matter and nucleons, indirect detection can probe beyond the standard neutralino dark matter candidate. In particular, annihilation product phenomenology is a tool for the exploration of the dark matter connection to the neutrino sector. The well-motivated $U(1)_{B-L}$ extension of the Minimal Supersymmetric Model (MSSM) naturally includes the neutrino sector to explain neutrino masses and mixings. Two new $B-L$ dark matter candidates arise: the right-handed sneutrino and a new neutralino. These each annihilate preferentially into leptons by virtue of the $B-L$ charges. Chapters 3 and 4 show that the annihilation cross-section in either case can achieve a Sommerfeld enhancement that fits data from the PAMELA satellite showing an excess in the positron fraction but no excess in the antiproton spectrum. Chapter 5 demonstrates that the IceCube neutrino telescope can distinguish the annihilation of the right-handed sneutrino candidate into monochromatic neutrinos. In general, final states provide a distinctive signature that can discriminate among classes of dark matter models. Chapter 6 considers a model-independent study of monochromatic neutrino signals. Even with the current energy reconstruction capability, IceCube/DeepCore can detect gauge boson or tau annihilation even in the presence of monochromatic neutrino annihilation given ten years of data. Finally, tau regeneration is found to be a potential mechanism for differentiating neutrino flavor final states from one another.

Contents

List of Figures

List of Tables

Chapter 1

Introduction to Dark Matter

1.1 Overview

The nature of dark matter is one of the major outstanding questions in modern physics. The term dark matter was first coined to name a scientific unknown. The mass calculated from measuring the luminosity of stars and hot gas does not equal the observed total mass of galaxies and galaxy clusters. The difference earned the name dark matter, whatever that non-luminous matter in galaxy clusters and galaxies might be. Precise measurements of the Cosmic Microwave Background (CMB) now reveal that about 24% of the energy density of the universe must be non-baryonic, comprised of some cold, pressureless matter that does not interact with or produce light the way that familiar matter does [5]. The CMB indicates that this mysterious matter is five times as prevalent in the universe as baryonic matter, and yet there is not a satisfactory explanation of what dark matter actually is. In other words, physics has no explanation for roughly five out of every six units of matter in the universe.

The search for an explanation of dark matter presents a mesmerizing contrast of physical length and time scales. The search is informed both by measurements of galaxy cluster masses (10^{22} m across) and the temperature map of quantum fluctuations that imprinted themselves on the universe thirteen billion years ago.[1] But while the evidence for dark matter comes from large-scale gravitational measurements, it ultimately points toward a particle explanation of the excess of non-luminous matter. The largest scales and oldest times of the universe suggest searches for the heaviest (1TeV) and smallest (10^{-21} m) particles yet discovered.

While the total mass of non-baryonic dark matter in the universe has been measured by observing the Comsic Microwave Background, the mass of an individual dark matter particle is still unknown, and the range of possible candidates extends

---

[1] At the time of the Comsic Microwave Background, the universe was about the size of an atom.

from 10^{-6} eV (axions) to several solar masses (primordial black holes). Supersymmetry, a well-motivated particle theory, independently predicts the existence of a stable particle that interacts weakly with light and could explain the observed abundance of dark matter. This dissertation focuses on the weak scale mass range ($\sim$ 100 GeV to a TeV), the range at which new physics beyond the Standard Model is expected.

Physicists hope to confirm the existence of particle dark matter in the lab. Recent experiments have placed tantalizing constraints on dark matter properties in the mass range indicated by supersymmetry and nearing astrophysically expected annihilation rates, further motivating this research. This dissertation joins major efforts in the field of particle phenomenology to predict values for the strength with which dark matter interacts with standard model matter and to explain experimental indications of the frequency with which DM self-annihilates or decays.

When two dark matter particles annihilate, the energy of their mass ($E = mc^2$) goes into the creation of new particles. The indirect detection of dark matter seeks to detect Standard Model annihilation products and deduce properties of dark matter from the observed properties of the annihilation products. This dissertation studies the phenomenology from three types of standard model particles produced in such annihilations: gamma rays, charged cosmic rays and neutrinos.

Before discussing the phenomenology associated with these annihilations, we shall seek to establish the persuasive evidence for the existence of dark matter and motivate why Weakly Interacting Massive Particles (WIMPs) are the leading dark matter candidates.

1.2 Why do we know Dark Matter exists?

The evidence for dark matter is well established and comes from measurements with independent and unrelated uncertainties and from a variety of length scales and times in the universe. Together this evidence creates a solid argument for the existence of non-baryonic dark matter, comprising almost a quarter of the energy-density of the universe.

1.2.1 Galaxy and Galaxy Cluster Rotation Curves

The most direct evidence for dark matter comes in the form of rotation curves tracing the velocity of stars or gas as a function of radius from the center of a galaxy. Velocities can be measured by calculating the redshift or blueshift of the emission lines from either the star or the 21-cm emission line in the case of neutral hydrogen gas. Simple Keplerian dynamics can then be used to calculate the expectated velocity by demanding that stars and gas be gravitationally bound to the galaxy, i.e. that the rotational velocity be generated by the gravitational force from the mass of the galaxy.

$$\frac{mv^2}{r} = \frac{GM(r)m}{r^2} \tag{1.1}$$

$$v = \sqrt{\frac{GM(r)}{r}}\,, \tag{1.2}$$

where $M(r)$ is the mass inside of radius r. A typical rotation curve is shown in Fig. 1.1, where the expected velocities are calculated by treating the stars and gas as black-body radiators, and calculating mass from luminosity. The luminous mass of stars and gas in the disk does not equal the total mass needed to support the high gas velocities measured.

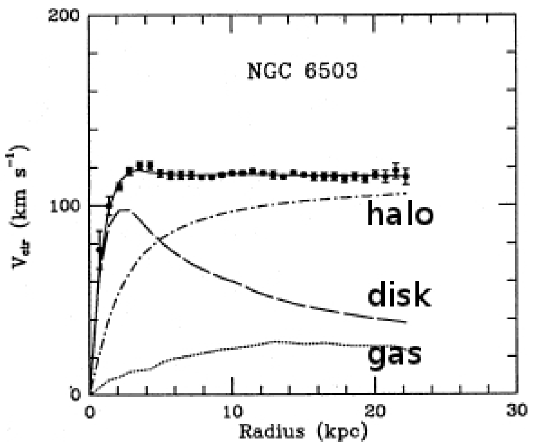

Figure 1.1: A typical spiral galaxy rotation curve for NGC 6503. The dashed line represents the visible components of a sample galaxy, the dotted line the gas contribution and the dash-dotted line the dark halo mass contribution [6].

That is, while the expectation is that the velocity curve should fall off $\propto 1/\sqrt{r}$ beyond the optical disk of the galaxy, instead the observations show a flat rotation curve, which in turn indicates that a dark halo of mass $M(r) \propto r$ gravitationally supports fast gas velocities. Typical galaxy mass-to-light ratios range from a few up to ten or so, while dwarf spheroidal galaxies, gravitational companions to the Milky Way galaxy, boast ratios of 30 to a few hundred $M_\odot/L_\odot$ and are therefore composed predominantly of dark matter.

1.2.2 Galaxy Clusters: Gravitational Lensing

Astronomy provides another direct method of measuring the mass of galaxy clusters. Light that propagates from a distant source to observers on earth will be bent and distorted by the presence of intervening matter, which warps space in accordance with Einstein's general relativity. Strong lenses appear as multiple images of a single source, whereas weak lensing only distorts a single source shape. The extent and correlation of the distortion of the shapes of these background sources can be used

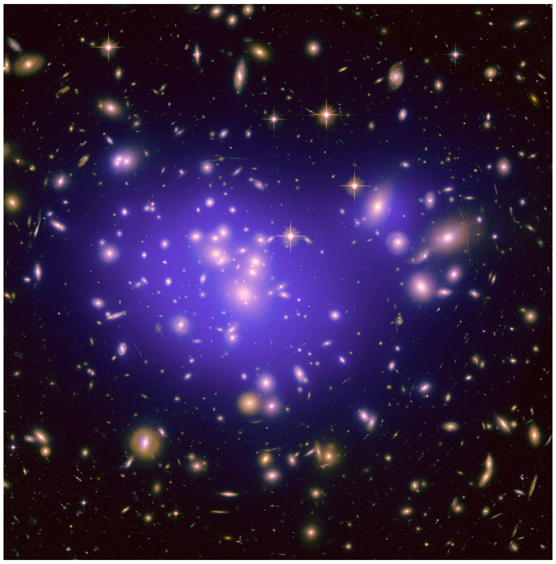

Figure 1.2: Distorted galaxies appear as arcs around galaxy cluster Abell 1689. Weak lensing reveals dark matter's contribution to the total mass of the cluster [7].

to calcualte the total intervening, lensing mass between the observer and a source. A classic example is shown in Fig. 1.2, a large galaxy cluster that lenses galaxies behind it. Weak lensing analysis reveals that dark matter contributes significantly to the total mass of the cluster.

1.2.3 Galaxy Cluster: The Bullet Cluster

The discrepancy in rotation curves between the mass deduced from gas and star luminosity and the total mass that must be present to support rotation was first observed in galaxy clusters by Fritz Zwicky in 1933 [8]. That a substantial portion of the mass in galaxies and clusters is non-luminous presents a major puzzle. Considering that rotation curves for clusters represent the largest scale test of the gravitational theory, some theories called for a modification of gravitational laws themselves rather than an introduction of dark matter. These theories were significantly challenged by a critical piece of evidence from the Bullet Cluster.

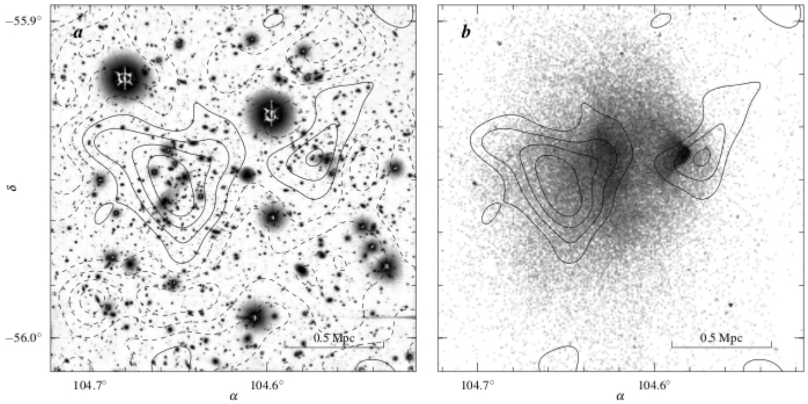

Figure 1.3: In the left panel, an overlay of mass contours from weak lensing on an optical image of the bullet cluster. In the right panel, the mass contours do not align with the X-Ray image of hot gas, showing a separation of baryonic hot gas from collisionless dark matter; from [10].

The Bullet Cluster consists of two galaxy clusters: a smaller one, the “bullet,” that has shot through and exited a larger cluster. The result is a shock wave of suddenly decelerated, hot gas, the X-rays of which were observed in 2001 [9]. Interestingly, weak lensing observations indicate that the mass of the galaxy clusters remains unaffected by the friction of the gas that underwent the shock but rather has passed through in a collisionless manner [10]. The separation of the baryonic gas and the weak lensing is shown in Fig. 1.3. Simulations have shown that the collision of dark matter and baryonic galaxy clusters would result in this configuration [11]. The Bullet Cluster shows clearly that dark matter must be collisionless and can be physically separated from baryonic gas. Modified gravitational theories are stretched to account for these observations.

1.2.4 Cosmic Microwave Background

While the evidence presented thus far indicates the existence of collisionless, non-luminous matter in halos around galaxies and in galaxy clusters, the Cosmic Microwave Background provides an opportunity to calculate the total amout of dark matter present in the universe and shows that this matter is in fact non-baryonic in addition to being non-luminous and collisionless.

At early times after the Big Bang, the universe was so hot and dense that photons could only go short distances before being absorbed or deflected by a charged particle. As the universe cooled and expanded, eventually photons could free-stream without scattering on charged particles. This surface of last scattering produced a Cosmic Microwave Background (CMB) of photons of practically uniform temperature, Fig. 1.4.

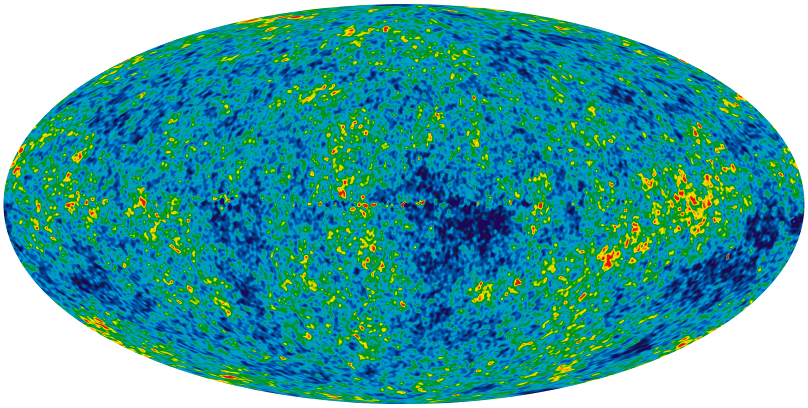

Figure 1.4: All sky seven-year temperature map from the Wilkinson Microwave Anisotropy Probe (WMAP) [12].

.

By correlating the angular size of temperature regions on the CMB sky, we can map the CMB power spectrum Fig. 1.5. These angular regions correspond to the distances over which photons had the opportunity to expand or contract. In the early universe, as gravitational structure was being created, baryonic matter that

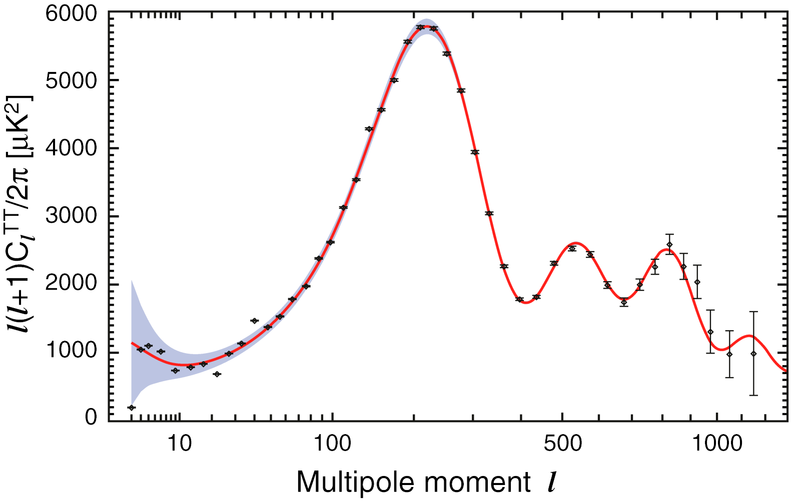

Figure 1.5: Power spectrum of the CMB, which maps the frequency of multipole moments that correspond to angular scales [13].

.

was attracted into gravitational wells would experience a pressure from photons: photons were exchanged between the matter in the well and the in-falling matter. The in-falling baryons could be prevented from creating gravitational structure; thus, photons act to erase anisotropies in structure and act in competition with the gravitational attraction of baryonic matter. This acoustic oscillation allows us to associate the first peak of the CMB with the first compression of matter into gravitational wells and measure the curvature of the universe. The second peak gives a measurement of the first expansion of matter and therefore the total baryonic matter, and the third peak can be used to infer the total amount of dark matter. From the CMB we can deduce that roughly five times as much dark matter exists as baryonic matter.

Furthermore, big bang nucleosynthesis (BBN) buttresses the observations of the CMB. Predicting the primordial abundance of light elements produced in the first few moments after the Big Bang depends heavily on the ratio of baryons to photons, which can be translated to a total number of baryons available for nucleosynthesis, see Fig. 1.6. The observations of light elements match well with the predictions and therefore support the total baryonic density measured by the CMB.

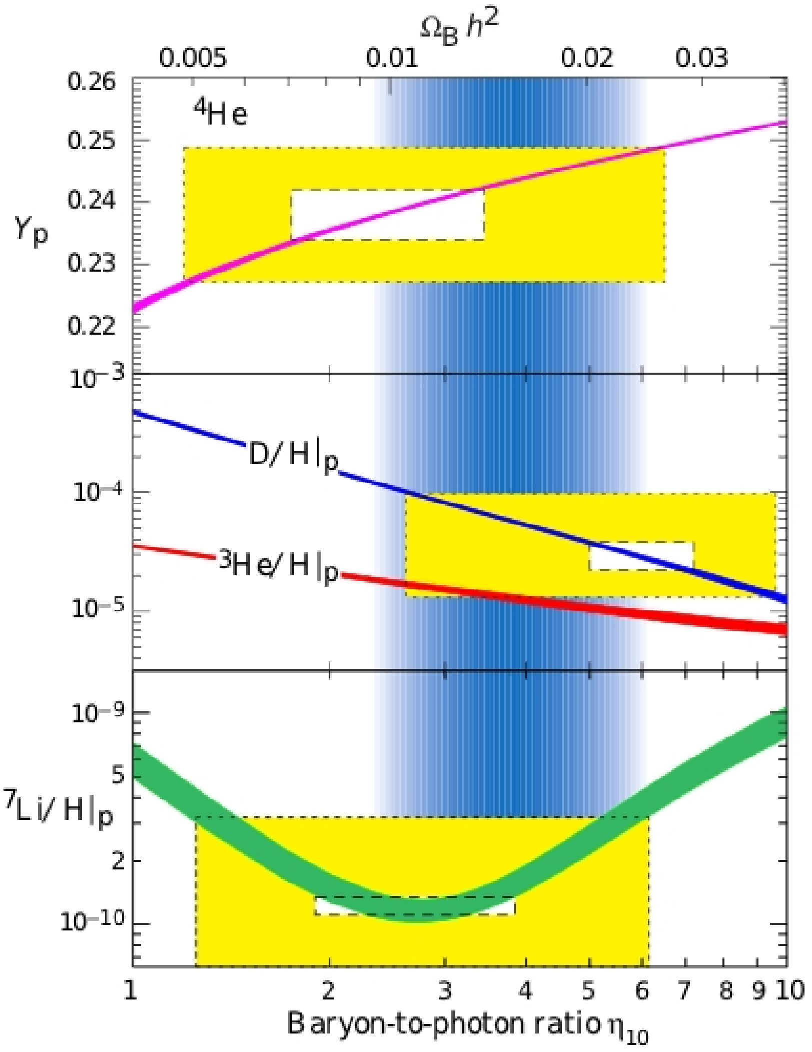

Figure 1.6: The observed primordial elemental abundances shown in boxes with two sigma error. Predicted abundances trace through these boxes and align with the observed value of Ωh^2 from WMAP7 [14].

1.2.5 Large Scale Structure

Thus, dark matter is not just non-luminous; it is also non-baryonic. It cannot experience pressure via the exchange of photons with the same strength as baryonic matter. This key lesson from the CMB is emphasized in simulations of large scale structure (LSS). At early, hot and dense times in the universe, the pressure in-falling baryons feel from photons would be extreme enough to prevent the formation of gravitational structures. This would retard the development of large scale structure by about a factor of ten compared to observations of the density of clusters and superclusters. Comparatively, non-baryonic dark matter interacts weakly with light so that dark matter decouples from photons and forms gravitational wells earlier. Later, when the universe continues to cool, baryons also decouple from photons and can join the gravitational structure dark matter has already created. A sketch of the growth of density perturbations due to the early de-coupling of dark matter appears in Fig. 1.7. The important lesson from large scale structure is that the observed extreme gravitational densities in the universe, such as superclusters, could not be explained by structure growth from baryonic gravitational wells. Instead, structure must be formed earlier, by a gravitational particle that interacts weakly with light, while baryons are still prevented from gravitationally clumping by the pressure of photons.

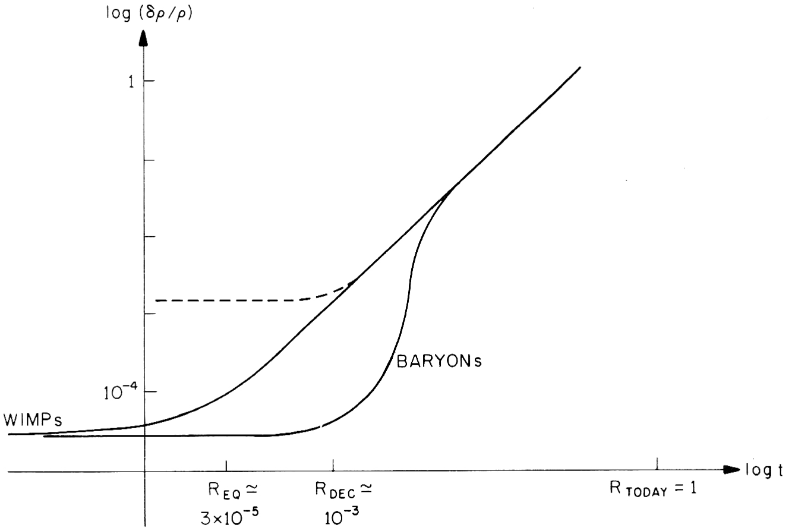

Figure 1.7: Density perturbation growth as a function of time [15]. Weakly Interacting Massive Particles (dark matter particles) decouple from photons at early times, creating gravitational structure well before baryons could. Baryons feel pressure from photons that prevent them from participating in the development of structure until later times.

1.3 What could dark matter be?

The search for a non-luminous, non-baryonic dark matter candidate seeks to provide a satisfactory explanation for all the current evidence. Many suggested candidates meet some but not all of the evidential demands. The majority of the field has elected to seek a single explanation for all of these phenomena, and we take this approach. However, it is possible that, for example, several dark matter candidates contribute to the total dark matter density indicated by the CMB. In this section, we explore some rejected as well as some viable dark matter candidates.

1.3.1 Modified Newtonian Dynamics

Since all of the observations of dark matter stem from its gravitational interactions, one may wonder whether a simple modification of the laws of gravity may explain the existing evidence. After all, as mentioned in Section 1.2.3, observations of rotation curves of galaxies and clusters are one of the largest-scale tests of gravity and therefore would be sensitive to even small deviations from Newtonian gravity. It is conceivable that at small length scales the gravitational force takes a form other than $F \propto 1/r^2$. In fact, the gravitational force has been tested to just under millimeter length scales, but not lower, allowing for terms in the gravitational potential $\propto ln(r)$. This form of the potential can successfully reproduce the flat rotation curves observed and was first suggested in 1983 [16].

Modified Newtonian Dynamics (MOND) gained some popularity as it avoided directly introducing new and unobserved particles. However, it is worth noting that any mathematical expression for force ultimately originates in the interactions of particles in the manner seen already for electromagnetism, the weak and strong force in quantum field theory. Thus, MOND does introduce additional degrees of freedom in postulating a new form for the gravitational potential.

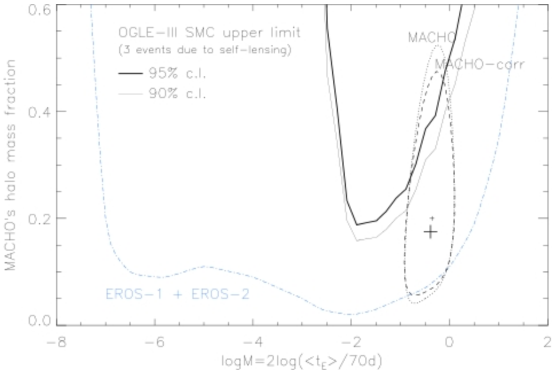

Figure 1.8: Upper limits placed on the fractional contribution of MACHOs to the halofrom MACHO, OGLE and EROS [17].

Ultimately, MOND has difficulty reproducing the dynamics observed in the bullet cluster and similar merging galaxies and cannot aid in explanations of early cosmological evidence for particulate non-baryonic dark matter, such as the CMB, LSS and BBN. While some continue to pursue MOND , it cannot provide a satisfactorily simple explanation for the entirety of the evidence.

1.3.2 Massive Compact Halo Objects

A portion of the dark matter halo density could come from dark matter halo compact objects, or MACHOs, such as black holes, neutron stars, faint old white dwarfs, brown dwarfs, planets or other objects that would contribute to gravitational evidence such as rotation curves, lensing and bullet cluster measurements. MACHOs can be detected by looking for microlensing events where a background star temporarily brightens as a foreground MACHO moves between the source and the observer. Diffuse dark matter would not produce such lensing events. The Optical Gravitational Lensing Experiment (OGLE), EROS and MACHO [17, 18] searched for such events in the Large and Small Magelllanic Clouds. Limits to the total contribution to the dark matter halo are shown in Fig. 1.8.

Thus, MACHOs cannot wholly explain the dark matter halo mass observed through galactic rotation curves. Nor can MACHOs be the sort of particulate dark matter that forms gravitational structure earlier than baryons and adds a purely gravitational contribution to the photon-baryon coupling seen in the CMB angular power spectrum. In other words, both the CMB and LSS still call for non-baryonic dark matter.

1.3.3 Standard Model Neutrinos

A natural candidate dark matter particle might be the Standard Model neutrino. Besides the virtue of being a known particle, the neutrino also neatly fits the requirement for weakly interacting with light.[2] Furthermore, neutrino oscillations among electron, muon and tau flavors demonstrate that neutrinos have non-zero mass and non-zero mixings.

Simplistic upper bounds on the total mass contribution from neutrinos can be computed by combining the upper-bounds on $m_{\bar{\nu}_e} \lesssim 2\text{eV}$ produced in tritium β-decay experiments [19] and the CMB bound on the sum of the active neutrino masses:

$$f_\nu = \frac{\Omega_\nu}{\Omega_m} = \frac{\Sigma m_\nu}{93\Omega_m h^2 \text{ eV}} \simeq 0.08\frac{\Sigma m_\nu}{1\text{eV}} \; ; \tag{1.3}$$

see [20] for details. Thus, neutrinos only account for approximately half of the total matter content of the universe, whereas dark matter must provide more than eighty percent of Ω_m. Next generation tritium decay experiment KATRIN will push the upper limit down an order of magnitude further. A table of even more stringent bounds from astrophysical evidence is shown in [20].

There is another drawback to Standard Model neutrino serving as dark matter.

---

[2] As a neutral particle, neutrino-photon interactions are suppressed by loop diagrams or by Brehmstrahlung radiation after charged current interactions.

Neutrinos can free-stream distances $d \sim T_\nu/(m_\nu H)$, where T and m are the temperature and mass of the neutrino and H is the Hubble rate. Neutrinos cannot clump at distance scales smaller than the co-moving scale d/a and thus produce a power spectrum fall-off at about 40Mpc $(m_\nu/30\text{eV})$ [19, 20]. In other words, neutrinos act to erase smaller structure and fall into the hot dark matter category [21]. Thus, larger structures in the universe would have developed early and smaller structures later, whereas the Milky Way is in fact older than the Local Group [22]. All indications show that familiar neutrinos cannot be the sole bearer of the dark matter moniker.

1.3.4 Promising candidates: sterile νs, axions, WIMPs

Having established those candidates that cannot wholly explain dark matter, a few viable, theoretically well-motivated candidates remain including sterile neutrinos, axions and WIMPs.

Introducing right-handed neutrinos to the Standard Model provides a mechanism to generate the light neutrino masses. Right-handed neutrinos have no coupling to the standard model W and Z gauge bosons and would therefore be effectively sterile other than any mixings with the left-handed neutrinos. Dodelson and Widrow proposed that sterile neutrinos can act as the dark matter in 1993 [23]. Sterile neutrinos can decay through their mixings with standard neutrinos and therefore must evade some cosmological bounds [24].

Another theoretically compelling dark matter candidate is the axion. The Peccei-Quinn solution to the strong CP problem introduces a new global U(1) symmetry the dynamical breaking of which produces a pseudo-Nambe-Goldstone boson, the axion.[3] Axions are predicted to have a mass between 10^{-6} and 1 eV. Nevertheless, axions are

---

[3] Dynamical symmetry breaking explains the lack of CP-violating terms in the QCD Lagrangian which are otherwise allowed.

produced out of equilibrium and thus may remain non-relativistic and constitute cold dark matter in sufficient quantities; see [25] for a review. The ADMX experiment has recently placed limits on the axion to photon coupling through an RF cavity search [26].

This is not a complete list of viable candidates: for a summary of WIMPzillas, primordial black holes and other exotic models, see e.g. [19]. However, the most popular solution to the dark matter problem remains the Weakly Interacting Massive Particle (WIMP), which will be the focus of the remainder of this dissertation.

1.4 Weakly Interacting Massive Particles

WIMPs experience gravitational interactions and have weak scale masses, between 100 GeV and 10 TeV or so. A number of different theories indendently include such weak scale particles since this is the mass scale at which new particles may explain the mass of the top quark. For example, supersymmetry (SUSY) introduces a supersymmetric partner or sparticle for each Standard Model particle. SUSY solves the Hierarchy Problem through radiative corrections for masses that include both particles and sparticles, thus neatly canceling the previously divergent terms that are proportional to $ln(\Lambda)$, where Λ is the scale of new physics[4], see Fig. 1.9. The expected scale of the new supersymmetric particles will naturally fall near the top mass and motivates the energy range probed by the Tevatron and now the Large Hadron Collider (LHC). WIMP mass ranges are of natural interest in searches beyond the Standard Model and are also of natural interest to the dark matter problem through the mechanism of the the WIMP Miracle.

1.4.1 Relic Density of WIMPs

The so-called WIMP miracle shows how a particle with a weak-scale mass and coupling will naturally produce the relic density of dark matter observed by WMAP. A particle species in chemical equilibrium will come to freeze out at a particular relic-density that can be calculated by solving the Boltzmann equation. Initially, the particle in equilibrium will annihilate and be created at equal rates, maintaining a constant co-moving density since

$$n_X(t) \propto \left(\frac{kT_X}{m_X}\right)^{3/2} e^{-kT/m_X} \tag{1.4}$$

---

[4] $\delta m^2 \propto \int^{\Lambda_{Pl}} \frac{d^4k}{(k^2-m^2)} \propto \Lambda_{Pl}^2$

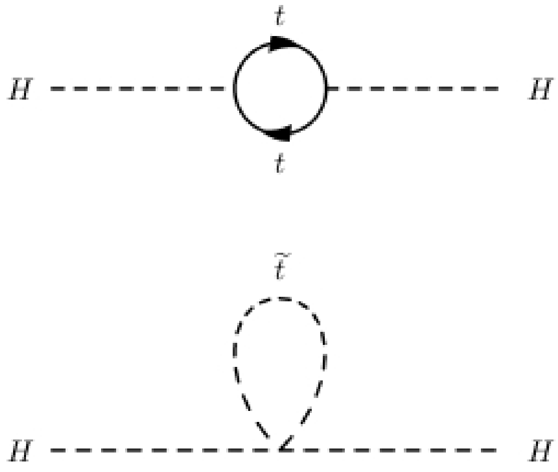

Figure 1.9: Corrections to the Higgs Mass involving the top quark and squark exactly cancel divergent contributions, solving the Hierarchy Problem and motivating supersymmetry.

and the universe at early times expands with a scale factor proportional to $T^{3/2}$. A simple way to think of this is that the universe is hot enough to ensure that the kinetic energy of annihilations are enough to produce the species with mass $m_X << T$. However, as the universe cools, eventually the temperature falls below the relevant mass, and the Boltzmann exponential suppression turns on. Particles can only annihilate and are no longer likely to be created. Finally, the expansion of the universe outpaces the exponentially falling annihilation rate.[5] In other words, the universe has become so sparse that particles can no longer find one another to annihilate. The relic density of the particle species has frozen in, to remain the same through today. This chronology is illustrated in Fig. 1.10.

A back of the envelope calculation shows the expected annihilation rate, recalling that freeze-out occurs when the annihilation rate for WIMPs approximately equals the Hubble rate:

---

[5] During matter and radiation dominated epochs the Hubble rate H(t) is a power law in temperature $H(t) \propto T^n$.

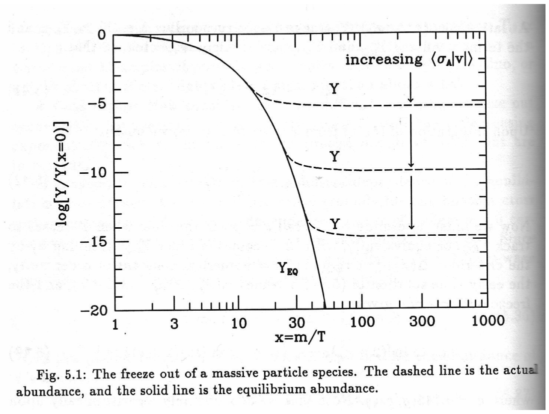

Fig. 5.1: The freeze out of a massive particle species. The dashed line is the actual abundance, and the solid line is the equilibrium abundance.

Figure 1.10: Schematic of comoving density over time for a particle species. Species begin in equilibrium but are Maxwell-Boltzmann suppressed until freeze out. Higher annihilation rates result in lower relic densities [15].

$$\begin{aligned}
\Gamma = \langle\sigma v\rangle n_f &\approx H \propto \frac{T_f^2}{M_{Pl}} \\
n_f &\approx \frac{T_f^2}{M_{Pl}\langle\sigma v\rangle} \\
n &\propto a^{-3} \propto T^3 \\
n_0 = \frac{\rho_{x,0}}{m_x} &= n_f\left(\frac{T_0}{T_f}\right)^3 = \frac{T_0^3}{M_{Pl}\langle\sigma v\rangle}\frac{1}{T_f} \\
\langle\sigma v\rangle &= \frac{T_0^3}{M_{Pl}}\frac{m_x}{T_f\rho_{x,0}} \\
\langle\sigma v\rangle &= \frac{T_0^3}{M_{Pl}}\frac{1}{20\rho_x}\ .
\end{aligned}$$

Here we use the numerical solution for the Boltzmann equation freeze-out $\frac{m_x}{T_f} \approx \frac{1}{20}$. Inserting the WMAP value for Ω_{CDM}, we discover that we should expect a WIMP annihilation rate of $3\times10^{-26}\ cm^3/s$, exactly the scale expected for weak interactions, a WIMP miracle.[6] Thus, both theoretical particle considerations and cosmological

---

[6] A few caveats to the WIMP miracle. Relic density only applies for species in equilibrium: it is possible to produce particles non-thermally. So-called WIMPless miracles have also been proposed [27].

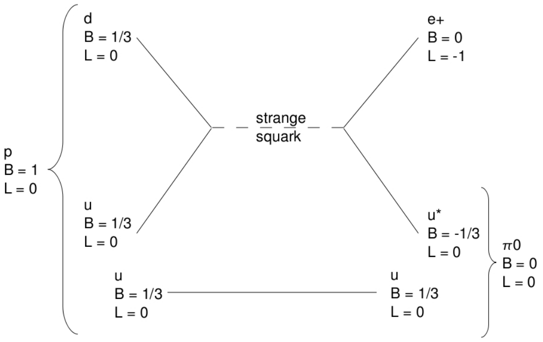

Figure 1.11: Possible supersymmetric channel for proton decay that is forbidden when R-parity is imposed.

measurements align and motivate an exploration of the weak scale.

1.4.2 WIMPs as Lightest Supersymmetric Particles

WIMPs must be stable or very long lived to explain both the density of dark matter at freeze-out measured by the CMB and the density of the Milky Way halo today. Interestingly, early in the history of supersymmetry it was realized that protons could decay through a squark s-channel too readily compared to experimental bounds on the proton lifetime, Fig. 1.11. However, if an R-parity symmetry $R = (-1)^{2s+3B+L}$ were imposed, the quantity $2s + 3B + L$ would be conserved according to Noether's theorem. Consequently, such proton decays would be forbidden.

The implication for supersymmetric dark matter is that the form of R requires that any interaction have an even number of supersymmetric particles enetering and exiting the interaction or an odd number entering and exiting. Thereofore, two supersymmetric particles may annihilate and produce Standard Model particles or one supersymmetric particle may decay into another. Therefore, the lightest supersymmetric particle (LSP) is kinematically forbidden from decaying. Motivated by protecting the lifetime of the proton, a natural WIMP candidate emerges in the

LSP. The method of breaking supersymmetry determines the nature of the LSP, which may be a sneutrino (spin-0), neutralino (spin 1/2), gravitino (spin 3/2) or axino (spin 0).

Each of these LSPs have distinct phenomenology determined by the particulars of a SUSY model, but all provide viable explanations to the dark matter problem.

1.5 How do we detect WIMPs?

Exciting prospects exist for the detection of many dark matter candidates, including axions, sterile neutrinos and some LSP WIMPs. Experimentalists hope to confirm in the laboratory the particle nature of dark matter. To do so will require observing the interaction of dark matter with standard matter. Experiments fall into three detection methods: colliders, direct and indirect detection.

1.5.1 Colliders

The Large Hadron Collider collides protons at a center-of-mass energy of 14 TeV. These collisions may be energetic enough to produce supersymmetric particles. The sparticles would undergo rapid decay until the LSP was produced. The stable LSP WIMP candidate would then exit the detector without interacting. Its presence could then be reconstructed by calculating the missing energy from the products of the collision. This missing energy corresponds directly to the mass of the WIMP. Unfortunately, many models produce missing energy in colliders, so other forms of detection will be needed to confirm the WIMP mass measurement and to confirm the astrophysical role of any particle that provides a missing energy signal. Channels of new physics constrained by colliders are model dependent and outlined in [19].

1.5.2 Direct Detection & Neutrino Telescopes: Elastic Scattering Cross Section Limits

Direct detection experiments use a target of gas (noble liquid detectors, e.g. ZEPLIN, XENON, DEAP, ArDM, WARP, LUX) or crystal (cryogenic detectors, e.g. CDMS,

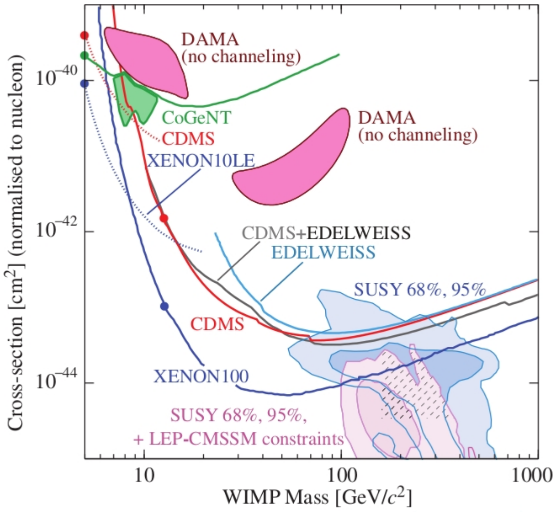

Figure 1.12: Recent upper bounds on the WIMP-nucleon spin-independent elastic scattering cross section from [28].

CRESST, EDELWEISS, EURECA) to look for energy deposited when a local [7] WIMP scatters elastically off of a nucleon in the target. Detectable signals can include ionization, scintillation, phonons or nucleation of bubbles. These experiments are low or no-background experiments and must operate underground, with shielding and clean environments to ensure no false signals from cosmic rays and radioactive impurities in gases. Annual modulation experiments such as DAMA/LIBRA look for changes in the interaction rates as the earth is moving in the same or opposite direction as the sun around the galaxy (and thus decreasing or enhancing the WIMP-nucleon rate). Directional dark matter searches use a Time Projection Chamber to look for changes during the course of the day as the laboratory aligns with or away from the direction in which the sun is traveling. The advantage of directional searches is that they can isolate a signal from an isotropic background.

In all cases, the experiments place limits on the WIMP-nucleon elastic scatter-

---

[7] There is approximately one WIMP in a volume the size of a coffee cup. The challenge is to detect it!

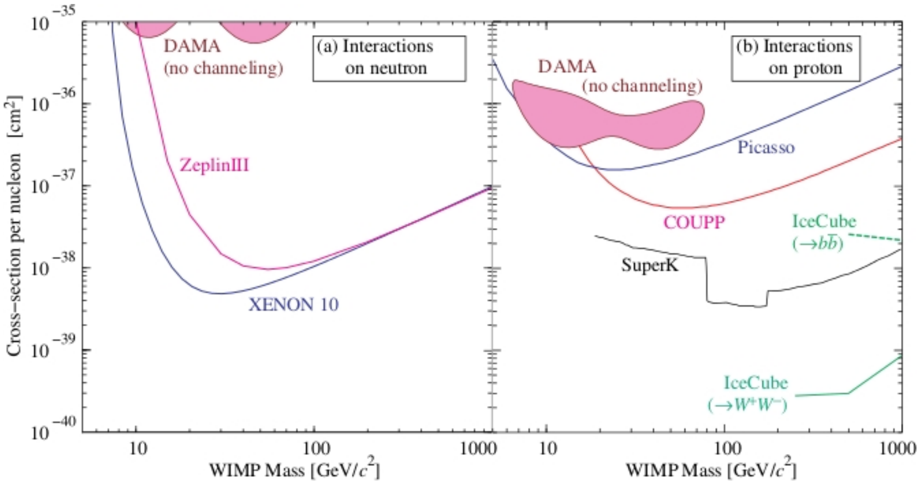

Figure 1.13: Recent upper bounds on the WIMP-nucleon spin-dependent elastic scattering cross section from [28].

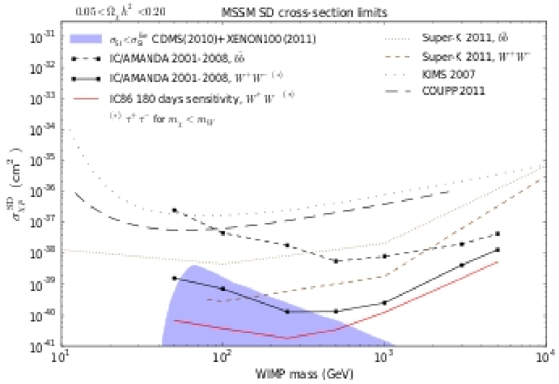

Figure 1.14: Recent upper bounds and future sensitivities of neutrino telescopes [29].

ing cross section detection. In general this cross section has both spin-dependent and spin-independent components. The best spin-independent limits are shown in Fig. 1.12. The best spin-dependent limits are actually reached by neutrino telescopes such as IceCube and Super-Kamiokande as long as the WIMP population that becomes gravitationally captured in the sun and earth comes to equilibrium. See Chapter 5 for an explanation of how these limits beat those of direct detection searches with high spin targets such as COUPP and Picasso. Recent limits on $\sigma_{SD} vs. m$ are shown in Fig. 1.13 and projected IceCube sensitivities in Fig. 1.14. The phenomenology of discovery and discrimination of dark matter candidates using neutrino telescopes to limit scattering cross sections is discussed in Chapters 5 and 6 of this work.

1.5.3 Indirect Detection: Annihilation Cross Section Limits

Indirect detection searches look for evidence of the annihilation of dark matter. Annihilation products can include charged cosmic rays such as positrons, gamma rays and neutrinos. Detecting any of these annihilation final states signals is made more difficult by the challenge of understanding the expected astrophysical background. Detection and discovery of dark matter through indirect detection relies on the analysis of the flux of standard model particles through a telescope or detector. Typically this signal is displayed as a function of energy and is referred to as a spectrum.

Chapter 2 addresses gamma ray indirect detection. While dark matter cannot be charged and cannot interact directly with light, if it annihilates and produces charged particles, those particles will emit gamma rays through synchrotron emission and Brehmmstrahlung radiation. The gamma ray telescope Fermi has been able to place upper bounds on the gamma rays produced by dark matter annihilation by doing a composite analysis of dwarf spheroidal galaxies, which have high dark matter content and relatively low astrophysical gamma ray background [31] (Fig. 2.4). Interestingly, dark matter can also produce monochromatic light through a loop diagram Fig. 1.15, and Fermi has also placed the most competetive bounds on these lines in the energy spectrum [30] (Fig. 2.2).

In 2009, PAMELA reported an excess of positrons and no excess of anti-protons; this data could be interpreted as annihilating dark matter. PAMELA data motivated the work of Chapters 3 and 4, which focus on the phenomenology of charged

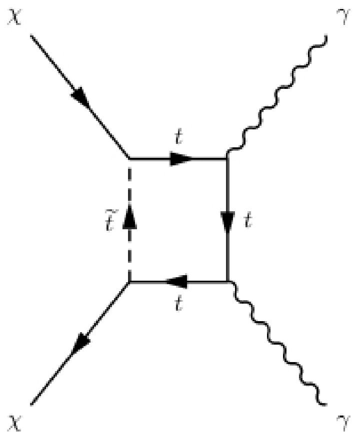

Figure 1.15: Dark matter annihilation can produce monochromatic gamma rays through a loop diagram.

cosmic rays, Fig. 1.16. Fermi, built fundamentally as a gamma ray telescope, put its tracker to creative use and placed meaningful constraints on the flux of positrons and electrons out to a region of a few kiloparsecs, Fig. 1.17.

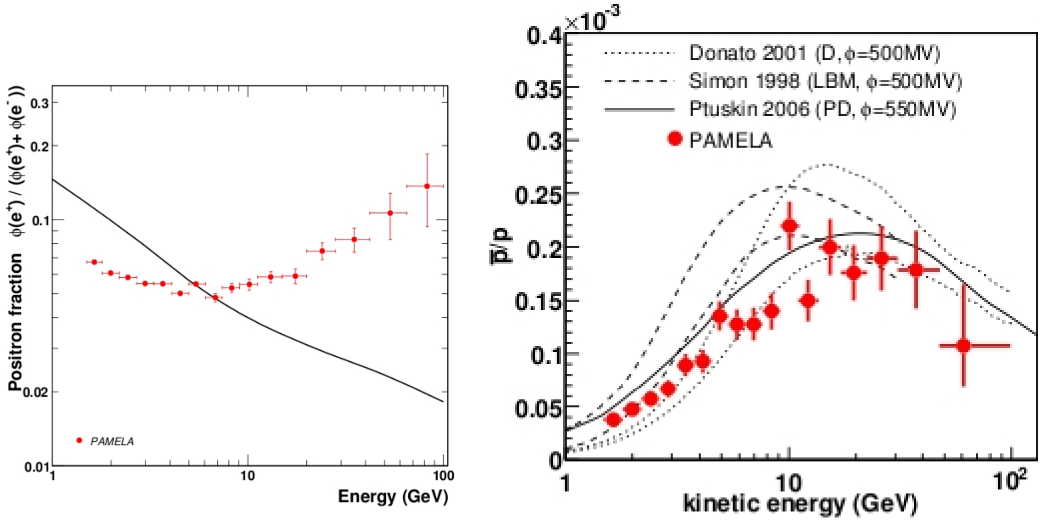

(a) Positron Excess (b) Anti-Proton Spectra

Figure 1.16: Measured flux of positrons and anti-protons compared to predicted astrophysical background. [32, 33].

Neutrino telescopes such as IceCube and Super-Kamiokande can also place limits

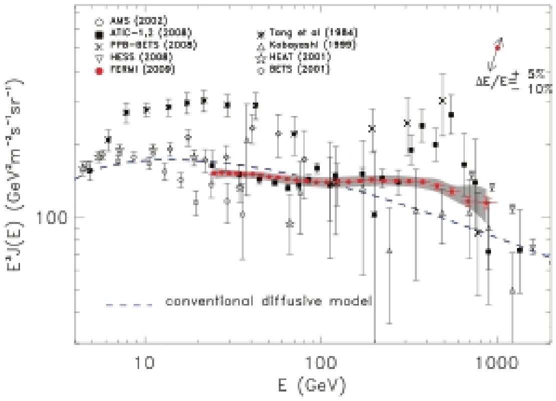

Figure 1.17: Fermi electron and positron energy spectra [34].

on the annihlation rate of dark matter particles by looking at the galactic center, rather than the equilibrated populations of WIMPs in the sun and earth. Recent bounds are shown in Fig. 1.18.

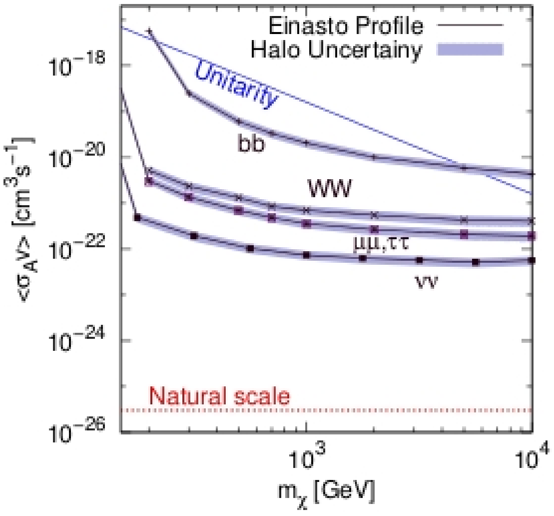

Figure 1.18: IceCube neutrino telescope upper bounds on the annihilation cross section looking toward the galactic center [35].

1.5.4 Detection Complimentarity

Ultimately, all three detection methods will inform our search for WIMPs and the nature of the WIMP-standard matter interactions in three different directions as shown in Fig. 1.19. Mass constraints from colliders may be compared to those from direct and indirect detection experiments. Direct detection experiments may confirm the existence of a particulate dark matter halo, and any scattering cross section will have implications for the scale of fine structure in dark matter halos as discussed in Chapter 2. Indirect detection experiments are already beginning to probe the annihilation rates predicted by the relic density seen by the CMB. This dissertation thus stands as a small part of the ongoing effort to predict the phenomenology of theoretically relevant models and understand the emerging evidence from indirect detection searches.

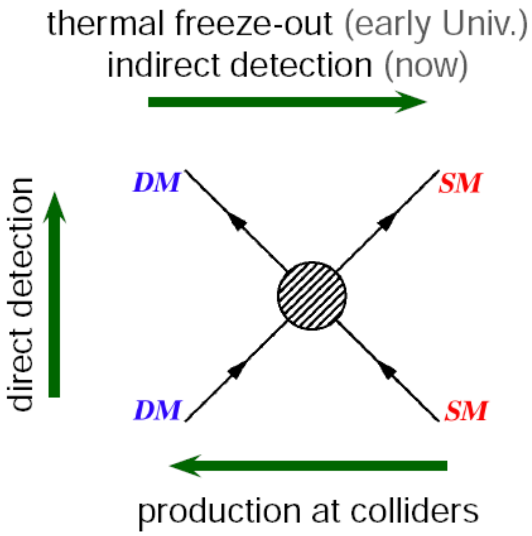

Figure 1.19: Collider, direct detection and indirect detection experiments probe different aspects of dark matter interactions with standard matter. Colliders are expected to measure dark matter mass as missing energy. Direct detection experiments measure the WIMP-nucleon scattering strength, while indirect searches look for the products of WIMP annihilation.

1.6 Signals Beyond the Simplest Supersymmetric Dark Matter

To successfully detect a signal from dark matter annihilation, the signal must be statistically significant above the astrophysical background. The annihilation signal contains a degeneracy: the rate of dark matter annihilation and its density both increase the detection rate of annihilation products. The assumptions made in this dissertation concerning dark matter density and some ways that this may be constrained in the future are discussed in Chapter 2.

Chapters 3 and 4 consider an augmentation to the mathematically well-motivated framework of supersymmetry, a leading candidate for describing particle physics beyond the Standard Model. Extending the Minimal Supersymmetric Model (MSSM) by adding the gauged U_{B-L} symmetry explains the presence of neutrino masses and mixings. These chapters explore the rammifications of the two new dark matter candidates in the model: the right-handed sneutrino and a new neutralino. Unlike other candidates, if the right-handed sneutrino acts as the lightest supersymmetric particle (LSP), it has zero spin and carries lepton number. Either of these candidates can experience Sommerfeld enhancement during annihilation and can correctly match the rate and kind of annihilation evidenced by PAMELA. In 2008, the PAMELA experiment observed a rise in the positron energy spectrum in the nearby region a few kiloparsecs in radius.

Chapter 5 demonstrates the feasibility of a discovery detection of right-handed sneutrino dark matter using IceCube/DeepCore. This work is extended more generally to any dark matter model in Chapter 6 in a discussion that moves beyond dark matter discovery to the challenge of distinguishing among dark matter annihilation signals that include a monochromatic neutrino signature. IceCube/DeepCore was completed in late 2011 and will place the leading constraints on the spin-dependent dark matter-nucleon scattering cross-section in the next year.

This dissertation explores a parameter region indicated by supersymmetric theory for which experiments are producing ever tighter and astrophysically relevant constraints. In the context of acknowledged uncertainties surrounding dark matter density and velocities that may be well constrained soon, we present a possible dark matter explanation for observed signals in the charged cosmic rays and seek to explore the limits of what dark matter properties may be observed through the neutrino annihilation signal.

Chapter 2

Gamma Ray Annihilation Signature

2.1 Fermi Gamma-ray Telescope

The Fermi satellite, launched in 2008, provides an unprecedented resolution in gamma rays and a factor of thirty improvement in sensitivity compared to its predecessor EGRET, which recorded the gamma ray sky up to 10 GeV. In contrast, the Fermi Large Area Telescope (LAT) is sensitive from a few tens of MeV to more than 300 GeV with a greater than 2 steradian field of view. A recent map of the gamma ray sky in this energy range is shown in Fig. 2.1.

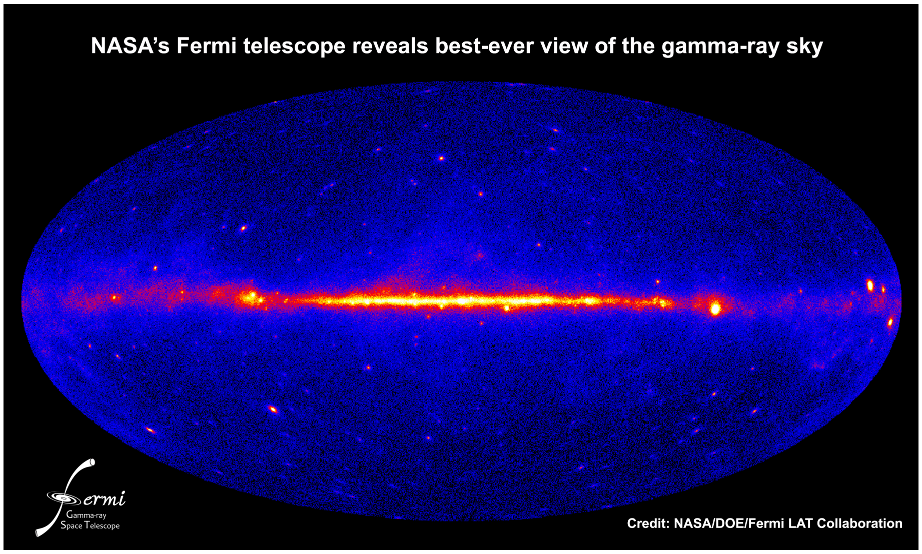

Figure 2.1: Fermi's view of the gamma ray sky.

Fermi delivers the unique capability of highly constraining dark matter (DM) annihilation to gamma rays. While dark matter cannot strongly couple to (emit) photons in order to produce observed rotation curves, the CMB or LSS, DM annihilation may still couple weakly to light and produce a detectable gamma ray phenomenology. In particular, annihilation can produce high energy charged cosmic rays. These charged particles will spontaneously emit photons via Bremsstrahlung radiation, and they will also interact with magnetic fields in the galaxy and produce gamma rays through synchrotron emission. As mentioned briefly in the introduction, DM may even annihilate to monoenergetic gamma rays directly via coupling to other particles. In this case the gamma rays would be the same energy as the DM mass and would provide a direct measurement of this mass and a possible confirmation of any missing energy from collider searches. While this coupling is expected to be suppressed by many orders of magnitude in a one-loop diagram (see Fig. 1.15), the unique monochromatic spike in the gamma ray spectrum would provide a smoking gun signature of DM models. The limits derived for DM annihilation to $\gamma\gamma$ from the current data are shown in Fig. 2.2. Note that similar limits are obtained by the Fermi collaboration for monocrhomatic annihilation to γZ via a similar loop.

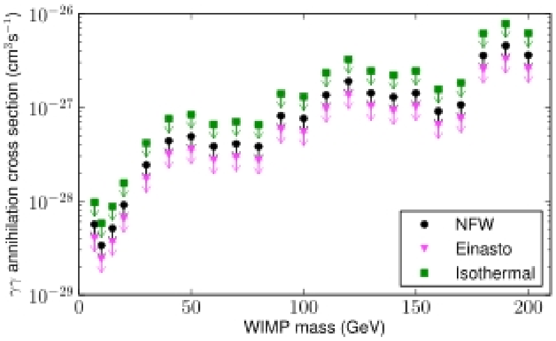

Figure 2.2: Upper limits on dark matter annihilation to $\gamma\gamma$ under the assumption of three dark matter profiles [30].

The total gamma ray integrated flux expected depends on astrophysical and quantum properties of the dark matter, including the annihilation rate, dark matter mass and density. Additionally, energy thresholds and cuts, angular cuts, detector energy and angular resolution and the astrophysical background all play a pivotal role in determining the sensitivity of an experiment to dark matter parameters. The total integrate flux can be schematically caluclated:

$$N_\gamma = \left(\int_{line of sight} \rho_{DM}^2 dl(\psi)\right)\left(\frac{\langle\sigma v\rangle}{m_{DM}^2}\right)$$

$$\times \left(\int_{E_{th}}^{m_{DM}} \left(\frac{dN_{\gamma}}{dE} A_{eff}(E) dE \right) \right) \frac{\Delta\Omega}{4\pi} \tau_{exp} \ . \tag{2.1}$$

This depends on the angular acceptance of the detector Ω and exposure time τ_{exp} but ignores concerns such as the energy reconstruction error. We address the impact of reconstruction error in the case of neutrino telescopes in Chapter 6.

Critically, limits on dark matter properties such as annihilation rate $\langle \sigma v \rangle$, in the case of traditional indirect detection experiments, and elastic scattering cross section, in the case of neutrino telescopes, are derived by analyzing the energy spectrum or integrated flux of annihilation products.

In general, Fermi can place constraints on the DM annihilation rate by observing gamma ray sources in various parts of the sky including the galactic center, dwarf spheroidals, extragalactic signals and the galactic halo diffuse flux, see Fig. 2.3.

Some of the tightest constraints come from a composite analysis of all dwarf galaxy subhalos and currently place a limit on DM annihilation to final states such as taus, Ws or bottom quarks just above the natural scale of annihilation expected for thermally produced weak scale particles [30], Fig 2.4. The dwarf spheroidal analysis benefits from the relatively low gamma ray background in these satellite subhalos of the Milky Way that have order-of-magnitude mass-to-luminosity ratios O(100 $M_{\odot}/L_{\odot}$).

Since annihilation is proportional to density squared as in equation 2.1, the galactic center is a natural place to search for a strong signature from dark matter. Analysis in the galactic center is complicated by the fact that there is some significant dispute about how cuspy the inner radial profile of the DM halo is. The Navarro Frenk and White profile is infinite at the center,

$$\rho(r) = \frac{\rho_0}{\frac{r}{R_s}\left(1 + \frac{r}{R_s}\right)^2} \ , \tag{2.2}$$

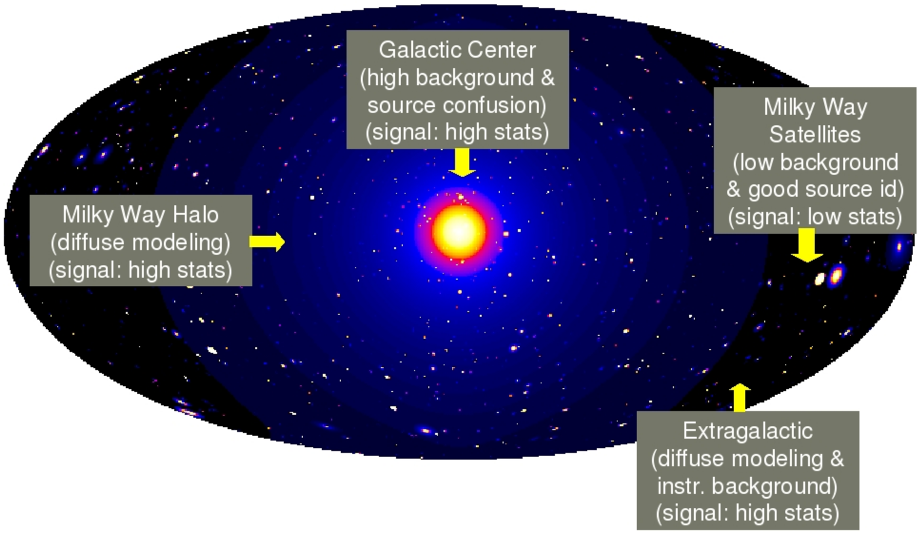

Figure 2.3: Searches for dark matter annihilation in the galactic center benefit from high dark matter density but suffer from background source confusion. Some of the tightest constraints on annihilation rate currently come from low background dwarf spheroidals (Milky Way satellites). Fermi has also placed limits on annihilation rates from the diffuse gamma rays and extragalactic sources such as galaxy clusters. Picture from Dr. Eduardo do Couto e Silva, Deputy Manager of Fermi's Large Area Telescope (LAT) Instrument Science Operations Center.

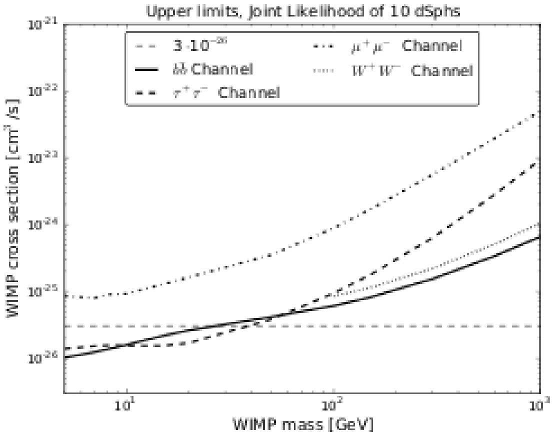

Figure 2.4: Dwarf spheroidal derived upper bounds on annihilation cross section based on annihilation final state [31].

where R_s and ρ_0 are parameters that can be fit to each halo. The Einasto profile fits DM N-body simulations well with a flat center instead

$$\rho(r) \propto \exp\left(-Ar^{\alpha}\right) , \tag{2.3}$$

where α determines the curvature of the profile. Not knowing this profile leads to order of magnitude uncertainties in calculating the flux from annihilating DM.

Additionally galactic center DM searches face the challenge of understanding all the other astrophysical sources of gamma rays near the center, including pion decays produced from charged cosmic ray collisions with gas and the inverse Compton scattering of electron charged cosmic rays off of photons from, e.g. the CMB. Additionally, the Milky Way's supermassive blackhole may contribute substantially to the gamma ray spectrum in the energy range of interest for WIMPs. This source confusion has made analysis of the galactic center difficult and has cast doubt on recent fits to the galactic center signal that claims a departure from the background that could be explained by $7-10$ GeV DM [36]. This problem with the galactic center illustrates precisely why a spectral monochromatic feature would be so fruitful: such a feature would be difficult to emulate astrophysically.

Fermi has observed a diffuse haze of gamma rays towards the Galactic center extending roughly fifty degrees [37]. This haze is consistent with a population of gamma rays upscattered from a population of hard electrons via inverse compton scattering. Recent analysis shows that the WMAP haze can be explained by the same population of electrons from the Fermi haze now producing synchrotron radiation in the microwave. While a standard spherical halo and isotropic cosmic ray diffusion cannot create these signals via annihilating dark matter, a prolate halo, anisotropic diffusion of electrons along magnetic field lines and an enhancement from a modification of the velocity dependence of the annihilation cross section together can match the signal [38]. The Fermi haze motivates a more careful look at assumptions surrounding the halo profile as well as the velocity dependence of the annihilation cross section.

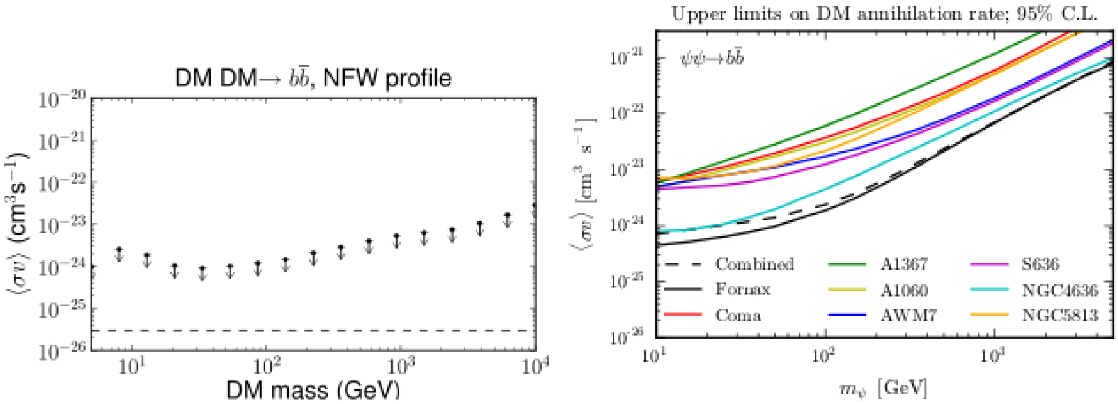

Figure 2.5: Left panel: From the diffuse gamma ray sky, upper limits on dark matter annihilation to $b\bar{b}$ under the assumption of an NFW dark matter halo profile. Other annihilation final states are shown in [30]. Right panel: upper limits on dark matter annihilation to $b\bar{b}$ for flux in a combined Galactic Cluster analysis [47].

The diffuse search limits are not as competetive as the dwarf spheroidal and monochromatic limits, Fig. 2.1. Similarly, the extra-Milky Way galactic cluster combined analysis, see Fig. 2.1, suffer a few orders of magnitude due to the extra modelling challenges associated with the intergalactic medium. However, all of these limits are infringing on the territory of cosmologically relevant annihilation rates, that is, the value expected if WIMPs annihilate today as they did during thermal production to create the relic density measured by the CMB, O(10^{-26}cm^3/s). Fermi thus stands to make significant contributions to the understanding of dark matter and may definitively eliminate critical regions of theoretically well-motivated paramater space.

2.2 Limitations on Fermi Bounds

However, the annihilation upper bounds from gamma ray observations depend on a number of degenerate factors all of which can increase or decrease the total count of gamma rays, including the dark matter final states, the uncertainty of both the density of the DM at the gamma ray source, the annihilation rate dependence on velocity as well as the velocity distribution and dispersion. A proper interpretation of the Fermi results will ultimately include these more subtle considerations. The limits published thus far make standard assumptions for some of the unknowns that when relaxed could significantly limit the cosmological implications of the Fermi results.

2.2.1 Velocity Dependence

The annihilation rate that we seek to constrain $\langle \sigma v \rangle$ is proportional to the velocity of the annihilating particles. The annihilation cross section itself may have some non-trivial velocity behavior. Additional lines of inquiry that are called for in light of the Fermi data investigate these two aspects of velocity dependence. The astrophysical question is: what is the DM velocity distribution? The particle physics inquiry, what is the velocity dependence of its annihilation cross section, may be answered by further astrophysical observations by Fermi.

On average, the Milky Way DM halo has a density of 0.4 GeV/cm^3, but this halo may have significant substructure. Any region in which the dark matter clumps more densely would produce an enhanced signature. For example, it has been postulated that in the formation of the baryonic galactic disk, infalling baryons could drag DM with them through gravitational interactions. This would form a disk of dark matter, the existence of which has been indicated in N-body simulations [39]. If a dark disk exists, then the lower velocity dispersion of this disk is lower than the spherical halo by a factor of six [40].

The DM annihilation cross section can depend on velocity in a number of ways. In the typical scenario, annihilation can be expanded in powers of the velocity squared:

$$\sigma = a + b\left(\frac{v}{c}\right)^2 + ... \tag{2.4}$$

With a concrete Lagrangian in mind, a quantum field theory calculation will reveal the values of the s-wave component a and the p-wave component b, etc. Virialized dark matter in the Milky Way will move at approximately one thousandth the speed of light. Theories with no s-wave component then experience p-wave suppression in their annihilation. Thus, sources of dark matter density with low velocity dispersion, as indicated in the disk would have lower signal for p-wave suppressed models, providing the possibility of differentiating these models from others using the Fermi telescope.

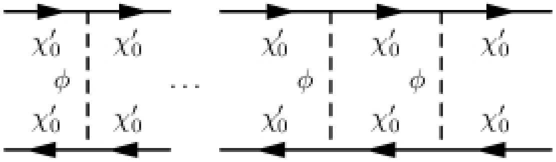

Figure 2.6: Example Sommerfeld enhancement diagram. The exchange of a light mediator can create an attractive force due to a Yukawa interaction between the DM and the light scalar.

However, it is also possible for models to experience an enhancement of s-wave annihilation for low velocities, where annihilation is inversely proportional to velocity. WIMPs may have a Yukawa interaction allowing the exchange of a light mediator. This exchange acts as an attractive force creating the Sommerfeld effect [41]. The Sommerfeld potential is exponential, since it must sum over not just one exchange of the mediator, but the sum of up to n such exchanges as in Fig. 2.6. The resulting form of the potential for the Yukawa term $\mathcal{L} \subset \lambda\phi\chi'\chi'$ is:

$$V(r) = \frac{-\lambda^2}{4\pi r^2} e^{-m_\phi r} \tag{2.5}$$

The wave function of the annihilation is a solution to the radial Schrodinger equation:

$$\frac{1}{m_{DM}}\psi''(r) - V(r)\psi(r) = -m_{DM}v^2\psi(r) \tag{2.6}$$

with the s-wave function $\Psi(r) \equiv \psi(r)/r$. The Sommerfeld enhancement has a finite range and saturates at a low velocity so that the enhancement $S \sim \alpha m_{\chi'}/m_\phi$. This happens when the de Broglie length of the particle exceeds the range of the interaction $(m_{DM}v)^{-1} > (m_\phi)^{-1}$.

It is important to realize that while Fermi is placing bounds on the value of annihilation that compare favorably to the annihilation rate at freeze out, DM with velocity dependent annihilation necessitates a lower prediction for the annihilation rate today. Fig. 2.7 shows that p-wave suppressed annihilation would be approximately six orders of magnitude less today than at freeze out, owing to the virialized, low velocity DM today. Meanwhile, s-wave annihilation with Sommerfeld enhancement could be as much as one to four orders of magnitude more than the annihilation at freeze out. Chapters 3 and 4 address the impact of Sommerfeld enhancement in $U(1)_{B-L}$ extension to the MSSM. Thus, Fermi's bounds are already limiting s-wave Sommerfeld enhanced models but are not as consequential for p-wave models.

There are further measurable consequences to the velocity dependence of DM annihilation. If the Sommerfeld enhancement to dark matter interactions is strong enough, then the dark matter velocity dispersion will become isotropic, creating a spherical DM halo. Thus, measurements of the ellipticity of the DM halo can provide constraints on the mass of any mediating particle that creates the Sommerfeld enhancement [43]. In a similar manner, the DM disc may constrain the mediator mass and coupling. The contributions to DM signals from the disk can be more significant in Sommerfeld models than for WIMPs without such low-velocity enhancements.

Besides the DM disk, the velocity dependence of models may be extracted by

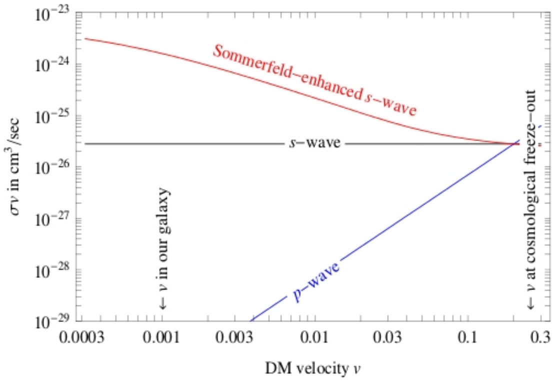

Figure 2.7: P-wave suppressed annihilation rates suffer as dark matter virializes in the halo at lower velocities; Sommerfeld enhanced DM annihilation benefits from an attractive force felt at low velocities [42].

looking at a variety of DM structures. For example, it has already been shown that p-wave suppressed models are one order of magnitude different in their angular power spectrum in the extragalactic signal [44]. However, in the halo it may be possible to distinguish between large subhalos who support higher DM velocities and would have an enhanced Sommerfeld effect and smaller subhalos for which high velocity DM would escape. This angular scale may be distinguished in our DM halo.

Additionally, the tidal streams visible in M31 in the gamma ray signal may be sufficient to define the expected velocity dependence of the cross-section for Fermi. In Sommerfeld scenarios, streams in the outer regions of the halo may significantly contribute to the gamma ray signal [44]. Fermi might be able to statistically resolve the relative strength of contributions to the velocity dependent cross-section.

2.2.2 Constraints on Substructure

Looking at DM substructures, such as dwarf spheroidals in the Milky Way halo may produce a visible gamma ray signal with relatively low astrophysical background. Aquarius and Via Lactea II, state-of-the-art N-body simulations, predict too many dwarf galaxies in DM halos. The difference in predicted and observed substructure may possibly be explained by collisional damping. DM particles can scatter elastically with other particles even after freeze-out. DM would remain in chemical equilibrium until kinetic decoupling, after which DM is effectively collisionless [45]. Thus, density fluctuations on scales less than the free-streaming scale are severely suppressed. Damping erases substructure on some scale, dependent on DM mass and couplings. Thus, the elastic scattering of the DM is indicative of the scale of substructure and vice versa.

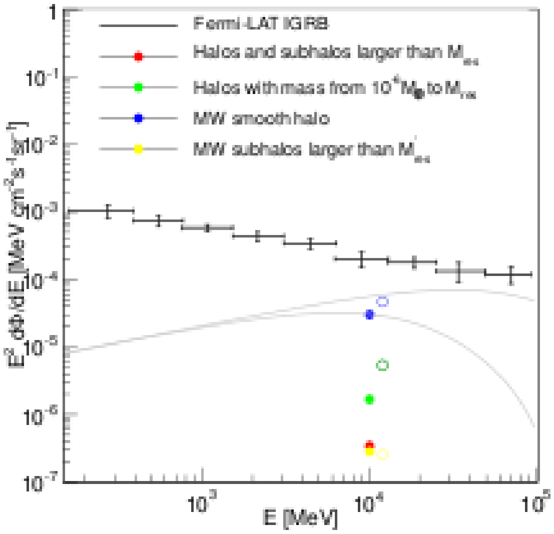

Figure 2.8: Energy spectrum flux of diffuse gamma rays from Fermi LAT appears in black. The blue filled circle is the flux from DM annihilation for a smooth DM halo. The yellow dot represents the flux from all the subhalos in the Aquarius simulation (above the lowest resolved mass of the simulation, M_{res}). A significant portion of the expected flux is extrapolated from masses below the resolution limit, green dot. The grey line indicates flux from annihilation to bottom quarks, normalized to a smooth halo [46].

Work that has been done to predict the gamma ray signal from substructure has had to extrapolate the halo mass function below the resolution of the simulations, from ten million solar masses down to the DM particle damping scale [46]. There can be significant contributions from substrucutre to the flux, depending on the accuracy of such extrapolations, see Fig. 2.8. The current uncertainty in substructure suggests that boosts to the gamma ray signal may be of order two toward the galactic center and between tens to hundreds in the halo and in extragalactic signals. Furthermore, it is theorized that dynamical friction and tidal stripping leads to the depletion of some substructure near the center of clusters. This results in a boosted signal in the more dense outskirts of the main halo compared to the stripped center. Boosts between ten and a thousand are possible in galaxy clusters [47].

Usually, a low-mass cutoff of halo structure of 10^{-6} solar masses is used to calculate these boosts, but this presumes a kinetic decoupling temperature about 100 MeV, which is appropriate for a standard WIMP. However, some Fermi bounds calculate an upper limit on annihilation channels without considering substructure or other possible boosts [30, 48]. DM carrying lepton number, like the sneutrino DM considered in Chapters 3, 4 and 5, may have significantly constrained annihilation rates in the unsuppressed monochromatic neutrino channel. A scan of the MSSM parameter space 1) considering the full range of structure cutoff scales that help determine substructure scale and 2) incorporating the uncertainty in substructure when translating the Fermi detection to an annihilation rate is called for but beyond the scope of this work.

Direct detection experiments DAMA and COGENT provide some evidence for the existence of a few GeV DM. For light DM masses, the substructure scale would cutoff below between 10^7 and 10^4 solar masses [49]. In the absence of substructure, mediators less than 200 MeV are forbidden. However, light DM experiencing Somerfeld enhancement may avoid constraints arising from the substructure free streaming cutoff since recent evidence has shown that mediators less than 200 MeV can avoid such constraints [50]. The long term sensitivity of the Fermi satellite to faint subhalos may further constrain mediator properties.

As a final word, throughout this work we assume the thermal production of

DM, that is, DM maintains thermal and chemical equilibrium with its surroundings, following the Maxwell-Boltzmann equation and freezing-out at a relic density determined by its mass, couplings and annihilation rate. However, non-thermal models can produce DM with the correct Ω_{CDM} as measured by WMAP-7 but without the consequently tight constraints on the annihilation cross section. Non-thermal DM sacrifices the WIMP miracle, but is known to exhibit a severely suppressed power spectrum compared to thermal DM models [51]. Non-thermal production with light mediators may change the bounds on DM annihilation rate and substructure scale. Scalars in early times [52] in the universe may produce extremely dense substructures that could dominate the indirect detection signal.

2.2.3 Annihilation Final States

All of the limits that Fermi derives are for individual dark matter annihilation states. Each charged state of annihilation has a different characteristic production of gamma rays, from the very hard bottom quark spectrum to the softer muon spectrum. For gamma rays the hardest (most energetic) spectra are for the heavier particles, whose radiation will be proportional to the final state energy and in turn the dark matter mass. This stands in contrast to the relative hardness of neutrino spectra viewed by IceCube, where primary neutrino final states are more energetic than annihilation to W bosons. Thus, depending on the assumption of final state, more stringent bounds can be placed on the annihilation rate, or in other words, there is a degeneracy between the final state and annihilation rate.

By assuming muon or tau final states in Chapters 3 and 4, we are better able to fit the charged cosmic ray observations from PAMELA and ATIC. In Chapter 5, we evaluate the monochromatic neutrino annihilation as a tool to identify sneutrino dark matter. While annihilation to Ws or neutrinos alone could produce the same total signal count, strategic energy and angle cuts can highlight the distinctive monochromatic neutrino signal. This energy and angular spectral analysis comes to the forefront again in Chapter 6 where we discover that final state discrimination between branching fractions to W bosons or τs in the presence of monochromatic neutrinos is possible.

This case study investigation of the limits of the Fermi bounds provides an indication of the types of assumptions that feed into calculating bounds on dark matter properties. For the rest of this work, we assume a NFW halo profile and investigate the properties of various dark matter annihilation final states.

Chapter 3

A Supersymmetric $B - L$ Dark Matter Model and the Observed Anomalies in the Cosmic Rays

Major Results

PAMELA data indicate an increase in the positron fraction compared to the expected astrophysical background but indicate no such increase for the anti-proton spectrum. This chapter, co-authored with Drs. Rouzbeh Allahverdi, Bhaskar Dutta and Yudi Santoso, first appeared in Physical Review D [1] and considers whether a $U(1)_{B-L}$ model extension to the MSSM could provide annihilating dark matter that matches the signal. Such a model has been proposed historically because of its ability to explain the light left-handed neutrino masses through a see-saw mechanism.

The gauged $U(1)_{B-L}$ extension results in both right-handed neutrinos and their right-handed supersymmetric partners in order to avoid creating any anomalies in the field theory. Furthermore, the $U(1)$ symmetry is mediated by a new Z' boson in analogy with the Standard Model hypercharge $U(1)$. However, the Z' candidate cannot be massless but must acquire a mass through symmetry breaking. The Standard Model Higgs cannot give the Z' mass, since it is not charged under $B-L$ and therefore cannot break the symmetry. Thus we introduce a Higgs with $B-L$ charge. The $\widetilde{Z}'$ and Higgsino-prime mix to create a χ' that can act as the Lightest Supersymmetric Particle.

This paper shows that such a χ' LSP will annihilate leptophilically, thanks to the $B-L$ charges, and may experience a Sommerfeld enhancement to its s-wave annihilation. These features of the model make it capable of explaining the PAMELA data. In fact, correct relic densities and matches to PAMELA and ATIC data are possible for DM annihilation to μs and τs with a mass of 1.5 TeV and an enhancement of 10^3.

Published Abstract

We propose a simple model of supersymmetric dark matter that can explain recent results from PAMELA and ATIC experiments. It is based on a $U(1)_{B-L}$ extension of the minimal supersymmetric standard model. The dark matter particle is a linear combination of the $U(1)_{B-L}$ gaugino and Higgsino partners of Higgs fields that break the $B-L$ around one TeV. The dominant mode of dark matter annihilation is to the lightest of the new Higgs fields, which has a mass in the GeV range, and its subsequent decay mainly produces taus or muons by the virtue of $B-L$ charges. This light Higgs also results in Sommerfeld enhancement of the dark matter annihilation cross section, which can be $\gtrsim 10^3$. For a dark matter mass in the $1-2$ TeV range, the model provides a good fit to the PAMELA data and a reasonable fit to the ATIC data. We also briefly discuss the prospects of this model for direct detection experiments and the LHC.

Published Paper

One of the major problems at the interface of particle physics and cosmology is dark matter and its identity. There are various lines of evidence supporting the existence of dark matter in the universe, and it is well established that particle physics can explain dark matter in the form of weakly interacting massive particles [19]. The standard scenario is thermal dark matter in which the dark matter relic abundance, as precisely measured by cosmic microwave background (CMB) experiments [53], is determined from the freeze out of the dark matter annihilation in the early universe. Supersymmetry is a front runner candidate for physics beyond the standard model (SM). It addresses the hierarchy problem of the SM and has a natural dark matter candidate in the form of the lightest supersymmetric particle (LSP). It has been known that in supersymmetric models, a neutralino LSP can have the thermal relic abundance required for dark matter [54].

There are major experimental efforts for direct and indirect detection of dark matter particle beside the gravitational effect that it has on the universe. Indirect detection investigates final states (photons, anti-particles, neutrinos) from the annihilation of dark matter through astrophysical observations, while the direct detection probes the scattering of the dark matter particle off nuclei in the dark matter detectors. The PAMELA satellite is an indirect experiment that has recently published results on cosmic ray flux measurements. The data show an excess of positrons at energies above 10 GeV [32], while no excess of anti-proton flux is observed [33]. The publication shows results up to 100 GeV and the experiment is expected to get data up to ~ 270 GeV. There is also new data from the ATIC (a balloon experiment) where one observes excess in $e^+ + e^-$ spectrum with a peak around 600 GeV [55]. The backgrounds are nominal for both of these effects. Another balloon experiment, the PPB-BETS [56], also reports excess in the $e^+ + e^-$ energy spectrum between 500-800 GeV. However, the excess is based on a few data-points that are not quite consistent with ATIC data. While there could be astrophysical explanations for these anomalies [57], it is natural to ask whether they can be attributed to the effect of dark matter annihilation in the halo.

Model-independent analysis shows that the annihilation cross section required to explain the positron excess exceeds the canonical value required by relic density $\sim 3 \times 10^{-26}$ cm^3/s by at least an order of magnitude [58]. In the usual minimal Supergravity (mSUGRA) model, the situation is further complicated since dark matter annihilation to fermions in that model is P-wave suppressed, implying a much smaller annihilation cross section today as compared to that at the freeze out time. Even in the best case scenarios an astrophysical boost factor of $10^3 - 10^4$ is then needed to explain the positron excess [59], which might be difficult to obtain based on the recent analysis on substructures(see e.g. [60]). Moreover, in order to explain both the positron and anti-proton data, dark matter annihilation must dominantly produce leptons as direct products [42, 61]. There have been proposals [42, 62] (also see [63, 64]) for new dark matter models in which the dark matter candidate belongs to a hidden sector. Acceptable thermal relic density is obtained via new gauge interactions, dark matter annihilation today is enhanced via Sommerfeld effect [41] due to existence of light bosons, and the annihilation mainly produces lepton final states. This set up can explain PAMELA data for dark matter mass of a few hundred GeV without needing a large boost factor, and ATIC data for larger masses [65].

In this paper we provide a concrete model to explain the recently measured anomalies in the cosmic ray. Our model is a simple extension of the minimal supersymmetric standard model (MSSM) that includes a gauged $U(1)_{B-L}$ [66]. The $B-L$ extension is very well motivated since it automatically implies the existence of three right-handed (RH) neutrinos through which one can explain the neutrino masses and mixings. It has also been shown that this model can explain inflation [67, 68]. The model contains a new gauge boson Z', two new Higgs fields H'_1 and H'_2, and their supersymmetric partners.

The $B-L$ charge assignments are shown in Table 1. The superpotential is

$$W = W_{\rm MSSM} + W_N + \mu' H'_1 H'_2 \tag{3.1}$$

where W_N is the superpotential containing RH neutrinos, and μ' is the new Higgs mixing parameter. The new Higgs fields do not have renormalizable coupling to lepton and quark fermions as a result of their $B-L$ charges. The $U(1)_{B-L}$ symmetry is broken by the VEV of the new Higgs bosons, $v'_1 \equiv \langle H'_1 \rangle$ and $v'_2 \equiv \langle H'_2 \rangle$. This gives a mass $m_{Z'}$ to Z', where $m^2_{Z'} = (27/4) g^2_{B-L} (v'^2_1 + v'^2_2)$, with g_{B-L} being the $B-L$ gauge coupling. We have three physical Higgs states, the lightest of which ϕ has a mass m_ϕ which is related to $m_{Z'}$ through $m^2_\phi < m^2_{Z'} \cos^2 2\beta'$, where $\tan\beta' \equiv v'_2/v'_1$.

Fields	Q	Q^c	L	L^c	N	N^c	H'_1	H'_2
Q_{B-L}	1/6	-1/6	-1/2	1/2	-1/2	1/2	3/2	-3/2

Table 3.1: The $B-L$ charges of the fields. Here Q, L and N represent quarks, leptons, and RH neutrinos respectively; while H'_1 and H'_2 are the two new Higgs fields. The MSSM Higgs fields have zero $B-L$ charges and are not shown in the table.

For $\tan\beta' \approx 1$ we have $m_\phi \ll m_{Z'}$. The other two Higgs states, Φ and $\mathcal{A}$, are heavy and have masses comparable to $m_{Z'}$. Note that unlike the MSSM case, radiative corrections to the Higgs quartic coupling do not lift m_ϕ because H'_1 and H'_2 are not coupled to fermions. Note that although the particle content in our model is similar to the one in [69], our set up is different. Assuming that supersymmetric particles in the MSSM sector are heavier than those in the $U(1)_{B-L}$ sector, the dark matter in this model arises from the new sector. The dark matter particle, denoted by χ_1^0, is the lightest of the three new neutralinos χ_i^0 (not to be confused with the MSSM neutralinos which we do not discuss in this paper). It is a linear combination of the $U(1)_{B-L}$ gaugino $\widetilde{Z}'$ and the two Higgsinos $\widetilde{H}'_1$, $\widetilde{H}'_2$. The dark matter thermal relic abundance is dictated by the annihilation of the lightest neutralino χ_1^0 into a pair of ϕ via s-channel exchange of ϕ and Φ, and t-channel exchange of χ_i^0. (There is also subdominant annihilation processes to $f\bar{f}$ via s-channel Z' exchange, and t-channel sfermion exchange.) The annihilation to $\phi\phi$ is not P-wave suppressed since the final state particles are bosons. Hence the (perturbative) annihilation cross-section does not change between the time of freeze-out and the present time.

The ϕ subsequently decays into fermion-antifermion pairs via a one-loop diagram containing two Z' bosons. The decay rate is given by:

$$\Gamma(\phi \to f\bar{f}) = \frac{C_f}{2^6\pi^5}\frac{g_{B-L}^6 Q_f^4 Q_\phi^2 m_\phi^5 m_f^2}{m_{Z'}^6}\left(\frac{1}{2} - \frac{2m_f^2}{m_\phi^2}\right), \tag{3.2}$$

where Q_ϕ and Q_f are the $B-L$ charges of ϕ and the final state fermion respectively,

m_f is the fermion mass, and C_f denotes color factor. (The Higgs can also decay into four fermion final states via two virtual Z', but this decay mode is suppressed by two orders of magnitude compared to the two fermion final states.) Decays to neutrinos are much suppressed because of the negligible neutrino masses. Since $B-L$ charge of leptons is three times larger than that of quarks, the leptonic branching ratio is about 27 times larger than that for quarks of comparable mass. We note that m_ϕ can be controlled by the VEVs of the new Higgs fields and for comparable VEVs, i.e. for $\tan\beta' \approx 1$, it can be very small without any tuning on the soft masses in the Higgs sector. We can choose this mass to be between $O(1)$ GeV and 10 GeV. For $2m_\tau < m_\phi < 2m_b$ the dominant decay mode is to $\tau^-\tau^+$ final state. If m_ϕ is slightly less than $2m_\tau$, ϕ can decay either to $c\bar{c}$ or $\mu^-\mu^+$ with comparable branching ratios. It is possible to reduce the ϕ mass further to be below $2m_c$, and make $\mu^-\mu^+$ final state the dominant decay mode.

The annihilation cross section at the present time has Sommerfeld enhancement as a result of the attractive force between dark matter particles due to the light Higgs boson exchange. The Higgs coupling to dark matter, $h\phi\bar{\chi}^0_1\chi^0_1$, leads to an attractive potential $V(r) = -\alpha(e^{-m_\phi r}/r)$ in the non-relativistic limit, where $\alpha \equiv h^2/\pi$. Note that α is larger than the usual definition of fine structure constant because of the Majorana nature of χ^0_1. Since the neutralinos are traveling with non-relativistic speed $v \sim 10^{-3}c$ today, the Sommerfeld effect is much more important now than at the time of freeze out. The Sommerfeld enhancement in our model can be $\gtrsim 10^3$. We can therefore explain the PAMELA data without requiring any boost factor.

To show that our model can explain the PAMELA data, we pick random parameters and generate point models. We then calculate the relic density and the Sommerfeld enhancement factor for each of these models. We use reasonable values for the parameters, i.e. $\tan\beta' \approx 1$, $m_{Z'} > 1.5$ TeV, $\mu' = 0.5-1.5$ TeV, soft masses for the Higgs fields $m_{H'_{1,2}} = 200-600$ GeV, and soft gaugino mass $M_{\tilde{Z}'} = 200-600$ GeV.

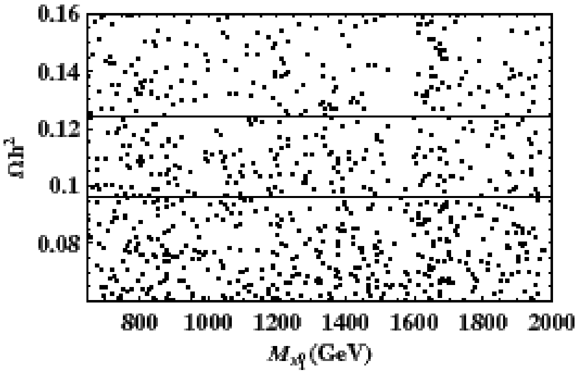

Figure 3.1: We show the relic density and the neutralino mass for model points generated by varying the parameters mentioned in the text.

We use $g_{B-L} \sim 0.45$, which is in concordance with unification of the gauge couplings (we need to use a normalization factor $\sqrt{3/2}$ for unification). The Z' mass used in the calculation obeys the LEP and the Tevatron bounds [70, 71] for our charge assignments.

In Figure 3.1, we show the relic density and the dark matter mass for different points. The horizontal band shows the acceptable range for relic density according to the latest CMB data [53]. In Figure 3.2 we show the possible enhancement that can be obtained for these points in term of $\epsilon_\phi \equiv m_\phi/\alpha M_{\chi_1^0}$. Note that for points that satisfy the relic density constraint thereare many that have enhancement factor $\geq 10^3$, corresponding to $\epsilon_\phi = 0.153$ to 0.157, within the whole range of $M_{\chi_1^0}$ shown in Figure 3.1. In addition, we note that the lifetime of ϕ for these points is found to be $\tau_\phi \sim 10^{-4} - 10^{-3}$ seconds from Eq. (2). This is short enough to escape the tightest bounds from big bang nucleosynthesis (BBN) [72].

We select models that satisfy the dark matter relic density. We then use `DarkSUSY -5.0.2` [73] to calculate the positron flux from dark matter annihilation. Note that each pair annihilation in our model produces 2 ϕ's that yield four fermions upon their decay. For this reason, we generally need a heavier neutralino compared to

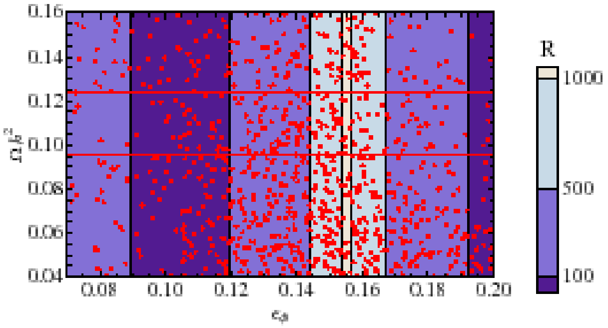

Figure 3.2: We show relic density as a function of ϵ_ϕ. We show different ranges for the Sommerfeld enhancement factor R by shades.

models in which the pair annihilation directly produces two fermions. We normalize the positron fraction by a factor $k_b = 1.11$ [74]. There are theoretical uncertainties in the positron cosmic ray flux calculation due to the assumptions about the dark matter halo profile and the cosmic ray propagation model. Here we assume a NFW profile [75] and MED parameters for the propagation as defined in [76].

In Figure 3.3, we show our fit to the PAMELA data for $M_{\chi_1^0} = 1, 1.5$ and 2 TeV, for $\tau^-\tau^+$ final state case. We see that the fit is very good for a neutralino mass around 1.5 TeV. We have chosen a point where the enhancement factor is 10^3. In general, for larger enhancement factors we can fit the data with a larger neutralino mass. For an enhancement factor of 10^4, we can obtain a good fit for a dark matter mass around 5 TeV. On the other hand, smaller masses require a smaller enhancement factor. However, for this tau case the fit with a smaller mass is not good because the spectrum is too soft. The antiproton data is still satisfied with this large enhancement factor since the leptonic branching ratio is much larger (~ 27) compared to the quark branching ratios.

In Figure 3.4 we show the plot with $\mu^-\mu^+$ final states. In order for the Higgs to mainly decay to muons, we need to make m_ϕ smaller than twice the charm mass. However, the lifetime of the Higgs becomes larger than a second in this case, which

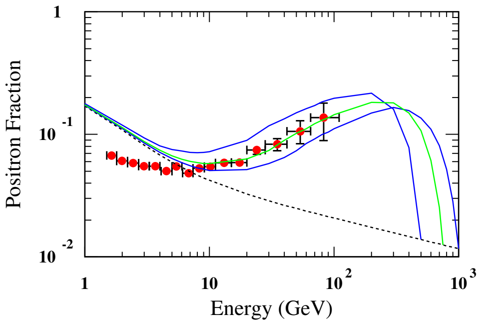

Figure 3.3: We show a fit to the PAMELA data when the ϕ decays mostly to taus for neutralino masses to be 1, 1.5, and 2 TeV (from top to bottom), with enhancement factor 10^3.

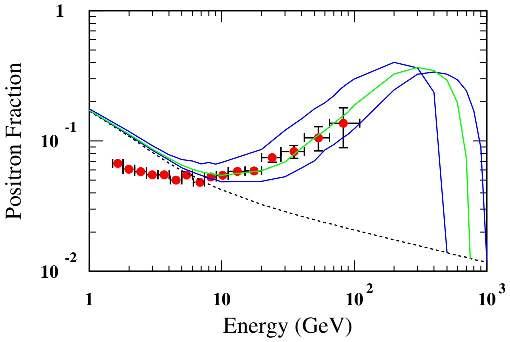

Figure 3.4: Same as Fig. 3.3 but for the case of final state muons.

will be problematic for BBN [72]. The Higgs lifetime can be reduced if we increase the $B-L$ charges by a factor of two. On the other hand, the positron spectrum in the muon case is harder than that in the tau case, and we can also fit the PAMELA data with a 500 GeV neutralino mass, and an enhancement factor of around 100.

In Figure 3.5 we show the fit to the ATIC data by using muon and tau final states. We normalize the background to fit with the data at smaller energies. We again use enhancement factor of 10^3. We see that the muon final states give a better fit than the tau final states. However, we can see that the simultaneous fit to both ATIC and PAMELA is not satisfactory. In particular, it is more difficult to fit the ATIC data with our model. If we use a large enhancement factor, the spectrum at smaller energies will also be lifted up. From the ATIC data plot [55], there seems

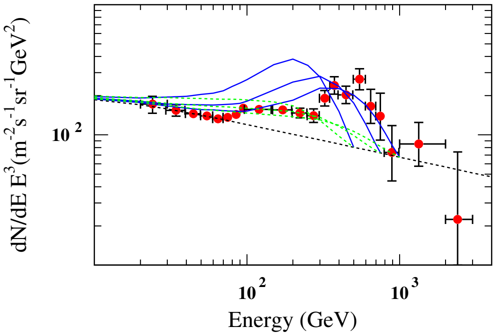

Figure 3.5: We show a fit to the ATIC data when ϕ decays to muons mostly (solid line) and taus mostly(dashed line) for the lightest neutralino masses to be 1, 1.5 and 2 TeV

to be some missing signals at some energies which results in the jagged curve. This can also indicate more than one source for the excess. In any case, we need to wait for verification from future experiments. It is interesting to point out that there is a proposal for an upgraded version of ATIC, called ECAL [77], which should have much improved background rejection power and higher resolution. We will be able identify the model parameter space by combining results from all these experiments.

We would also like to comment on other phenomenological aspects of the model. The leading order interaction of dark matter particle χ_1^0 with quarks is via squark exchange in the t-channel. The new Higgs fields couple to the quarks at one-loop level, and hence interactions via Higgs exchange are suppressed (even after Sommerfled enhancement is taken into account). As a result, the cross section for spin-independent interactions is also very small, well below 10^{-10} pb, and hence beyond the reach of direct detection experiments. We note that since left and right quarks have the same $B-L$ charge, and χ_1^0 is a Majorana particle, there will be strictly no spin-dependent interactions between dark matter and ordinary matter in this model. The model however has a great potential to be observed with the Fermi Satellite experiment. The Sommerfeld enhancement would still be responsible for giving rise to a higher rate of photons in the cosmic gamma ray background.

At the LHC, the Z' can be produced. However, the new light Higgs ϕ will decay outside of the detector, hence will be missed, because of its long life time ($\sim 10^{-4}$ sec). Thus we have another source of missing energy signal in this model. We also note that there are 7 neutralinos in this model, compared to four in the MSSM, while the number of charginos is still two. Therefore, using the end point analysis [78], one can find many neutral states.

Acknowledgement- The authors would like to thank S. Bornhauser, M. Cvetic, P. Gondolo, R. Mahapatra, D. Toback, L. Wang and J.P. Wefel for useful discussions and communications. The work of BD is supported in part by DOE grant DE-FG02-95ER40917.

Chapter 4

Sneutrino Dark Matter and the Observed Anomalies in Cosmic Rays

Major Results

This chapter, representing work with co-authors Drs. Rouzbeh Allahverdi, Bhaskar Dutta and Yudi Santoso, was originally published in Physics Letters B [2] and explores further the $U(1)_{B-L}$ model extension to the MSSM first presented in Chapter 3. The gauged $U(1)_{B-L}$ extension has a second viable LSP candidate, the right-handed sneutrino. The $\widetilde{N}$ also can experience Sommerfeld enhancement to its leptophilic s-wave annihilation which occurs thanks to its scalar nature. Correct relic densities and Sommerfeld enhancements create a positron spectrum that also reproduces the PAMELA results for annihiation to τs or μs for a DM mass of 1.5 TeV and an enhancement of 10^3. This particular configuration is of interest since the inflaton may take the form of one of the flat directions in the theory. Thus, this model extension has the attractive property of containing a DM and inflaton candidate at the same time as it provides a potential explanation for the light left-handed neutrino masses.

Abstract

We revisit sneutrino dark matter in light of the recent results from the PAMELA and ATIC experiments. In the $U(1)_{B-L}$ extension of the minimal supersymmetric standard model the right-handed sneutrino is a natural candidate for thermal dark matter. Sneutrino annihilation at the present time can be considerably enhanced due to the exchange of the lightest field in the Higgs sector that breaks $U(1)_{B-L}$. The annihilation mainly produces taus (or muons) by the virtue of $B-L$ charges. A sneutrino mass in the $1-2$ TeV range provides a good fit to the PAMELA data and a reasonable fit to the ATIC data. Within this mass range the sneutrino-nucleon elastic scattering cross section is $10^{-11}-10^{-9}$ pb, which might be probed by upcoming and future direct detection experiments. In addition, if (at least) one of the neutrinos

is dominantly a Dirac fermion, the sneutrino can provide a unified picture of dark matter and inflation.

4.1 Introduction

Even though the existence of dark matter has been supported by various lines of evidence, the identity of dark matter itself is not yet known. One proposed solution for this dark matter problem comes from particle physics beyond the standard model in the form of weakly interacting massive particles (WIMPs) [79]. In particular, for weak scale masses and interactions, thermal freeze out of WIMP annihilation in the early universe can result in an acceptable relic abundance for dark matter, as precisely measured by cosmic microwave background (CMB) experiments [53]. Supersymmetry, as one candidate for physics beyond the standard model, has a natural dark matter candidate in the lightest supersymmetric particle (LSP). It is known that in supersymmetric models a neutralino LSP is a suitable candidate for dark matter [54].

There are currently major experimental efforts for both direct and indirect detection of the dark matter particle. Direct detection probes the scattering of the dark matter particle off nuclei in underground dark matter detectors, while indirect detection investigates astrophysical effects of dark matter annihilation in the galaxy, including signatures in the cosmic rays. PAMELA is a satellite-borne experiment that measures cosmic ray fluxes. The recently published results show an excess of positron flux at energies above 10 GeV [32], while no excess of anti-proton flux is observed [33]. The publication shows results up to ~ 100 GeV and the experiment is expected to get data up to ~ 190 GeV for anti-protons and ~ 270 GeV for positrons. Another cosmic ray experiment called ATIC (a balloon experiment) has also recently published data where one observes an excess in the $e^+ + e^-$ spectrum with a peak around 600 GeV [55]. There is a third experiment, the PPB-BETS [56] (also a balloon experiment), which reports an excess in the $e^+ + e^-$ energy spectrum between 500 and 800 GeV. However, the excess is based on a few data-points that are not quite consistent with the ATIC data. While there could be astrophysical explanations for these anomalies (e.g. from nearby pulsars [57, 80]), it is reasonable to ask whether they can be attributed to the effect of dark matter annihilation in the galaxy.

Model-independent analysis shows that the annihilation cross section required to explain the positron excess exceeds the canonical value required by relic density, i.e. $\sim 3 \times 10^{-26}$ cm^3/s, by at least an order of magnitude [58]. In the usual neutralino dark matter scenario in the minimal Supergravity (mSUGRA) model, the situation is further complicated because the dark matter annihilation (to fermions) in that model is P-wave suppressed, implying a much smaller annihilation cross section today as compared to that at the freeze out time. An astrophysical boost factor of $10^3 - 10^4$ is then needed to explain the observed positron excess [59]. However, this might be difficult to obtain based on recent analyses of halo substructures (see e.g. [60]). Moreover, in order to explain both the positron and anti-proton data, dark matter annihilation must be dominated by leptonic final state modes [42, 61]. (There could also be some effects from anisotropic propagation on the positron and anti-proton fluxes that still need to be investigated [81].) There have been proposals [42, 62] (also see [63]) for new dark matter models in which the dark matter candidate belongs to a hidden sector, and an acceptable thermal relic density is obtained via new gauge interactions. The key ideas of these models are that the dark matter annihilation today is enhanced by a Sommerfeld effect [41] due to the existence of light bosons and that annihilation mainly produces lepton final states via symmetry of the hidden sector. This arrangement explains PAMELA data for a dark matter mass of a few hundred GeV, without needing a large astrophysical boost factor, and ATIC data for larger values of dark matter mass [65]. Another type of explanation that has been proposed for the data is decaying dark matter with a tuned lifetime [64].

We recently proposed an explicit model that can explain the measured anomalies in the cosmic rays [1]. It is based on a simple extension of the minimal supersymmetric standard model (MSSM) that includes a gauged $U(1)_{B-L}$ and where the dark matter is the lightest neutralino in the new sector. Even though this model has a large dark matter annihilation cross section today due to Sommerfeld enhancement, the cross section for scattering of dark matter off quarks is too low to be accessible to direct detection experiments. In fact, this is a generic situation for hidden sector dark matter models that can explain PAMELA data along the line discussed above.

In this paper we again consider a $B - L$ extension of the MSSM, but with the right-handed (RH) sneutrino as the dark matter. As we will argue, this is a minimal model of thermal dark matter that can explain the observed anomalies in the cosmic rays and can also be probed by direct detection experiments. The main channel of sneutrino annihilation is to light Higgs fields, which carry a non-zero $B-L$ quantum number. These Higgs particles in turn decay dominantly to leptons by virtue of the $B - L$ charges for fermions. The same Higgs field also results in a large Sommerfeld enhancement factor for the annihilation cross section. For a sneutrino mass of 1-2 TeV, this model can explain PAMELA and ATIC data. In addition, due to the scalar nature of dark matter, the sneutrino-proton elastic scattering cross section is in the $10^{-11} - 10^{-9}$ pb range, which is an interesting range from a direct detection perspective. Moreover, the sneutrino can be part of the field that drives primordial inflation, thus explaining the small temperature anisotropy in the cosmic microwave background (CMB) via tiny neutrino masses [67, 68]. We will also discuss various possibilities for radiative breaking of the $B - L$ symmetry and some related issues.

4.2 The model

The $B-L$ extension of the MSSM [66] is well motivated since it automatically implies the existence of three RH neutrinos through which one can explain the neutrino masses and mixings. The minimal model contains a new gauge boson Z', two new Higgs fields H_1' and H_2', the RH neutrinos N, and their supersymmetric partners. The superpotential is (the boldface characters denote superfields)

$$W = W_{\text{MSSM}} + W_{B-L} + y_D \mathbf{N}^c \mathbf{H_u} \mathbf{L}\,, \tag{4.1}$$

where $\mathbf{H_u}$ and $\mathbf{L}$ are the superfields containing the Higgs field that gives mass to up-type quarks and the left-handed (LH) leptons respectively. For simplicity, we have omitted the family indices. The W_{B-L} term contains $\mathbf{H_1'}$, $\mathbf{H_2'}$ and $\mathbf{N}^c$. Its detailed form depends on the charge assignments of the new Higgs fields (explicit examples will be presented later). The last term on the RH side of Eq. (4.1) is the neutrino Yukawa coupling term.

The scalar potential consists of F-terms from the superpotential, and D-terms from the gauge symmetries. The D-term contribution from $U(1)_{B-L}$ is given by

$$V_D \supset \frac{1}{2} D_{B-L}^2, \tag{4.2}$$

where

$$D_{B-L} = \frac{1}{2} g_{B-L} \left[Q_1 (|H_1'|^2 - |H_2'|^2) + \frac{1}{2} |\tilde{N}|^2 + ... \right]. \tag{4.3}$$

Here g_{B-L} is the gauge coupling of $U(1)_{B-L}$, and $+Q_1$, $-Q_1$, $1/2$ are the $B-L$ charges of H_1', H_2', $\tilde{N}$ respectively ($\tilde{N}$ is the sneutrino field). The $U(1)_{B-L}$ is broken by the vacuum expectation value (VEV) of H_1' and H_2', which we denote by v_1' and v_2' respectively. This results in a mass $m_{Z'} = g_{B-L} Q_1 \sqrt{v_1'^2 + v_2'^2}$ for the Z' gauge boson. We have three physical Higgs fields ϕ, Φ (scalars) and $\mathcal{A}$ (a pseudo scalar). The scalar Higgses are related to the real parts of H'_1, H'_2 through the mixing angle α':

$$\begin{aligned} H'_1 &= \frac{v'_1 + \cos\alpha'\Phi - \sin\alpha'\phi}{\sqrt{2}} + \frac{H'_{1,I}}{\sqrt{2}} \\ H'_2 &= \frac{v'_2 + \sin\alpha'\Phi + \cos\alpha'\phi}{\sqrt{2}} + \frac{H'_{2,I}}{\sqrt{2}}\,, \end{aligned} \tag{4.4}$$

where $H'_{1,I}$, $H'_{2,I}$ represent the imaginary parts. Eqs. (4.2,4.3,4.4) lead to the following terms in the scalar potential

$$\begin{aligned} V \supset\ & -\frac{1}{2} g_{B-L} m_{Z'} \sin(\alpha' + \beta')\, \phi\, |\tilde{N}|^2 \\ & -\frac{1}{2} g^2_{B-L} Q_1 \cos(2\alpha')\, \phi^2\, |\tilde{N}|^2 \\ & +\frac{1}{2} g_{B-L} m_{Z'} \cos(\alpha' + \beta')\, \Phi\, |\tilde{N}|^2 \\ & + \dots\,, \end{aligned} \tag{4.5}$$

where $\tan\beta' \equiv v'_2/v'_1$. The masses of the Higgs fields follow $m^2_\phi < \cos^2(2\beta')\, m^2_{Z'}$ and m_Φ, $m_{\mathcal{A}} \sim m_{Z'}$.

A natural dark matter candidate in this model is the sneutrino $\tilde{N}$ [1]. We note that the $\tilde{N}$ has fewer gauge interactions than other fields, hence its mass receives the smallest contribution from the gaugino loops. The main processes for annihilation of dark matter quanta are then governed by interactions in Eq. (4.5). The dominant channel is $\tilde{N}^*\tilde{N} \rightarrow \phi\phi$ via the s-channel exchange of the ϕ, Φ, the t, u-channel exchange of the $\tilde{N}$, and the contact term $|\tilde{N}|^2\phi^2$. The s-channel Z' exchange is subdominant because of the large Z' mass (as required by the experimental bound on $m_{Z'}$). There are also $\tilde{N}^*\tilde{N} \rightarrow \phi\Phi$, $\phi\mathcal{A}$, $\Phi\Phi$, $\mathcal{A}\mathcal{A}$ annihilation processes, but

---

[1] Another candidate is the lightest neutralino in the new sector, which is a linear combination of the $U(1)_{B-L}$ gaugino $\widetilde{Z}'$ and the two Higgsinos $\widetilde{H}'_1$, $\widetilde{H}'_2$ [1, 69].

they are kinematically suppressed and/or forbidden for the parameter space we are considering. The sneutrinos can also annihilate to RH neutrinos via t-channel neutralino exchange. Again for the parameter space that we consider the annihilation into $\nu\bar{\nu}$ final states is at least an order of magnitude below the $\phi\phi$ final states. Other fermion final states, through s-channel Z' exchange, have even smaller branching ratios. Moreover, note that the annihilations to fermion-antifermion final states are P-wave suppressed.

The ϕ subsequently decays into fermion-antifermion pairs via a one-loop diagram containing two Z' bosons. The decay rate is given by:

$$\Gamma(\phi \to f\bar{f}) = \frac{C_f}{2^7\pi^5}\frac{g_{B-L}^6 Q_f^4 Q_\phi^2 m_\phi^5 m_f^2}{m_{Z'}^6}\left(1 - \frac{4m_f^2}{m_\phi^2}\right)^{3/2}, \tag{4.6}$$

where Q_f and Q_ϕ are the $B-L$ charges of the final state fermion and the ϕ respectively, m_f is the fermion mass, and C_f denotes color factor. Since the $B-L$ charge of leptons is three times larger than that of quarks, the leptonic branching ratio is naturally larger than that for quarks. We note that m_ϕ can be controlled by the VEVs of the new Higgs fields and for comparable VEVs, i.e. for $\tan\beta' \approx 1$, it can be very small compared to $m_{Z'}$. For $m_\phi > 2\,m_b$ the dominant decay mode is $\phi \to \tau^-\tau^+$ final state, while the branching ratio for the $\phi \to b\bar{b}$ mode is ≈ 7 times smaller.

The annihilation cross section at the present time has Sommerfeld enhancement as a result of the attractive force between sneutrinos due to the ϕ exchange. The Higgs coupling to dark matter is given by the first term on the RH side of Eq. (4.5) and leads to an attractive potential $V(r) = -\alpha(e^{-m_\phi r}/r)$ in the non-relativistic limit [41], where

$$\alpha = \frac{g_{B-L} m_{Z'} \sin(\alpha' + \beta')}{4m_{\tilde{N}}}, \tag{4.7}$$

and $m_{\tilde{N}}$ is the sneutrino mass.

Fields	Q	Q^c	L	L^c	H'_1	H'_2
Q_{B-L}	1/6	-1/6	-1/2	1/2	3/2	-3/2

Table 4.1: The $B-L$ charges of the fields for the minimal model. Here Q and L represent quarks and leptons respectively, while H'_1 and H'_2 are the two new Higgs fields. The MSSM Higgs fields have zero $B-L$ charges.

4.3 Sneutrino dark matter and PAMELA

We are now going to show that the sneutrino dark matter can explain the PAMELA data. We first identify the allowed regions of the model parameter space that result in an acceptable dark matter relic density and then find the Sommerfeld enhancement factor for these regions. For an explicit example, which we call the minimal model, we choose the $B-L$ charge for H'_1 (i.e. Q_1) to be 3/2. The $B-L$ charges of the fields involved are shown in Table 4.1. We use reasonable values for the model parameters, i.e., $\tan\beta' \approx 1$, $m_{Z'} > 1.5$ TeV, $\mu' = 0.5 - 1.5$ TeV (μ' being the Higgs mixing parameter in the $B-L$ sector), soft masses for the Higgs fields $m_{H'_{1,2}} = 200-600$ GeV, and soft gaugino mass $M_{\tilde{Z}'} \geq 1$ TeV. We use $g_{B-L} \sim 0.40$, which is in concordance with unification of the gauge couplings (we need to use a normalization factor $\sqrt{3/2}$ for unification). We show the unification of all the gauge couplings using the two loop renormalization group equations (RGEs) in Figure 4.1. We find that for $m_{Z'} \simeq 2.5$ TeV the couplings unify at $\sim 10^{16}$ GeV. This figure is drawn for the $B-L$ assignments shown in Table 4.1. The Z' mass used in the calculation obeys the LEP and Tevatron bounds [70, 71] for our charge assignments. The sneutrino mass is chosen to be between 800 GeV and 2 TeV in order to explain the PAMELA (and ATIC) data.

In Figure 4.2, we show the relic density and the sneutrino mass for different model points. The horizontal band shows the acceptable range for relic density according to the latest WMAP data [53]. In Figure 4.3 we show the possible Sommerfeld enhancement factor R that can be obtained for these points in term of $\epsilon_\phi \equiv m_\phi/\alpha m_{\tilde{N}}$.

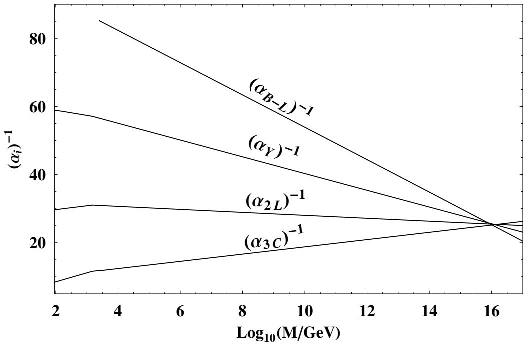

Figure 4.1: We show the unification of gauge couplings for the $B - L$ charge assignments in Table 1 using two loop RGEs.

Note that many of the points that satisfy the relic density constraint have enhancement factor $R \geq 10^3$, corresponding to $\epsilon_\phi = 0.55$ to 0.65. This is true for the whole range of $m_{\tilde{N}}$ shown in Figure 4.2. The lifetime of ϕ for these points is found to be $\tau_\phi \sim 10^{-5} - 10^{-4}$ seconds from Eq. (4.6). Thus ϕ's produced in the early universe decay rapidly enough in order not to affect big bang nucleosynthesis (BBN) [72][2]. We select points that satisfy the dark matter relic density and then use `DarkSUSY`-5.0.2 [73] to calculate the positron flux from dark matter annihilation. Each pair annihilation in our model produces 2 ϕ's that yield four fermions upon their decay. For this reason, we generally need a heavier sneutrino compared to models in which the pair annihilation directly produces fermions. We normalize the positron fraction by a factor $k_b = 1.11$ [74]. There are theoretical uncertainties in the positron cosmic ray flux calculation due to the assumptions about the dark matter halo profile and the cosmic ray propagation model. Here we assume NFW profile [75] for the dark matter halo and MED parameters for the propagation as defined in [76].

---

[2] Since dark matter particles are non-relativistic at the time of BBN, their annihilation enhanced by Sommerfeld effect can result in significant electromagnetic and/or hadronic showers that dissociate light elements from BBN. For muon final states, the large enhancement factor required to explain PAMELA is compatible with BBN bounds, while for tau final states a small astrophysical boost factor seems to be needed in order not to affect BBN [82].

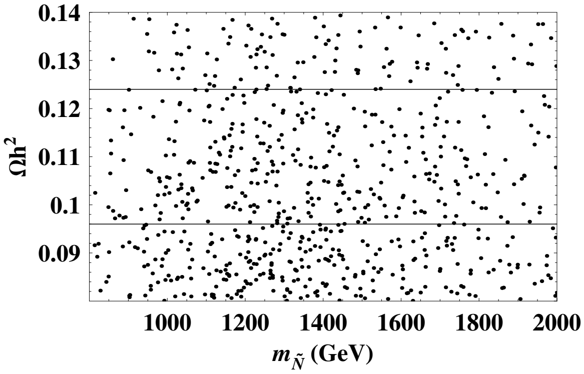

Figure 4.2: We show the relic density and the sneutrino mass for model points generated by varying the parameters mentioned in the text.

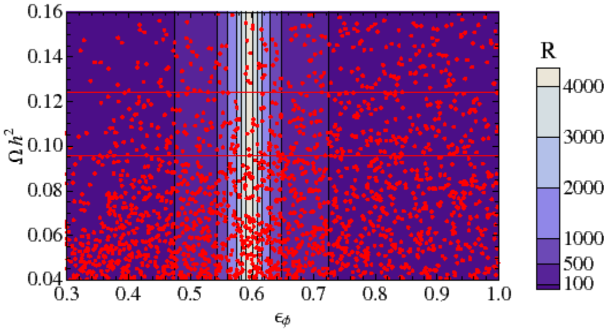

Figure 4.3: We show relic density as a function of ϵ_ϕ. We show different ranges for the Sommerfeld enhancement factor R by shaded contours.

In Figure 4.4, we show our fit to the PAMELA data for $m_{\tilde{N}} = 1.5$ TeV for $\tau^+\tau^-$ and $\mu^+\mu^-$ final state cases. We found that with an enhancement factor of 10^3 the chi-square values (including only points with energy greater than 10 GeV) for a sneutrino mass of 1.5 TeV are small, i.e. 2.9 and 5.5 for $\tau^+\tau^-$ and $\mu^+\mu^-$ respectively. When m_ϕ is (chosen to be) below $2\,m_b$ but above $2\,m_\tau$, we do not have any anti-proton excess. In fact we can raise m_ϕ up to ~ 15 GeV and still have acceptable anti-proton flux. We can also have a reasonable fit to the ATIC data, although simultaneous fit for both ATIC and PAMELA are not satisfactory [1].

We note that this model also has a great potential to be observed with the Fermi

Satellite experiment. Due to electromagnetically charged final states of ϕ decays, the Sommerfeld enhancement would also lead to a higher rate of photons in the gamma ray background [83]. There could also be contribution to the neutrino flux [84].

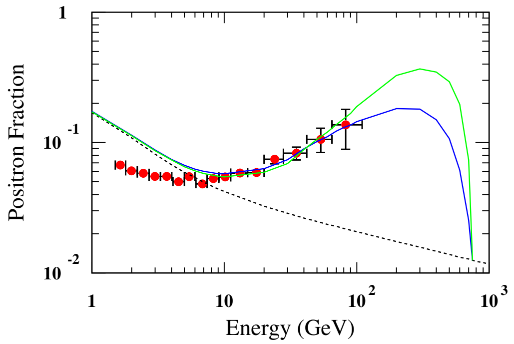

Figure 4.4: We show a fit to the PAMELA data when the ϕ decays mostly to taus (dark blue) or muons (light green) for a sneutrino mass of 1.5 TeV and an enhancement factor of 10^3. The dashed line is the expected background cosmic rays.

4.4 Direct Detection

The current upper bound on the spin-independent dark matter particle-proton scattering cross section is about 4.6×10^{-8} pb for a dark matter mass around 60 GeV, and increasing to $\sim 2 \times 10^{-7}$ pb for a mass around 1.2 TeV [85]. In our model the elastic scattering of the sneutrino occurs via the Z' exchange with the nucleus in the t-channel. This leads to only a spin-independent contribution since the $B-L$ charges of the left and right quarks are the same. In Figure 4.5, we show the $\tilde{N}$-p scattering cross section for the model points in Figure 1 that satisfy the relic density constraint $0.096 < \Omega_{DM}h^2 < 0.124$. We see that the cross section can be in the $10^{-11} - 10^{-9}$ pb range, which is close to the reach of the upcoming dark matter direct detection experiments [86].

It is also seen that the cross section decreases as the sneutrino mass increases. This is because for larger values of $m_{\tilde{N}}$ we also need a larger annihilation cross section to satisfy the relic density constraint. As discussed earlier the annihilation cross section depends on the sneutrino couplings to ϕ and Φ, see Eq. (4.5), which are $\propto m_{Z'}$.

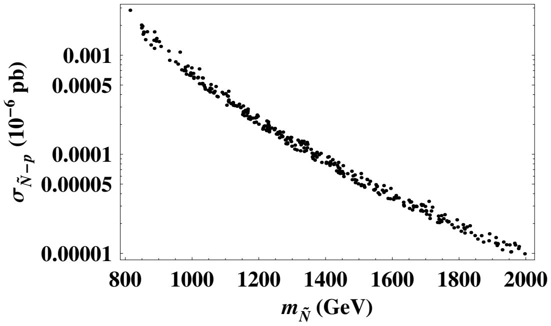

Figure 4.5: We show the direct detection cross section as a function of sneutrino mass.

It is interesting to note that within this mass range the Z' can be produced at the LHC. The Z' decay will produce the new light Higgs ϕ (among other fields). However, ϕ will decay outside of the detector because of its relatively long life time ($\sim 10^{-5}$ sec). Thus, in addition to the sneutrino LSP, we have another source of missing energy signal in this model [3].

4.5 Radiative breaking of $B-L$ symmetry

In order to have spontaneous breaking of $U(1)_{B-L}$ we need a negative eigenvalue in the H'_1, H'_2 square-mass matrix. This can arise dynamically as a result of radiative corrections to the Higgs soft masses. Here we discuss two generic possibilities.

---

[3] We also note that there are 7 neutralinos in this model, compared to four in the MSSM, while the number of charginos is still two. Therefore, using the end point analysis [78], one can find many neutral states.

4.5.1 Higgs coupling to right-handed neutrinos

If $Q_1 = 1$, then H_2' can have a superpotential coupling to the RH neutrinos [4]. In this case we have:

$$W_{B-L} = f\mathbf{H_2'}\mathbf{N}^c\mathbf{N}^c + \mu'\mathbf{H_1'}\mathbf{H_2'}, \tag{4.8}$$

where μ' is analogous to the MSSM μ parameter. Note that in the minimal model, with $Q_1 = 3/2$, the H_2' can only couple to H_1' in the superpotential. Taking the soft mass parameters into account, the Higgs potential is

$$(m_1^2 + \mu'^2)|H_1'|^2 + (m_2^2 + \mu'^2)|H_2'|^2 + (B\mu' H_1' H_2' + \text{h.c}) \,. \tag{4.9}$$

(Here the parameters m_1, m_2, B are not to be confused with the MSSM Higgs parameters.) The Yukawa coupling between $\mathbf{H_2'}$ and $\mathbf{N}^c$ can drive m_2^2 to a sufficiently negative value such that $m_2^2 + \mu'^2 < 0$ around the TeV energy scale [5]. This requires that f not be very small. On the other hand, f should not be very large. Otherwise there would be a one-loop correction that lifts the ϕ mass above its tree-level limit $m_\phi^2 < M_{Z'}^2 \cos^2(2\beta')$ (similar to the correction from the top Yukawa in the MSSM [87]):

$$\Delta m_\phi^2 \sim \frac{1}{16\pi^2} f^2 m_N^2 \ln\left[\frac{m_N^2}{m_{\tilde{N}_R} m_{\tilde{N}_I}}\right] . \tag{4.10}$$

Here $m_N = \sqrt{2} f v_2'$ is the Majorana mass of N and

$$\begin{aligned} m_{\tilde{N}_R} &= \left[m_{\tilde{N}}^2 + m_N(A+\mu')\right]^{1/2} \\ m_{\tilde{N}_I} &= \left[m_{\tilde{N}}^2 - m_N(A+\mu')\right]^{1/2} \,, \end{aligned} \tag{4.11}$$

---

[4] Similarly, H_1' can couple to the RH neutrinos if $Q_1 = -1$.

[5] Since H_1' has no Yukawa couplings, m_1^2 increases towards smaller scales because of the $U(1)_{B-L}$ gaugino loop.

are the total masses of the real and imaginary parts of the $\tilde{N}$ respectively. The mass splitting is due to the contribution of the A and μ' terms to the $\tilde{N}$ potential given by

$$f\left(AH_2' + \mu' H_1'^*\right)\tilde{N}\tilde{N} + \text{h.c.} \tag{4.12}$$

For simplicity we have assumed that f, A and μ' are real, and we have used the requirement that $v_1' \approx v_2'$. This mass splitting can lift m_ϕ above its tree-level limit similar to the effect from stop mixing in the MSSM [87]. In order for this not to be significant, it will be sufficient to have $|A + \mu'| \ll m_{\tilde{N}}$ at the TeV scale [6].

In our case the sneutrino and the neutrino masses can be close and therefore the corrections to the Higgs mass can be very small < 10 GeV (which we have checked numerically). In fact, this allows us to keep the Higgs mass below 15 GeV such that we do not have any problems with anti-proton data. We also have found that $f \sim 0.2$ is large enough to lead to radiative breaking of $U(1)_{B-L}$. Assuming grand unification, one should use the SUGRA boundary conditions to achieve radiative breaking due to the smallness of f (as compared with the top Yukawa in the MSSM). The appropriate boundary conditions are such that $m_1^2 = m_2^2 < 0$, but $m_{1,2}^2 + \mu'^2 > 0$, while all other soft (mass)^2 are positive at the grand unification scale.

The potential term in Eq. (4.12), no matter how small, inevitably splits the masses of the real and imaginary parts of the sneutrino. In this case dark matter will be the lighter of $\tilde{N}_R$ and $\tilde{N}_I$, which we choose to be $\tilde{N}_R$ without loss of generality. Then the heavier component $\tilde{N}_I$ decays to dark matter and fermions via an off-shell Z' in the early universe. In this case the dark matter coupling to the light Higgs ϕ, the first term on the RH side of Eq. (4.5), will be twice as small as the term wherein the dark matter is a complex field. However the attractive potential, due to

---

[6] This also ensures that the contribution of Eq. (4.12) to the coupling of dark matter to ϕ, Φ is negligible compared with that from the D-term (4.5).

ϕ exchange, will be the same in the two cases. This is because a real field annihilates and creates the same quanta, thus giving rise to a factor of two that compensates the 1/2 that appears in the coupling. The same also holds for dark matter annihilation. Therefore, as far as relic density calculations and the Sommerfeld enhancement factor are concerned, our results will not depend on whether dark matter is the complex $\tilde{N}$ field or its real (or imaginary) component.

We also note that the $f\mathbf{H'_2}\mathbf{N}^c\mathbf{N}^c$ term opens a new channel for the decay of the light Higgs ϕ. Since $m_\phi \ll m_N$, the decay to on-shell RH neutrinos is not possible. The decay can happen via off-shell N through their couplings to the MSSM fields (4.1), at higher orders of perturbation theory. Then, if the neutrino Dirac Yukawa coupling y_D is sufficiently small, this decay mode will be totally negligible. Indeed this is the case since the see-saw mechanism at the TeV scale requires $y_D \lesssim 10^{-6}$ to generate the observed neutrino masses.

4.5.2 Higgs coupling to other fields

If $Q_1 \neq \pm 1$, then neither H'_1 nor H'_2 can have a superpotential coupling to N. This happens, for example, if $Q_1 = 1/2$ [68] or $Q_1 = 3/2$ (as chosen above for the minimal model and also in [1]). Radiative breaking of $U(1)_{B-L}$ then requires a moderate Yukawa coupling of one of the $B-L$ Higgses to the new fields.

A simple model of this type includes two new superfields $\mathbf{\Phi_1}$, $\mathbf{\Phi_2}$ and has the following superpotential

$$\begin{aligned} W_{B-L} &= \mu'\mathbf{H'_1}\mathbf{H'_2} + f_1\mathbf{H'_1}\mathbf{\Phi_1}\mathbf{\Phi_1} + f_2\mathbf{H'_2}\mathbf{\Phi_2}\mathbf{\Phi_2} \\ &+ \mu''\mathbf{\Phi_1}\mathbf{\Phi_2} + \lambda\mathbf{\Phi_1}\mathbf{N}^c\mathbf{N}^c\,, \end{aligned} \tag{4.13}$$

where $Q_1 = 2$ and the $B-L$ charges of $\mathbf{\Phi_1}$, $\mathbf{\Phi_2}$ are $-1, \ +1$ respectively. All we need for radiative breaking of $U(1)_{B-L}$ is $f_1 \sim 0.2$, or $f_2 \sim 0.2$ (one of the couplings can be very small) and SUGRA boundary conditions. This ensures sufficiently large loop corrections that drive the $(\text{mass})^2$ of the corresponding Higgs field to negative values around a TeV. In this case, since the Higgs fields are not coupled to $\mathbf{N}^c$, there are no Majorana masses for the RH neutrinos, and hence neutrinos are of a Dirac nature. Also, there will be no splitting between the masses of the real and imaginary parts of the $\tilde{N}$, and thus the dark matter is a complex scalar field.

Interactions in the first line of Eq. (4.13) result in a 2×2 mass matrix for $\mathbf{\Phi_1},\ \mathbf{\Phi_2}$. For large enough μ'' (i.e. $\mu'' \sim v'_1,\ v'_2$) the mass eigenvalues will be larger than the sneutrino mass. Hence the corresponding mass eigenstates would quickly decay to the RH neutrino and sneutrino through the $\lambda \mathbf{\Phi_1} \mathbf{N}^c \mathbf{N}^c$ superpotential term in the early universe. The $f_1 \mathbf{H'_1} \mathbf{\Phi_1} \mathbf{\Phi_1}$ and $\lambda \mathbf{\Phi_1} \mathbf{N}^c \mathbf{N}^c$ terms also open a new decay channel for the light Higgs: $\phi \to 4N$ via off-shell fermionic components of Φ_1 [7]. However, λ can be chosen to be sufficiently small such that $\phi \to \tau^- \tau^+$ remains the dominant decay mode of ϕ.

If $Q_1 = 3/2$, as chosen in Table 1, one can introduce four new superfields $\mathbf{\Phi_1},\ \mathbf{\Phi_2},\ \mathbf{\Phi_3},\ \mathbf{\Phi_4}$ (with respective $B - L$ charges $-1,\ +1,\ -1/2,\ +1/2$) and the following superpotential

$$\begin{aligned} W_{B-L} &= \mu' \mathbf{H'_1} \mathbf{H'_2} + f_1 \mathbf{H'_1} \mathbf{\Phi_1} \mathbf{\Phi_3} + f_2 \mathbf{H'_2} \mathbf{\Phi_2} \mathbf{\Phi_4} \\ &+ \mu'' \mathbf{\Phi_1} \mathbf{\Phi_2} + \mu''' \mathbf{\Phi_3} \mathbf{\Phi_4} + \lambda \mathbf{\Phi_1} \mathbf{N}^c \mathbf{N}^c \,. \end{aligned} \tag{4.14}$$

Again the mass eigenvalues of the 4×4 mass matrix for $\mathbf{\Phi_1},\ \mathbf{\Phi_2},\ \mathbf{\Phi_3},\ \mathbf{\Phi_4}$ can be made large enough such that the corresponding eigenstates rapidly decay to lighter fields via the $\lambda \mathbf{\Phi_1} \mathbf{N}^c \mathbf{N}^c$ superpotential terms.

---

[7] Note that there can be no $\tilde{N}$ in the final state since $m_\phi \ll m_{\tilde{N}}$.

It is interesting to note that although we have used $Q_1 = 3/2$ to obtain the results in the previous sections, they are largely independent from the exact charge assignments of H_1', H_2'. This is because the major contributions to relic density calculations involve Z' mass in the coupling and Q_1 is already absorbed in the mass definition, see Eq. (4.5). The direct detection cross section also remains unchanged for the same reason. The gauge coupling unification still occurs but requires a larger value of g_{B-L} for $|Q_1| < 3/2$. Therefore Eqs. (4.8,4.13,4.14) can all yield thermal sneutrino dark matter with a large Sommerfeld enhancement factor and radiative breaking of $U(1)_{B-L}$.

4.6 Right-handed sneutrino and inflation

In addition to being the dark matter candidate, the RH sneutrino can also drive inflation in the context of the $U(1)_{B-L}$ model [67, 68]. The gauge-invariant combination $\mathbf{N}^c\mathbf{H_u}\mathbf{L}$ forms a D-flat direction under the whole gauge symmetry $SU(3)_C \times SU(2)_L \times U(1)_Y \times U(1)_{B-L}$. The flat direction field φ is defined as

$$\varphi = \frac{\tilde{N} + H_u + \tilde{L}}{\sqrt{3}}. \tag{4.15}$$

The potential along the flat direction, after the minimization along the angular direction, is found to be [67],

$$V(|\varphi|) = \frac{m_\varphi^2}{2}|\varphi|^2 + \frac{y_D^2}{12}|\varphi|^4 - \frac{A y_D}{6\sqrt{3}}|\varphi|^3, \tag{4.16}$$

where y_D is the neutrino Dirac Yukawa (4.1) and A is the corresponding A-term coupling. The flat direction mass m_φ is given in terms of the $\tilde{N}$, H_u, $\tilde{L}$ masses:

$$m_\varphi^2 = \frac{m_{\tilde{N}}^2 + m_{H_u}^2 + m_{\tilde{L}}^2}{3}. \tag{4.17}$$

For $A \approx 4m_\varphi$, there exists an inflection point φ_0 for which $V''(\varphi_0) = 0$. Due to the extreme flatness of the potential around the inflection point, inflation can take place near φ_0. The amplitude of density perturbations generated during inflation follows [67]

$$\delta_H \simeq 3.5 \times 10^{-27} \left(\frac{y_D \langle H_u \rangle}{0.05 \text{ eV}}\right)^2 \left(\frac{M_\text{P}}{m_\varphi}\right) \mathcal{N}_\text{COBE}^2 \,, \tag{4.18}$$

where $\langle H_u \rangle \simeq 174$ GeV and $\mathcal{N}_\text{COBE} \sim 50$ is the number of e-foldings between the time that relevant perturbations were produced and the end of inflation. It is seen from Eq. (4.18) that perturbations of the correct size $\delta_H = 1.91 \times 10^{-5}$ are obtained if $y_D \sim 10^{-12}$. Interestingly this is the typical neutrino Dirac Yukawa coupling that gives rise to the mass scale $m_\nu \simeq 0.05$ eV required to explain the atmospheric neutrino oscillations detected by the Super-Kamiokande experiment [88] if neutrinos are dominantly Dirac in nature.

Dirac neutrinos can be achieved in both cases considered above (4.8,4.13). If the Higgs fields that break $U(1)_{B-L}$ are not coupled to $\mathbf{N}^c$ (4.13), the neutrinos are naturally Dirac since there will be no Majorana masses for the RH neutrinos in this case, regardless of how big the couplings f_1, f_2 are. On the other hand, a superpotential coupling between the Higgs that breaks $U(1)_{B-L}$ and $\mathbf{N}^c$, see Eq. (4.8), inevitably induces a Majorana mass $m_N = 2f\langle H_2' \rangle$ to the RH neutrinos upon the $B-L$ breaking. Nevertheless, the main contribution to the mass of light neutrinos comes from the Dirac Yukawa coupling y_D. Hence all that we need in this case is one of the Majorana masses (out of the three generations) to be very small in order to have an almost Dirac neutrino with $y_D \sim 10^{-12}$. The other Majorana masses (and respectively the coupling f) can be large.

We therefore conclude that it is possible to have a unified $U(1)_{B-L}$ model of inflation and dark matter, where the RH sneutrino is the dark matter and a component of the inflaton field [68].

4.7 Conclusion

Motivated by the recently reported cosmic ray anomalies, we have reconsidered a minimal extension of the MSSM that includes a gauged $U(1)_{B-L}$. This additional symmetry is broken around a TeV by two new Higgs fields that carry non-zero $B-L$ charges. The RH sneutrino can naturally be the dark matter candidate in this model since it has the smallest gauge interactions among all the fields. Sneutrino interactions of gauge strength yield an acceptable thermal relic density in large regions of the parameter space. If the lightest Higgs in the $B-L$ sector is much lighter than a TeV, the dark matter dominantly annihilates into final states including this Higgs. The annihilation is governed by D-term couplings between the sneutrino and the Higgs and takes place in the S-wave. The light Higgs subsequently decays to fermions and the $B-L$ symmetry guarantees that the branching ratio for producing leptons is several times larger than that for quarks, which agrees with the observation of positron and anti-proton fluxes by PAMELA. For a $1-2$ TeV sneutrino, a Higgs mass ≤ 15 GeV will result in a large Sommerfeld enhancement factor $\mathcal{O}(10^3)$ in the annihilation cross section at the present time. This provides a good fit to the PAMELA data and a reasonable fit to the ATIC data.

The sneutrino interacts with quarks via t-channel exchange of the $U(1)_{B-L}$ gauge boson Z'. The interaction only has a spin-independent part since $B-L$ is a vector symmetry. The resulting sneutrino-nucleon elastic scattering cross section is found to be $10^{-11}-10^{-9}$ pb, which might be within the reach of future direct detection experiments.

We have also discussed radiative breaking of $U(1)_{B-L}$. This requires that (one of) the $B-L$ Higgs fields have a relatively large Yukawa coupling to the RH sneutrino or some other field. A Yukawa coupling ~ 0.2 is sufficient to induce radiative breaking while keeping the mass of the light Higgs low enough to give rise to considerable

Sommerfeld enhancement of dark matter annihilation.

Finally, if (at least) one of the neutrinos is dominantly a Dirac fermion, the sneutrino can be part of the inflaton field in addition to being the dark matter. This is a very appealing scenario since direct and indirect detection experiments not only probe dark matter in this case, but they can also reveal the interactions of the inflaton, which is supposed to be the most elusive particle in the universe.

4.8 Acknowledgement

The work of BD is supported in part by DOE grant DE-FG02-95ER40917.

Chapter 5

Prospects for indirect detection of sneutrino Dark Matter with IceCube

Major Results

Having established in the previous chapter the viability of a right-handed sneutrino as the LSP, this chapter investigates whether or not such an LSP could be distinguished from the traditional Majorana fermion neutralinos produced by mSUGRA hyperbolic branch/focus point models. The work of this chapter was conducted in collaboration with co-authors Drs. Rouzbeh Allahverdi, Sascha Bornhauser and Bhaskar Dutta and was published in Physical Review D [3].

First we find that for dark matter to come to an equilibrium in the sun so that two particles are captured for every annihilation, a cross section of 10^{-8} pb is necessary for a freeze-out annihilation rate of $3 \times 10^{-26}\text{cm}^3/\text{s}$. Equilibrium is necessary for the IceCube neutrino telescopes to detect a DM signal. For Sommerfeld enhanced models, the requirement on the WIMP-nucleon cross section may be relaxed inverse to the enhancement. The derived values put the $B - L$ model smartly in the territory of contemporary direct detection experiments. The monochromatic neutrinos produced in right-handed sneutrino annihilation produce a characteristic linear spectrum of muon tracks in the IceCube neutrino telescope. Integrating the energy spectrum demonstrates that this model is within the sensitivity range of IceCube.

Additionally, if a dark matter disc is present enhancing the local density of DM through which the earth sweeps, the earth may accumulate sufficient dark matter to reach equilibrium and produce a viable signal from DM accumulated in the earth without spoiling limits on the signal from the sun. At a 400 GeV mass, counts of muon track events are roughly equivalent between mSUGRA models and the sneutrino case. This occurs even though predicted capture rates differ by orders of magnitude because the focus point models annihlate to the relatively soft quark final state compared to the more energetic, leptophilic annihilation of sneutrinos.

Abstract

We investigate the prospects for indirect detection of right-handed sneutrino dark matter at the IceCube neutrino telescope in a $U(1)_{B-L}$ extension of the MSSM. The capture and annihilation of sneutrinos inside the Sun reach equilibrium, and the flux of produced neutrinos is governed by the sneutrino-proton elastic scattering cross section, which has an upper bound of 8×10^{-9} pb from the Z' mass limits in the $B-L$ model. Despite the absence of any spin-dependent contribution, the muon event rates predicted by this model can be detected at IceCube since sneutrinos mainly annihilate into leptonic final states by virtue of the fermion $B-L$ charges. These subsequently decay to neutrinos with 100% efficiency. The Earth muon event rates are too small to be detected for the standard halo model irrespective of an enhanced sneutrino annihilation cross section that can explain the recent PAMELA data. For modified velocity distributions, the Earth muon events increase substantially and can be greater than the IceCube detection threshold of 12 events km^{-2} yr^{-1}. However, this only leads to a mild increase of about 30% for the Sun muon events. The number of muon events from the Sun can be as large as roughly 100 events km^{-2} yr^{-1} for this model.

5.1 Introduction

There are various lines of evidence supporting the existence of dark matter in the universe, but its identity remains a major problem the solution to which likely rests at the interface of particle physics and cosmology. It is well established that particle physics can explain dark matter in the form of weakly interacting massive particles (WIMPs) [79]. In the standard scenario the dark matter relic abundance, as precisely measured by cosmic microwave background (CMB) experiments [53] is determined from the thermal freeze out of dark matter annihilation in the early universe. There are currently major experimental efforts for direct and indirect detection of dark matter particles. Indirect detection investigates annihilation of dark matter to various final states (photons, anti-particles, neutrinos) through astrophysical observations, while direct detection probes the scattering of the dark matter particle off nuclei inside dark matter detectors.

Supersymmetry is a front-runner candidate to address the hierarchy problem of the standard model (SM). The minimal supersymmetric standard model (MSSM) has become the focus of major theoretical and experimental activities for the past two decades. It has a natural dark matter candidate, namely the lightest supersymmetric particle (LSP), which can have the correct thermal relic abundance [54]. It is also believed that there are gauge symmetries beyond those of the SM. A minimal extension of the SM gauge group, motivated by the nonzero neutrino masses, includes a gauged $U(1)_{B-L}$ gauge symmetry [66] (B and L are baryon and lepton number respectively). Anomaly cancellation then implies the existence of three right-handed (RH) neutrinos and allows us to write the Dirac and Majorana mass terms for the neutrinos to explain the light neutrino masses and mixings.

The $B-L$ extended MSSM also provides new dark matter candidates: the lightest neutralino in the $B-L$ sector [69, 1] and the lightest RH sneutrino [68]. In this work we will focus on the sneutrino as the dark matter candidate[1]. The candidate is made stable by invoking a discrete R-parity, but in the context of a $B-L$ symmetry, a discrete matter parity can arise once the $U(1)_{B-L}$ is spontaneously broken [89]. The $B-L$ gauge interactions can yield the correct relic abundance of sneutrinos if the $U(1)_{B-L}$ is broken around the TeV scale.

---

[1] It is also possible to have successful inflation in the context of the $U(1)_{B-L}$ model [67]. In this case the dark matter candidate (the RH sneutrino) can become a part of the inflaton field and thereby gives rise to a unified picture of dark matter, inflation and the origin of neutrino masses [68].

Recently, it has been shown that it is possible to explain the positron excess observed in the PAMELA data [32, 33] in the context of a low scale $B-L$ extension of the MSSM [1, 2, 90]. Due to a factor of 3 difference between the $B-L$ charges of the quarks and leptons, the anti-proton flux is naturally suppressed in this model in agreement with the PAMELA anti-proton data. Furthermore, the $U(1)_{B-L}$ gauge coupling unifies with those of the SM symmetries, and the $B-L$ symmetry can be broken radiatively. The $B-L$ breaking around a TeV results in a Z' gauge boson with around a TeV mass that can be probed at the LHC along with the other new states of this model.

The RH sneutrino of this $B-L$ extended model can be detected when it elastically scatters off a nucleus. The sneutrino-proton scattering cross section is large enough to be probed in the ongoing and upcoming dark matter direct detection experiments [68]. In addition, annihilation of sneutrinos at the present time produces LH neutrinos. It is interesting to investigate the possibility of indirect detection of sneutrino dark matter by using final state neutrinos in the IceCube neutrino telescope. This ongoing experiment plans to probe the neutrino flux arising from the annihilation of gravitationally trapped dark matter particles in the Sun and the Earth. We will examine the status of the $U(1)_{B-L}$ model in two cases. In **case 1**, the sneutrinos annihilate mostly into RH neutrinos that subsequently decay into LH neutrinos and the MSSM Higgs. In **case 2**, the sneutrinos annihilate mostly into the lightest Higgs boson in the $B-L$ sector that decays into $\tau^+\tau^-$ and b^+b^- quarks, which subsequently produce LH neutrinos via three-body decays. The recent PAMELA data [32, 33] can be explained in **case 2**, where the final state taus give rise to the positron excess in the cosmic ray flux without producing a significant number of antiprotons [1, 2, 90]. The large cross section required to explain the data arises from Sommerfeld enhancement [41] or from the non-thermal production of dark matter [90].

Since the source of neutrinos are different in the two cases, two-body versus three-body decay, the energy spectrum of the neutrinos can be used to distinguish the cases. We will estimate the muon neutrino flux as well as the muon flux in both scenarios as a function of sneutrino mass. Since the Large Hadron Collider (LHC) is on the verge of producing physics results, it will enable us to measure the mass of the dark matter candidate. Therefore, using the LHC measurements and the IceCube results in tandem, we hope to discern the $B-L$ model. We will present predictions of this model using the standard dark matter halo model as well as the modified velocity distributions obtained in recent galaxy simulations.

This paper is organized as follows. In section II, we discuss the low scale $U(1)_{B-L}$ model. In section III, we give a general discussion of the indirect detection of sneutrino dark matter via neutrino final states. In section IV, we present our results and discuss the prospect of detection of sneutrino dark matter at IceCube in **case 1** and **case 2**. In section V, we show the results obtained for the modified velocity distributions. In section VI, we compare predictions for the sneutrino dark matter in the $U(1)_{B-L}$ model with those for the neutralino dark matter in the minimal supergravity model. Finally, we close by concluding in section VII.

5.2 The $U(1)_{B-L}$ Model

Since this $B-L$ is a local gauge symmetry, we have a new gauge boson Z' (and its supersymmetric partner). In the minimal model, we also have two new Higgs fields H'_1 and H'_2 (that are SM singlets) and their supersymmetric partners. The vacuum expectation values (VEVs) of these Higgs fields break the $B-L$ symmetry. We can write the superpotential of the model as follows (the boldface characters denote superfields)

$$W = W_{\text{MSSM}} + W_{B-L} + y_D \mathbf{N}\mathbf{H_u}\mathbf{L}\,, \tag{5.1}$$

where $\mathbf{H_u}$ and $\mathbf{L}$ are the superfields containing the Higgs field that gives mass to up-type quarks and the LH leptons respectively. For simplicity, we have omitted the family indices. The W_{B-L} term contains $\mathbf{H_1'}$, $\mathbf{H_2'}$ and $\mathbf{N}$ [2]. Its detailed form depends on the charge assignments of the new Higgs fields.

The $U(1)_{B-L}$ is broken by the VEV of H_1' and H_2', which we denote by v_1' and v_2' respectively. This results in a mass $m_{Z'}$ for the Z' gauge boson. We have three physical Higgs fields ϕ, Φ (scalars) and $\mathcal{A}$ (a pseudo scalar). The masses of the Higgs fields follow $m_\phi^2 < \cos^2(2\beta')m_{Z'}^2$ (where $\tan\beta' \equiv \langle H_2' \rangle / \langle H_1' \rangle$) and $m_\Phi,\ m_{\mathcal{A}} \sim m_{Z'}$.

Various $B-L$ charge assignments are allowed by anomaly cancelation. We choose the charge assignment shown in Table 1. In this case H_2' couples to the RH neutrinos and gives rise to a Majorana mass upon spontaneous breakdown of the $U(1)_{B-L}$. Choosing these Majorana masses in the 100 GeV − 1 TeV range, we have three (dominantly RH) heavy neutrinos and three (dominantly LH) light neutrinos. The masses of the light neutrinos are obtained via the see-saw mechanism.

Fields	Q	Q^c	L	L^c	H_1'	H_2'
Q_{B-L}	1/6	-1/6	-1/2	1/2	1	-1

Table 5.1: The $B-L$ charges of the fields for the minimal model. Here Q and L represent quarks and leptons respectively, while H_1' and H_2' are the two new Higgs fields. The MSSM Higgs fields have zero $B-L$ charges.

A natural dark matter candidate in this model is the lightest sneutrino $\widetilde{N}$. We note that it has fewer gauge interactions than other supersymmetric particles, and its mass receives the smallest contribution from the gaugino loops. Based on the dominant channel for sneutrino annihilation we therefore consider the following two cases:

- **Case 1**: A generic case where a solution to the positron excess observed by PAMELA is not sought. In this case the dominant annihilation channels are the S-wave processes $\widetilde{N}\widetilde{N} \to NN$ and $\widetilde{N}^*\widetilde{N}^* \to N^*N^*$ via t-channel exchange of $\widetilde{Z}'$. There are also $\widetilde{N}\widetilde{N}^* \to NN^*$, $f\bar{f}$ annihilation modes via s-channel exchange of a Z' or $B-L$ Higgs fields, but these are P-wave suppressed and can be completely neglected (particularly at the present time). In this case the annihilation cross-section has the nominal value $\sim 3 \times 10^{-26}$ cm^3/sec (dictated by thermal freeze out) at all times. The RH neutrinos produced from dark matter annihilation quickly decay to LH neutrinos and the MSSM Higgs.

- **Case 2**: In this case the PAMELA puzzle is addressed via Sommerfeld enhancement of sneutrino annihilation at the present time [2]. In this part of the model parameter space the lightest $B-L$ Higgs ϕ is much lighter than the Z'. The dominant annihilation channel is $\widetilde{N}^*\widetilde{N} \to \phi\phi$ via the s-channel exchange of the ϕ or Φ, the t or u-channel exchange of a $\widetilde{N}$, and the contact term $|\widetilde{N}|^2\phi^2$. The interactions for these processes arise from the D-term part of the potential, and their strength is proportional to $m_{Z'}$. There are other S-wave processes with Higgs final states $\widetilde{N}^*\widetilde{N} \to \phi\Phi$, $\phi\mathcal{A}$, $\Phi\Phi$, $\mathcal{A}\mathcal{A}$, but they are kinematically suppressed and/or forbidden. The annihilation modes $\widetilde{N}\widetilde{N} \to NN$ and $\widetilde{N}^*\widetilde{N}^* \to N^*N^*$ are also subdominant in this case. As in the previous case, annihilations to $f\bar{f}$ final states are P-wave suppressed and hence totally negligible. The cross section for annihilation to the $\phi\phi$ final state at the present time is required to be 3×10^{-23} cm^3/sec in order to explain the PAMELA data. Sufficient Sommerfeld enhancement is obtained as a result of the attractive force between sneutrinos due to the ϕ exchange provided that the mass of ϕ is small ($<$ 20 GeV)[2]. The ϕ subsequently decays into fermion-

---

[2] It is possible to invoke a non-thermal scenario where the sneutrinos are created from the decay of heavy moduli or gravitinos [90]. In this case we do not need Sommerfeld enhancement to satisfy the PAMELA data, and the annihilation cross section will be large, 3×10^{-23} cm^3/sec, at all times.

antifermion pairs very quickly via a one-loop diagram, and it mostly produces $\tau^+\tau^-$ final states by virtue of the fermion $B-L$ charges [2].

The sneutrino-proton scattering cross section for this model can be in the $10^{-11}-10^{-8}$ pb range for a reasonable choice of parameters that satisfy the relic density constraint, cf. [68, 2]. This opens up the prospect for direct detection with the help of the next generation of experiments [86]. The current upper bound for the spin-independent cross section is $4.6\times10^{-8}-2\times10^{-7}$ pb for a dark matter mass of $60-1200$ GeV; this is just above the highest possible values for our model[3].

5.3 Prospects for Indirect Detection at IceCube

5.3.1 The Neutrino Signal

The $B-L$ model also shows great promise for indirect detection, and we focus in particular on the potential neutrino signal at the IceCube experiment. In **case 1**, the sneutrinos annihilate to produce RH neutrinos that subsequently decay into a LH neutrino and a neutral Higgs boson[4]. We assume for most of this paper that the total LH neutrino flux branches into every neutrino flavor equally (see subsection 5.4.1 for a discussion). Assuming that the mass difference between the RH sneutrinos and RH neutrinos is small[5], the RH neutrinos are produced non-relativistically, and hence each LH neutrino and Higgs receives an energy equal to half of the sneutrino mass.

---

[3] Since $B-L$ symmetry is vectorial, the spin-dependent cross section is zero in this model.

[4] RH neutrino decay to a charged lepton and a charged Higgs is typically forbidden.

[5] This is the case when the soft supersymmetry breaking mass of the sneutrino is similar to or smaller than supersymmetry conserving Majorana mass of the (s)neutrino. A rather small soft mass term is motivated if the $B-L$ symmetry is to break radiatively and is needed to keep the lightest $B-L$ Higgs ϕ light as in **case 2** [2].

In **case 2**, RH neutrinos constitute about 10% of the annihilation final states. Two of the lightest $B - L$ Higgses ϕ compose the remaining 90% of the branching fraction. This branching fraction is necessary to provide a high enough leptonic particle rate to fit the PAMELA data. As mentioned in the previous section we need $m_\phi < 20$ GeV. For $4\,\text{GeV} < m_\phi < 20$ GeV, the final states are mostly taus (74%) and b quarks (16%), where the dominance of tau final states is a result of the fermion $B - L$ charges. The LH neutrinos in this case arise from the three-body decay of taus and bottom quarks. For $m_\phi < 4$ GeV, we would have mostly muons and charm quarks.

Both the **case 1** and **case 2** scenarios of our model display a crucial signature difference when compared to the standard neutralino LSP in the MSSM. The energy distribution of the produced LH neutrinos from the RH neutrino decay is a delta function occurring at half of the sneutrino mass. Other annihilation channels in this model, as well as those available in the MSSM, produce additional neutrino signal via three-body decays such as $\tau^- \to e^- \nu_\tau \bar{\nu}_e$. This difference opens up a significant possibility to differentiate between the $B - L$ model and the MSSM with the help of the differential energy spectrum of the detector event rates. This is discussed further in section 5.4.

5.3.2 Neutrino Flux

Sneutrino annihilation in the Sun and the Earth produces an expected neutrino flux through IceCube. This flux is modeled by calculating the number of gravitationally captured sneutrinos and then considering the propagation and detection of the produced neutrinos. The number of captured dark matter particles as a function of time is governed by a differential equation the solution to which is

$$N(t) = \sqrt{\frac{C}{A}} \tanh \sqrt{CA}t \ , \tag{5.2}$$

where C is the total capture rate and depends on both the total scattering cross sections off nucleons and A is related to the annihilation cross section; see Ref. [91] for details. The total rate of annihilation is given by

$$\Gamma_A = \frac{C}{2} \tanh^2 \left(\frac{t}{\tau_{eq}} \right) . \tag{5.3}$$

The number of captured sneutrinos will saturate as long as the length of time for the process has exceeded the equilibration time, $\tau_{eq} \equiv (\sqrt{CA})^{-1}$.

In equilibrated systems, the rate of annihilation is entirely dominated by the capture rate C, $\Gamma_A \approx C/2$. We can explain equilibration in the $B - L$ model by considering some example cross sections. Since the age of the solar system is 4.5 Gyr, for a 1 TeV sneutrino with an annihilation cross section of 3×10^{-23} cm^3/sec (3×10^{-26} cm^3/s), a spin-independent cross section $\sigma_{\rm SI}$ of at least 10^{-11} pb (10^{-8} pb) is needed to reach equilibration in the Sun. This assumes no spin-dependence as the $B - L$ model has none. The scattering cross section needed to achieve equilibration in the Earth is already excluded by direct detection bounds.

Alternatively we can fix the scattering cross section and place a limit on the annihilation cross section. In the $B - L$ model, the cross section for sneutrino-proton elastic scattering follows

$$\sigma_{\rm SI} \propto \left(\frac{g_{B-L} Q_L}{m_{Z'}} \right)^4 m_p^2, \tag{5.4}$$

where g_{B-L} and Q_L are the $U(1)_{B-L}$ gauge coupling and $B - L$ charge of leptons, respectively, and m_p is the proton mass. The limits on the Z' mass from LEP and Tevatron are given by [70, 71],

$$\frac{m_{Z'}}{g_{B-L} Q_L} > 6 \text{ TeV} . \tag{5.5}$$

This results in an upper limit on $\sigma_{\rm SI}$ of 8×10^{-9} pb. Assuming this bound is realized, an annihilation cross section $\geq 4 \times 10^{-26}$cm^3/s (1×10^{-18}cm^3/s) needs to be achieved to reach equilibrium in the Sun (Earth). Note that we can always choose the $B - L$ gauge coupling and scale $B - L$ charges in accordance with anomaly cancelation such that $\sigma_{\rm SI}$ is saturated while obtaining the correct relic density for sneutrino dark matter. This is possible since a different combination of g_{B-L} and Q_{B-L} appears in the relic density calculation . This is in contrast to the MSSM case where the SM gauge couplings and charges are fixed.

Since equilibrium is easily achieved in the Sun, the neutrino signal will depend solely on C, or equivalently $\sigma_{\rm SI}$, so the increased annihilation rate in **case 2** of our model confers no advantage compared to typical MSSM cases for annihilation in the Sun. On the other hand, choosing reasonable values for either of the relevant cross sections demonstrates that equilibrium is nearly impossible to reach for the Earth without significant deviation from the assumptions made in [91]. Consequently, the neutrino signal from the Earth will depend on both C and A. Therefore one expects a much larger signal for **case 2** as compared to either **case 1** or the neutralino dark matter models [92].

The annihilation of sneutrinos in the Sun and Earth yields neutrinos that can be detected by the IceCube experiment. IceCube can distinguish between neutrino signals from the Earth and Sun with the help of an angle cut. This cut restricts the detection to an angle range of $90^\circ < \Theta < 113^\circ$ in the case of the Sun, where Θ is the Earth zenith angle. One has to measure below the horizon to be able to distinguish the background of atmospheric neutrinos from the signal, and the Sun cannot be more than 23.5° below the horizon at the South Pole [93, 94]. In the case of a search for a potential Earth signal one looks at a zenith angle of about 180°, i.e., directly to the core of the Earth [93].

Muon neutrinos create muons via charged current interactions in the detector. The qualitative behavior of the muon flux depends on the corresponding neutrino muon flux, and the differential neutrino spectrum is given by

$$\frac{dN_\nu}{dE_\nu} = \frac{\Gamma_a}{4\pi D^2} \sum_f B^f_{\tilde{N}} \frac{dN^f_\nu}{dE_\nu} \ , \tag{5.6}$$

see for example Ref. [73]. Appendix 5.8 contains a detailed discussion about the mass dependence of this equation.

The IceCube detector records the Cerenkov light from relativistic charged particles in its volume. Cosmic ray showers create a muon background signal that can be controlled by selecting for upward-going and contained muon events. The atmospheric neutrino background is well understood and may be subtracted away from the signal.

In addition to the muon flux through IceCube, electromagnetic and hadronic cascades inside the detector might also allow sneutrino dark matter detection. Electromagnetic cascades occur via charged current interactions. By depositing some of the incoming neutrino energy in taus and electrons, Bremsstrahlung radiation produces a localized cascade of energy that the digital optical modules of IceCube can record. In the results of Appendix 5.9 we have ignored any contribution from the charged current electromagnetic cascades of the muons, since their contribution has already been considered in the form of Cerenkov radiation from the muon tracks. Hadronic cascades occur for both neutral current and charged current interactions. As the neutrino scatters off of a nucleus in the detector, the nucleus breaks up and produces products such as pions that in turn decay into detectable photons. Note that for neutral current interactions the energy of the outgoing neutrino is lost and is not recorded in any cascade. The energy from localized electromagnetic and hadronic cascades is much harder to reconstruct compared to muon tracks but still might produce an interesting signal in the detector, see Appendix 5.9.

5.4 Model Results

The annihilation of sneutrinos in the Sun and Earth results in a flux of particle events through the IceCube detector that are calculated using DarkSUSY, which uses results from WimpSim [73, 95]. The calculations account for neutrinos produced via decays, as well as neutrino oscillation, loss via charged current interactions and scattering via neutral current interactions. DarkSUSY default parameters are used, which include a Gaussian dark matter velocity distribution and an NFW halo profile. Realistic Sun and Earth density profiles are integrated over numerically according to [96]. For both **case 1** and **case 2**, the maximum spin-independent cross section allowed by the Z' limits is used. Similarly, the annihilation cross section is fixed at $3 \times 10^{-26}\text{cm}^3/\text{s}$ ($3 \times 10^{-23}\text{cm}^3/\text{s}$) for **case 1** (**case 2**). Finally, the results presented in the subsections below use the convention of a detector energy threshold of 1 GeV. IceCube effective areas have not been calculated for our model, but we anticipate that they would be slightly larger than those used for the MSSM scenarios since we have a slightly harder spectrum. This is especially true in **case 1**.

5.4.1 Sensitivity to Neutrino Flavor

For the results that follow we have considered equal branching to the three flavors of LH neutrinos, but in principle this need not be the case. The exact flavor composition of LH neutrinos produced from sneutrino annihilation in the Sun depends on the detailed structure of Majorana and Dirac couplings in the neutrino sector. In Fig. 5.1, the resulting muon neutrino flux for a 100% branching ratio to a single flavor is compared to equal flavor ratios in both **case 1** and **case 2** (upper and lower panels respectively).

It is seen from the upper panel that in **case 1** for sneutrino masses below 300 GeV (LH neutrino energy below 150 GeV) flavor composition of produced neutrinos

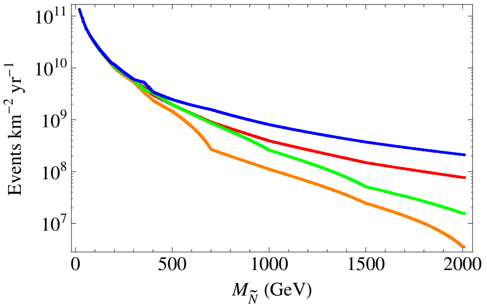

(a) Sun Muon Neutrino Flux, **Case 1**

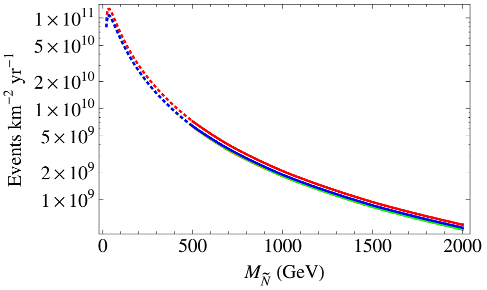

(b) Sun Muon Neutrino Flux, **Case 2**

Figure 5.1: Total muon neutrino rates received at the Earth for the $U(1)_{B-L}$ model as a function of the sneutrino mass in the case of sneutrino dark matter capture and annihilation in the Sun. The results are for one year of detection with IceCube. The $B-L$ model is robust to changes in the neutrino branching ratios. 100% branching to ν_e, ν_μ and ν_τ is shown in orange (bottom line in **case 1**), green (second line from the bottom in **case 1**) and blue (top line in **case 1**) respectively. Results of equal branching to neutrino flavors are in red (second line from the top in **case 1**).

does not matter since oscillations are very efficient at low energies and easily mix the neutrino flavors. Therefore 100% ν_e, ν_μ, or ν_τ each leads to the same ν_μ signal at the detector. However at high energies oscillation length $L_{\rm osc} \propto E_\nu/\Delta m^2$ elongates, and oscillations become less efficient. Here Δm^2 is the difference between (mass)^2 of neutrino mass eigenstates. This effect is most important for ν_e's since they oscillate to ν_μ's via the small mass splitting responsible for solar neutrino oscillations $\Delta m^2_{\rm sol}$. This is why the ν_μ flux at the detector falls quickly for 100% ν_e branching ratio at high energies. The effect is less pronounced for 100% ν_μ and ν_τ branching ratios because the relevant mass splitting is the one responsible for atmospheric neutrino oscillations $\Delta m^2_{\rm atm}$, which is much larger. However, it is seen that the ν_μ flux for 100% ν_μ branching ratio is less than that for 100% ν_τ branching ratio at high energies. This is because of charged current interactions inside the Sun whose cross section is proportional to the neutrino energy. These interactions convert muon neutrinos to muons that are quickly stopped in the Sun due to electromagnetic interactions that result in attenuation of the neutrino flux. Charged current interactions also convert tau neutrinos to taus. However, due to their much shorter lifetime, they decay back to ν_τ before any significant energy loss. Nevertheless, for sneutrino masses up to 1.5 TeV, the result for equal branching ratios to three flavors is within a factor of a few compared with the 100% branching ratio to a single neutrino flavor. Moreover, for a typical model, it is unlikely that sneutrino annihilation produces only one flavor of RH neutrinos. Therefore equal branching to the three flavors is a good approximation in **case 1**.

In **case 2**, the lower panel[6], there is virtually no difference between various flavor compositions. This is because sneutrino annihilation mainly produces taus in this case (the branching ratio for production of RH neutrinos is only 10%). Hence equal branching to the three flavors is a nearly perfect approximation in this case.

We conclude that our results do not depend critically on the choice of neutrino flavor branching ratios in either case.

---

[6] The effect of the 1 GeV conventional energy threshold in the spectrum can be seen at low masses as more of the neutrino signal is lost under the threshold; this causes the maximum event rate to move to the right from the edge of the graph. This effect is not evident in **case 1** since the majority of the neutrino flux arrives at higher energies and is unaffected by the small threshold.

5.4.2 Contributions to Muon Flux

It is worth emphasizing that **case 1** and **case 2** yield different neutrino signals. In **case 1**, LH neutrinos are produced from two-body decay of (almost non-relativistic) RH neutrinos. This produces a delta function in the energy of the LH neutrinos at one-half the mass of the sneutrino dark matter[7]. On the other hand, in **case 2**, the sneutrino dominantly annihilates to $\phi\phi$ final states, and each ϕ decays to a fermion-antifermion pair via a one-loop diagram. The partial decay rate of ϕ is proportional to the squares of the mass of the resulting fermion and the fourth power of its $B-L$ charge [1, 2]. As a result, the largest contribution to the annihilation is from taus ($\approx 74\%$) and bottom quarks ($\approx 16\%$), where the quark signal is suppressed due to the $B-L$ charge. Both of these final states produce neutrinos via three-body decay that results in a spread in energy signal.

Fig. 5.2a shows the muon neutrino flux energy spectrum through a kilometer squared of IceCube in one year for a 300 GeV sneutrino for **case 1**. The delta function at half the mass of the sneutrino can be seen clearly. A small portion of muon neutrinos from this initial annihilation state are scattered via neutral current interactions inside the Sun to lower energies. This produces the slight bump in the spectrum at low energies. Fig. 5.2b plots the resulting muon flux from the charged current interactions inside the IceCube detector. As expected for a monochromatic incident neutrino, the spectrum of muons has a linear dependence on energy.

For **case 2**, the delta function from the neutrino channel at the detector is subdominant to the other annihilation channels, see Fig. 5.3a. First, consider that the sneutrino annihilation mainly produces taus and bottom quarks that subsequently

---

[7] There is one additional potential source for neutrinos: the Higgs produced from the decay of the RH neutrinos can itself decay to a $b\bar{b}$ pair. We checked that this contribution gives only a few percent change in the signal. We therefore neglect it in our numerical calculation for the sake of simplicity.

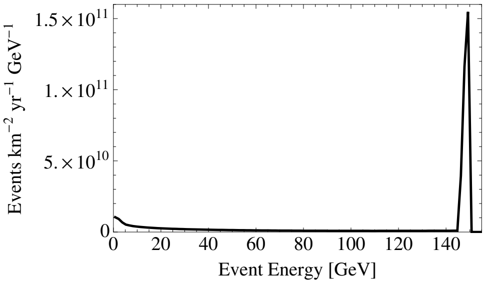

(a) Sun Muon Neutrino Flux

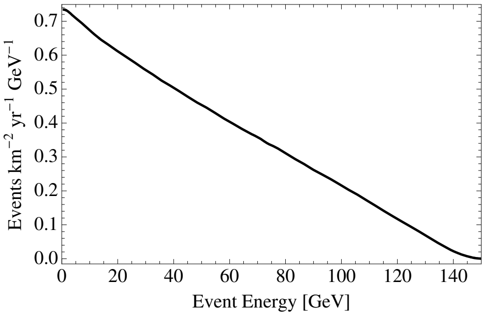

(b) Sun Muon Flux

Figure 5.2: In the upper (lower) panel, muon neutrino (muon) flux through IceCube from annihilation of 300 GeV sneutrinos in the Sun for **case 1**.

produce LH neutrinos via three-body decays. Second, due to the larger sneutrino mass of 1 TeV (in order to explain the PAMELA data), the LH neutrinos produced from two-body decays have a higher energy than in the 300 GeV case. Therefore they lose energy via neutral current interactions and get absorbed via charged current interactions inside the Sun more efficiently. As a result of both of these facts, there are more neutrinos with low energies at the detector from each channel in this case than in **case 1**. This also is reflected in the spectrum of muon flux, shown in Fig. 5.3b, which does not show a linear dependence on energy due to the presence of three-body decays. This is in contrast to Fig. 5.2b.

The muon event signal from annihilation in the Earth for **case 1** and **case 2** is too small to detect since the dark matter population has not reached equilibrium; therefore, the production of neutrinos depends on both the scattering cross section

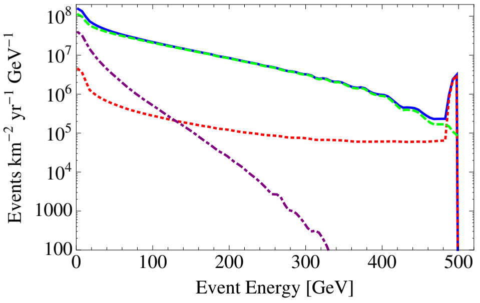

(a) Sun Muon Neutrino Flux

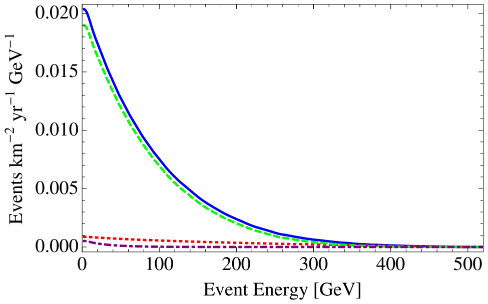

(b) Sun Muon Flux

Figure 5.3: The same as Fig. 5.2, but with a 1 TeV sneutrino in **case 2**. Individual annihilation channels are shown: neutrino (red, dotted), tau (green, dashed), bottom quark (purple, dot-dashed) and all channels (blue, solid).

and the annihilation cross section, which is small in this scenario.

5.4.3 Mass Dependence of Muon Flux

Fig. 5.4 shows our results for the total muon rate integrated over energy as a function of the sneutrino mass $m_{\widetilde{N}}$ for annihilation in the Sun[8]. The figure shows both the **case 1** and **case 2** rates in events km^{-2} yr^{-1}. The plots have two characteristics: an increase at lower masses culminating in a peak followed by a general decrease in event rates at higher masses.

---

[8] The apparent discrete nature of these plots occurs because only a few values of sneutrino mass are recorded in the WimpSim tables used by DarkSUSY; the program interpolates between these points. The effect is numerical and not physical.

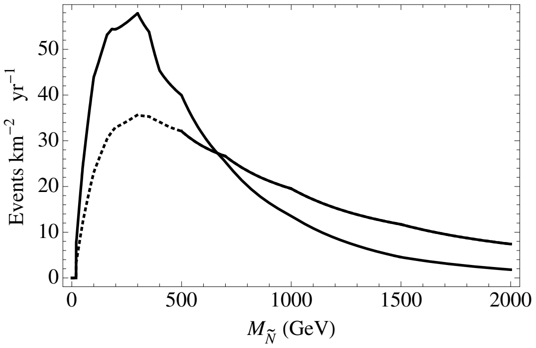

Figure 5.4: Total muon rates detected at the Earth from annihilation of sneutrino dark matter in the Sun as a function of the sneutrino mass. The results are for one year of detection with IceCube. **Case 1** (**case 2**) is the highest (lowest) peaked line. The dotted line denotes the mass range where one cannot explain the PAMELA data using **case 2** anymore.

The decrease of the event rates for higher $m_{\widetilde{N}}$ is reflective of the decrease of the neutrino flux due to the kinematic suppression of sneutrino capture (the factor scales approximately like $1/m_{\widetilde{N}}$ for large masses[9]). The linear increase at low $m_{\widetilde{N}}$ is explained by the linear dependence of the cross section for charged current interactions on the energy of neutrinos at the detector (which is proportional to the sneutrino mass). The **case 1** signal is larger than the **case 2** signal for lower values of sneutrino mass. LH neutrinos are produced in two-body decays in **case 1** versus three-body decays in **case 2**, and hence have a higher energy. As a result, the cross section for conversion of neutrinos to muons at the detector is larger in **case 1**. However, for large sneutrino masses **case 1** has a smaller signal than **case 2**. The produced LH neutrinos, 100% of **case 1** products, get absorbed via charged current interactions or lose energy via neutral current interactions inside the Sun more efficiently because of their larger energy, thus a smaller number of neutrinos arrive at the detector.

---

[9] See Appendix 5.8 for a more detailed definition of "large".

Refs. [97, 98] display sensitivity plots for the detection of a muon signal in the case of standard neutralino dark matter annihilation in the Sun and Earth respectively. In the case of the Earth, more than 12 events are needed for a DM mass between 70 GeV and 4 TeV. In the case of the Sun the number of events needed drops linearly as a function of mass starting from 300 events at 70 GeV down to 70 events at 300 GeV. Beyond 300 GeV up to 4 TeV, the number of events needed remains fixed at 70. This provides a hint that one could detect the event rates caused by sneutrinos despite some differences between the sneutrino and neutralino dark matter spectra. These differences are due to unequal numbers and weighting of neutrino production channels, but the somewhat harder spectrum of the sneutrino model will make IceCube slightly more sensitive to the model. Hence, we can expect that it might be possible to detect muon neutrinos produced by sneutrino annihilation for sneutrino masses around 300 GeV for the Sun, cf. Fig. 5.4. Note that a large range of masses would be accessible with only an order of magnitude improvement in sensitivity.

In summary, if the dark matter mass is determined from measurements at the LHC, then we can read the maximum number expected for the Sun muon rate in the $B-L$ model from Fig. 5.4[10]. Thus, for a known sneutrino mass, observation of a muon signal exceeding the number given in Fig. 5.4 will rule out the $B-L$ model. The largest number of muon events from the Sun in the entire depicted mass range is 58 $\text{km}^{-2}\ \text{yr}^{-1}$ (36 $\text{km}^{-2}\ \text{yr}^{-1}$) for **case 1** (**case 2**). Therefore detection of a muon signal larger than this will rule out the $B-L$ model regardless of the sneutrino mass.

In the case of the Earth, as mentioned in the previous subsection, there is no prospect for a potential detection at IceCube for the standard halo model. The number of muon events is 6 orders of magnitude below the minimum measurable Earth rate of 12 $\text{km}^{-2}\ \text{yr}^{-1}$ in this case.

---

[10] Since we have used the upper bound on the sneutrino-proton scattering cross section in our calculations, the number of muon events cannot be larger than that given in Fig. 5.4.

5.5 Dark Matter Disc in the Milky Way

In our analysis, so far we have assumed a Gaussian like velocity distribution for dark matter particles with a typical value for the three dimensional velocity dispersion of $\sigma_v = 270$ km sec^{-1} and $|v_{Sun}| = 220$ km sec^{-1} for the velocity of the solar system with respect to the halo. However, there are recent speculations about the existence of a dark matter thick disc in the Milky Way in addition to the baryonic one, see e. g. [99, 100]. This dark matter disc is caused by the accretion of Milky Way satellite galaxies and their corresponding baryonic and dark matter. As dynamical friction causes the satellite galaxies to accrete onto the disc, tidal forces disrupt the satellites [100]. Galaxy formation simulations find the density of the dark matter disc ρ_{dark} to be in the range $\approx 0.25 - 1.5$ times the local halo dark matter density ρ_{halo} [100].Possible ranges for the solar system velocity and velocity dispersion of the dark matter disc are$|v_{Sun}| \approx 0 - 150$ km sec^{-1} and $\sigma_v \approx 87 - 156$ km sec^{-1}.

Fig. 5.5 shows the Earth muon rate when we scan about the relevant parameter space for the allowed values of $|v_{Sun}|$ and σ_v in **case 1** and **case 2**. We used the fixed ratio $\rho_{\text{dark}}/\rho_{\text{halo}} = 1$. **Case 2** has a sufficient total event rate (≥ 12 km^{-2} yr^{-1}) for nearly the whole allowed parameter space. The constraint of the parameter space is more pronounced for **case 1**. The allowed combinations are roughly given by a triangle with maximal values of $|v_{Sun}| = 47$km/s and $\sigma_v = 100$km/s. The differences in the allowed parameter space for the two cases reflects the fact that the Earth is not in equilibrium yet. Thus the muon neutrino signal and the corresponding muon flux still depends on the annihilation cross section, which is three orders of magnitude larger for **case 2**. However, we see that in both cases the Earth rates have increased to detectable rates, several orders of magnitude higher than the standard halo model that has higher $|v_{Sun}|$ and σ_v, used in the previous section[11].

---

[11] The usage of a free space Gaussian velocity distribution means that our calculated event rates are an upper bound. There are many proposed parameterizations for the dark

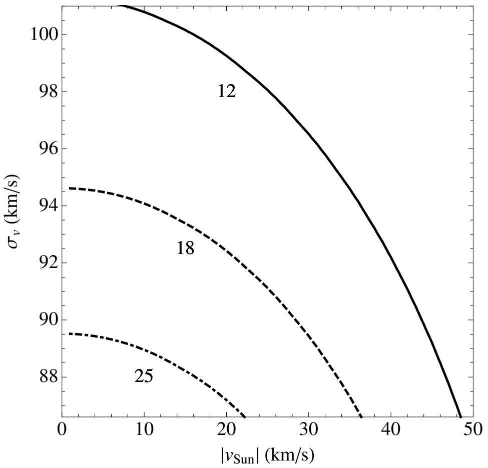

(a) Earth muons, **Case 1**

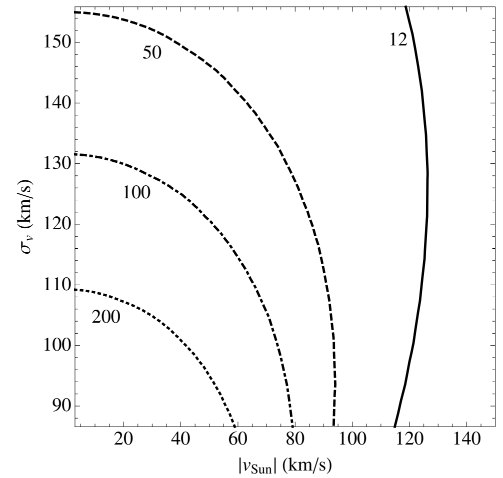

(b) Earth muons, **Case 2**

Figure 5.5: Total Earth-annihilation muon event rates inside the detector per kilometer squared per year for a 300 GeV (in **case 1**) and 1000 GeV (in **case 2**) sneutrino.

A change in the velocities and dispersions also modifies the corresponding total Sun event rates. This is comparatively modest for neutralino dark matter where it is at most one order of magnitude, see [39]. Fig. 5.6 shows a band of allowed total Sun muon rates for the sneutrino dark matter. These rates are given again as a function of the sneutrino mass and under the requirement that we have a measurable Earth

---

matter velocity distribution, and a Gaussian distribution belongs to the scenarios with the highest resulting event rates, see [39].

rate of at least 12 events km^{-2} yr^{-1}. Any variation of the event numbers for a fixed mass arises as a result of the use of velocities $|v_{Sun}|$ and dispersions σ_v within the required parameter ranges of Fig. 5.5a and 5.5b. A comparison between Fig. 5.4 and 5.6 shows an increase of $\approx 30\%$ in the Sun muon rates for the sneutrino dark matter.

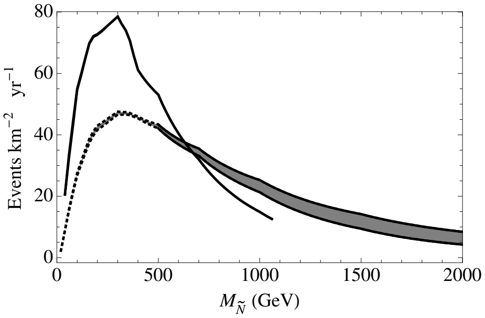

Figure 5.6: Total Sun-annihilation muon rates inside the detector for the sneutrino dark matter with modified velocity distributions that yield Earth-annihilation rates of at least 12 events per year per km^2. Upper (lower) curve shows the **case 1** (**case 2**). The dotted lines denote the mass range where one cannot explain the PAMELA data using **case 2** anymore.

The band of total muon rates for **case 1** is noticeably thinner than for **case 2**. It is seen from Figs. 5.5a and 5.5b that **case 1** has a smaller allowed parameter range with more than 12 events km^{-2} yr^{-1}. Thus the corresponding ratio between the minimal and maximal value within the allowed range is much smaller than that in **case 2**, and the possible change in the total Sun rates is comparatively small. Even for **case 2** the differences between the highest and lowest rates for a fixed mass is about 40% or less.

To summarize, a modified velocity distribution can substantially enhance the Earth muon rate for the sneutrino dark matter beyond the detection threshold of 12 km^{-2} yr^{-1}. It also raises the maximum Sun muon rate to 78 events km^{-2} yr^{-1} (48 km^{-2} yr^{-1}) in **case 1** (**case 2**). Observation of the Sun muon rates larger than these will rule out the $B - L$ model regardless of the sneutrino mass or Earth rates.

5.6 Comparison with mSUGRA

Minimal supergravity (mSUGRA) is a constrained version of the MSSM that depends only on four parameters and one sign. These are m_0 (the universal soft breaking mass at the grand unification scale), $m_{1/2}$ (the universal gaugino soft breaking mass at the grand unification scale), A (the universal trilinear soft breaking mass at the grand unification scale), tan β (the ratio of MSSM Higgs VEVs at the electroweak scale) and the sign of μ (the MSSM Higgs mixing parameter). The mSUGRA dark matter candidate is the lightest neutralino.

The parameter space of the mSUGRA model has three distinct regions allowed by the dark matter constraints [101]: (i) the co-annihilation region where both m_0 and $m_{1/2}$ can be small, (ii) the hyperbolic branch/focus point region where the dark matter has a large Higgsino component and m_0 is very large but $m_{1/2}$ is small, and (iii) the funnel region where both m_0 and $m_{1/2}$ are large and the dark matter annihilation occurs through heavy Higgs bosons in the s-channel. We note that a bulk region (where none of the above properties hold) is now almost ruled out due to other experimental constraints. Among these three regions, the neutralino has a large capture rate in the hyperbolic branch/focus point region due to a large Higgsino component that results in a large spin-dependent scattering cross section via Z exchange. In this section we compare mSUGRA hyperbolic branch/focus point scenarios with the $B - L$ model.

Fig. 5.7 shows the total Sun muon rate as a function of the neutralino mass for mSUGRA hyperbolic branch/focus points. A comparison with Fig. 5.4 shows that these scenarios always have a higher total muon rate in the plotted mass range than the $B - L$ model. The hyperbolic branch/focus point models yield larger muon

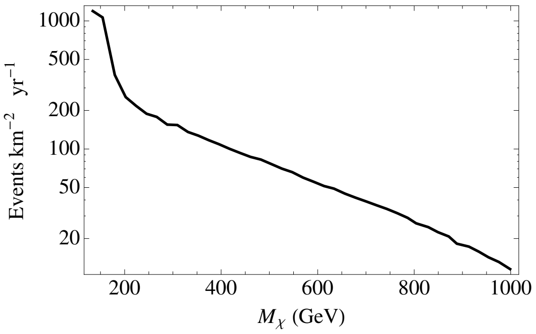

Figure 5.7: Total Sun-annihilation muon rates inside the detector for mSUGRA hyperbolic branch/focus point scenarios as a function of the neutralino mass. The results are for one year of detection with IceCube.

rates by between more than one order of magnitude and a factor of 1.5 for dark matter masses in the $100 - 800$ GeV range. Even for masses up to 400 GeV the hyperbolic branch/focus point scenarios provide rates higher than 100 events km^{-2} yr^{-1}. These higher rates are explained by the bigger spin-dependent scattering cross sections, which are a few orders of magnitude larger than the upper bound on the spin-independent cross section for the sneutrino dark matter. The spin-dependent scattering cross section for the $B - L$ model is zero because $U(1)_{B-L}$ is a vectorial symmetry. Since the Sun mainly consists of hydrogen, the spin-dependent piece contributes dominantly for the mSUGRA case.

However, it is interesting that despite having a much smaller scattering cross section, the $B - L$ model can yield muon rates that are roughly comparable to the mSUGRA scenarios. Sneutrino annihilation dominantly produces leptons, i.e., RH neutrinos in **case 1** and taus in **case 2**, which subsequently decay to LH neutrinos 100%. On the other hand, neutralino annihilation in the hyperbolic branch/focus point scenarios dominantly produces quark final states that have a small branching ratio for decay to neutrinos.

Furthermore, despite lower event rates, sneutrino dark matter still produces a distinctive linear spectrum in the muon flux. As illustrated in subsection 5.4.2, this feature is caused by the delta function in energy for the neutrino spectrum and can be used to distinguish between the $B - L$ model and the hyperbolic branch/focus point scenarios as long as energy binning of the differential muon rate with respect to the energy is precise enough at IceCube.

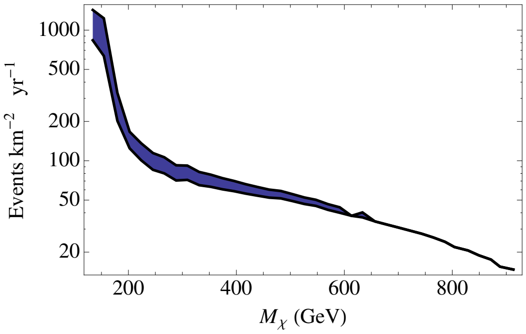

Figure 5.8: Total muon rates detected inside the Earth for mSUGRA Focus point scenarios as a function of the neutralino mass in the case of neutralino DM capture and annihilation in the Sun. Rates for a range of velocities and dispersions for which the corresponding Earth rates are at least 12 events per year per km^2 are shown in the shaded region. The results are for one year of detection with IceCube.

Fig. 5.8 shows the counterpart of Fig. 5.6 for mSUGRA hyperbolic branch/focus point scenarios. The range of velocities and dispersions for which the corresponding Earth rates are at least 12 events km^{-2} yr^{-1} yields a band for the total Sun muon rates. We see that the range between the highest and lowest rates for a fixed mass does not exceed a factor of two even for masses below 200 GeV.

A scan about the whole parameter space of the modified velocity distribution yields a maximum of 13 events km^{-2} yr^{-1} from the Sun for a 1000 GeV neutralino in the hyperbolic branch/focus point sneutrino. The $B - L$ model with sneutrino masses of 1000 GeV and 1500 GeV gives rise to maximum values of 18 and 6 (25 and 14) events km^{-2} yr^{-1} for **case 1** (**case 2**). In contrast, for a dark matter mass of 300 GeV, the maximum events km^{-2} yr^{-1} are 158 (hyperbolic branch/focus point), 79 (**case 1**) and 48 (**case 2**). Thus the hyperbolic branch/focus point rates are larger than the $B-L$ rates for low masses, but both are in the detectable range at IceCube. At high masses it becomes more difficult to distinguish between the hyperbolic branch/focus point and the $B-L$ models using maximal Sun rates; we would have to depend instead on the spectral features mentioned in Section 5.4.2.

In the stau co-annihilation and Higgs resonance regions the lightest neutralino has a high gaugino fraction and therefore a much smaller spin-dependent cross section that leads to much lower event rates than the $B-L$ model. For example, even if we assume a modified velocity distribution without any minimal Earth event rate condition the maximum total Sun rate is less than 1 event km^{-2} yr^{-1} for a 300 GeV neutralino (compared with the maximum Sun rate of 158 events km^{-2} yr^{-1} for a hyperbolic branch/focus point scenario with the same mass). This is far below any detection threshold.

It is also important to note that the hyperbolic branch/focus point in the m-SUGRA model is incompatible with the $g-2$ data, where there exists a 3σ deviation from the SM value if the e^+e^- data is used to calculate the leading order hadronic contribution [102]. In the context of the $B-L$ model, **case 2**, which can address the PAMELA puzzle, also becomes incompatible with $g-2$ data, however the generic $B-L$ model, i.e. **case 1**, is still compatible.

5.7 Conclusion

We have considered prospects of indirect detection of the RH sneutrino dark matter in a $U(1)_{B-L}$ extension of the MSSM at the IceCube neutrino telescope. The sneutrinos captured in the Sun and Earth dominantly annihilate through S-wave processes at the present time. In a generic situation (called **case 1**) the sneutrinos annihilate to RH neutrinos (annihilation cross section of 3×10^{-26} cm^3/sec) that quickly decay to a LH neutrino and the MSSM Higgs. If one seeks an explanation for the recently observed positron excess from the PAMELA data (called **case 2**), the sneutrinos with a mass ≥ 1 TeV dominantly annihilate to the lightest Higgs in the $B-L$ sector (with an enhanced annihilation cross section of 3×10^{-23} cm^3/sec) that rapidly decay to fermion-antifermion pairs (74% taus, 16% bottom quarks, and 10% RH neutrinos). LH neutrinos are produced mainly from the three-body decay of taus. The muon neutrinos from sneutrino annihilation are converted to muons via charged current interactions at IceCube.

In both of the cases, sneutrino capture and annihilation inside the Sun reaches equilibrium. Consequently, the flux of neutrinos from the Sun is governed by the cross section for sneutrino-proton elastic scattering, which has an upper bound of 8×10^{-9} pb from the LEP and Tevatron limits on the Z' mass (due to the vectorial nature of the $B-L$ symmetry, there is no spin-dependent piece). In Fig. 5.4 we have shown the number of Sun muon events at IceCube as a function of the sneutrino mass for **case 1** and **case 2** (using the upper bound on the sneutrino-proton scattering cross section). In both cases, the number of events are potentially detectable by IceCube due to a harder neutrino spectrum. Thus once the dark matter mass is found from measurements at the LHC, observation of muon events larger than that given in Fig. 5.4 will rule out the $B-L$ model.

For the standard halo model the capture and annihilation of sneutrinos inside the Earth does not reach equilibrium for either **case 1** or **case 2**, resulting in an event rate that is too small to be detected at IceCube. However, modified velocity distributions within the range allowed by recent simulations of the galaxy can lead to a substantially larger rate that exceeds the IceCube detection threshold of 12 km^{-2}

yr^{-1} for events from annihilation in the Earth. Nevertheless, the Sun-annihilation muon rate can at most increase by 30% for a modified velocity distribution, as shown in Fig. 5.6. This implies that observation of a muon event rate larger than roughly 100 $\text{km}^{-2}\ \text{yr}^{-1}$ from the Sun will all but rule out the $B-L$ model regardless of the dark matter mass.

We compared predictions of the sneutrino dark matter in the $B-L$ model with that of the neutralino dark matter in the mSUGRA model. Only hyperbolic branch/focus point scenarios in mSUGRA, which have a Higgsino type dark matter candidate and thus large spin-dependent contributions to the neutralino-proton elastic scattering cross section, give rise to Sun muon event rates that can be detected at IceCube. Even though scattering cross sections can be two to three orders of magnitude larger than the $B-L$ case, the muon rates do not scale directly with the cross section. This is because sneutrinos mainly annihilate into lepton final states (by virtue of the $B-L$ symmetry) that decay to neutrinos with 100% efficiency, while neutralino annihilation dominantly produces quark final states that have a small branching ratio for decay to neutrinos. Moreover, the linear dependence of the muon spectrum on the energy in the case of the sneutrino dark matter (particularly **case 1**) , a common feature for neutrinos produced from the two-body decays, can be used to distinguish between the $B-L$ model and the hyperbolic branch/focus point scenarios. This will be feasible by a sufficiently precise energy binning of the differential muon rate at IceCube.

5.8 Chapter Appendix: Mass Dependence of Γ_A

We analyze in detail here the contribution from Eq. (5.3) to the mass behavior of Fig. 5.4. Any mass dependence from dN_ν^f/dE_ν is ultimately washed out of the muon signal by the linear dependence of $\sigma_{CC,NC}$ on the neutrino energy, which dominates at low energy. The distance D between the detector and the source and the branching fraction $B^f_{\widetilde{N}}$ into the final state f are independent of $m_{\widetilde{N}}$. Thus, the annihilation rate at high energies is governed by the dependence of Γ_A on the kinematic suppression factor. Eq. (5.3) shows that this annihilation rate is proportional to the capture rate C. Ref. [91] provides a parameterization of C as a function of the energy:

$$C(m_{\widetilde{N}}) \propto \sum_i F_i(m_{\widetilde{N}}) S(m_{\widetilde{N}}/m_{N_i}) \sigma_i(m_{\widetilde{N}}) \ , \tag{5.7}$$

where the sum runs over all species i of nuclei in the Sun or Earth, F_i are the corresponding form factors, S is the kinematic suppression factor for capture of a sneutrino and the σ_i are the individual scalar cross sections for scattering from nucleus i. The effect of the F_i dependence on mass is negligible because most of these form factors vary little from unity. Furthermore, σ_i is not dependent on the sneutrino mass in the $B-L$ model since we have chosen a constant sneutrino-proton scattering cross section of 8×10^{-9} pb (the upper bound implied by the Z' mass limits). Thus the overall shape of the curves in Fig. 5.4 can be understood by looking at $S(m_{\widetilde{N}})$.

S can be parameterized by

$$S(x) = \left[\frac{A(x)^{1.5}}{1+A(x)^{1.5}}\right]^{3/2} \ , \tag{5.8}$$

$$A(x) = 1.5 \frac{x}{(x-1)^2} \left(\frac{<v_{esc}>^2}{\bar{v}^2}\right) \ , \tag{5.9}$$

where $\bar{v} = 270$ km sec^{-1} is the velocity dispersion of the dark matter particles and $< v_{\rm esc} >$ is the escape velocity of 1156 km sec^{-1} and 13.2 km sec^{-1} for the Sun and Earth respectively. $S(x)$ is bounded between zero and one. Moreover, it scales like $1.5(< v_{\rm esc} >^2 / \bar{v}^2)/x$ for $x \to \infty$, and it peaks at one for $x = 1$. Therefore, the exact location of the peak for each scattering element i is determined by its corresponding nucleus mass m_{N_i}. As mentioned in subsection 5.4.3, S scales approximately like

$1/m_{\widetilde{N}}$ for large masses. The meaning of large in this context depends on the value of the $(< v_{\rm esc} > /\bar{v})^2$ ratio in comparison to x. For example, a value of $m_{\widetilde{N}}$ with $m_{\widetilde{N}}/m_{N_i} > (<v_{\rm esc}> /\bar{v})^2$ is considered large.

5.9 Chapter Appendix: Cascade Signal

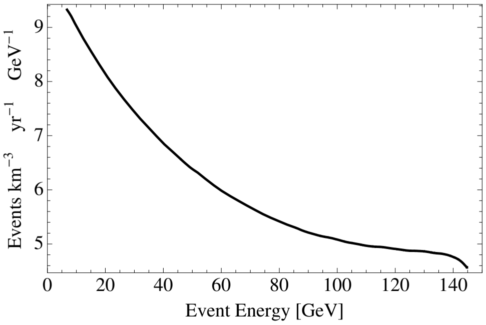

(a) Sun Cascades, **Case 1** 300 GeV sneutrino

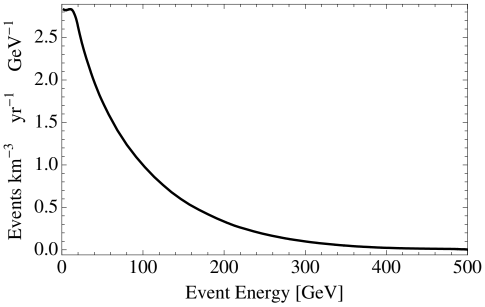

(b) Sun Cascades, **Case 2** 1000 GeV sneutrino

Figure 5.9: Total electromagnetic and hadronic cascades inside the detector volume from sneutrino annihilation in the Sun.

Fig. 5.9 plots the total energy spectrum from all cascades, both hadronic and electromagnetic (excluding the electromagnetic muon signal[12]), per kilometer squared of

---

[12] The electromagnetic cascade from a muon signal is excluded from the graph since it is accompanied by a more discernable muon track, the subject of the body of this paper.

detector per year for **case 1** and **case 2**. The general downward trend of the plot occurs because the hadronic signal dominates as it is produced by both charged current and neutral current interactions, while the upward-trending electromagnetic signal only receives contributions from the charged current interactions and excludes the muon signal altogether. The cross sections for hadronic processes decrease as the transferred energy to the nucleus goes up, hence creating the decreasing trend (high energy in the hadronic cascades corresponds to low energies in the electromagnetic cascades). We note that in the lower panel of the figure (**case 2**) the cascade signal is depleted at high energies. This is because the produced neutrinos have higher energies (as a result of the higher sneutrino mass in this case), and therefore absorption and scattering effects inside the Sun are more important. This explains why the signal in **case 2** is more steeply curved than the **case 1** signal.

It is important to remember that it is not clear at this time whether IceCube will be able to distinguish between electromagnetic and hadronic cascades. As a result, while a single charged current interaction will result in both a hadronic and electromagnetic cascade, these may be recorded as a single event with the total energy of the incoming neutrino. Meanwhile, the hadronic cascade of neutral current events would be recorded correctly as a single event with only part of the energy of the incoming neutrino. While we have assumed in the above that individual cascade signals are separable this may not reflect experimental reality.

5.10 Acknowledgement

The authors wish to thank Spencer Klein and Carsten Rott for valuable discussions. The work of BD is supported in part by DOE grant DE-FG02-95ER40917.

Chapter 6

Distinguishing among dark matter annihilation channels with neutrino telescopes

Major Results

Diverting from the previous work, this chapter takes a model-independent approach and seeks to discriminate between different DM final states, which may be generated by any model. The work of this chapter was completed in collaboration with Dr. Rouzbeh Allahverdi and was accepted for publication in Physical Review D [4]. Since muons in the ice travel approximately 5 GeV for every meter, track length may be used to reconstruct energy as long as $E_\mu < 1$ TeV. The energy reconstruction thus has a Gaussian error in energy approximately equal to a spread of 40 GeV with one sigma likelihood. However, even when these reconstruction errors are taken into account, IceCube/DeepCore is capable of detecting monochromatic neutrinos in the presence of less energetic Ws or τs after ten years of data.

Furthermore, neutrino flavors may also be distinguished using the signal from tau neutrino regeneration, wherein tau neutrinos experience charged-current interactions, produce a tau, which in turn decays quickly to a low energy tau neutrino. Neither electron nor muon neutrinos experience regeneration since μs and electrons are quickly stopped due to electromagnetic interactions. The oscilltion length is propotional to energy, but the absorption length of charged current interaction is inversely propotional to energy. Thus, as energies increase starting at about 500 GeV, the absorption length becomes shorter than the oscillation length. Muon neutrinos are absorbed in charged current interactions before they have the opportunity to oscillate to tau neutrinos and experience regeneration. The distinguishing signal of regenerated τs may shed light on the nature of the lepton-numbered DM annihilating to neutrinos.

Abstract

We investigate the prospects for distinguishing dark matter annihilation channels using the neutrino flux from gravitationally captured dark matter particles annihilating inside the sun. We show that, even with experimental error in energy reconstruction taken into account, the spectrum of contained muon tracks may be used to discriminate neutrino final states from the gauge boson/charged lepton final states and to determine their corresponding branching ratios. We also discuss the effect of ν_τ regeneration inside the sun as a novel method to distinguish the flavor of final state neutrinos. This effect as evidenced in the muon spectrum becomes important for dark matter masses above 300 GeV. Distinguishing primary neutrinos and their flavor may be achieved using multi-year data from a detector with the same capability and effective volume as the IceCube/DeepCore array.

6.1 Introduction

Many lines of evidence support the existence of dark matter (DM) in the universe, but its identity remains a major problem at the interface of particle physics and cosmology. The weakly interacting massive particles (WIMPs) are promising DM candidates [79]. They can explain the DM relic abundance, as precisely measured by cosmic microwave background (CMB) experiments [5], via thermal freeze-out of annihilation in the early universe. Major experimental efforts seek to detect DM particles via direct, indirect and collider searches. These experiments provide complementary information on the properties of DM such as its mass, elastic scattering cross section with nucleons, annihilation cross section, and annihilation channels.

Indirect searches investigate annihilation of DM to various final states (neutrinos, photons, charged particles) through astrophysical observations. Neutrinos provide an especially interesting probe because they are least affected on their way from the production point to the detection point. As a result, neutrino telescopes like IceCube (IC) can trace a neutrino signal directly back to the source. DM particles gravitationally captured inside the sun annihilate and produce such a signal. When equilibrium between DM capture by the sun and DM annihilation inside the sun is established, the flux of produced neutrinos depends on the DM mass, scattering cross section off nucleons and the annihilation spectrum. The DM mass and scattering cross section can be independently determined from other experiments. In particular, the Large Hadron Collider (LHC) is on the verge of discovering new physics, which will enable us to measure the mass of the DM particle. Therefore, using the LHC measurements and the IC results in tandem, we hope to identify the annihilation channels and their corresponding branching ratios.

In this paper, we study the prospects for determining DM annihilation final states with IC. This model-independent study has two goals: 1) distinguishing scenarios in which DM annihilates into neutrinos from scenarios where DM annihilates into gauge bosons and charged leptons, and 2) extracting information about flavor composition of neutrino final states in the former case.

Gauge boson and charged fermion final states are the dominant annihilation channels for the popular and extensively studied neutralino DM in the minimal supersymmetric standard model (MSSM). On the other hand, annihilation to neutrinos can arise as the dominant channel in extensions of the standard model (SM) in which DM is related to the neutrino sector. Discriminating neutrino final states from gauge boson and tau final states will therefore allow us to discern between the two large classes of DM models. In the case that DM mainly annihilates into neutrinos, it will be important to also know the flavor composition of the final state neutrinos. This will shed further light on the specific aspects of the model that connect DM to neutrinos.

We show that the contained muon tracks at neutrino telescopes like IC may be used for both purposes. The spectrum of contained muons can be used to determine the branching ratios of neutrino final states versus gauge boson and tau final states. We demonstrate this for several points in the parameter space within the reach of the one-year sensitivity limits of the IceCube/DeepCore (IC/DC) array, with the background from atmospheric neutrinos and the experimental error in energy reconstruction of the muons taken into account. In addition, the ν_τ regeneration due to charged current interactions inside the sun may be used to extract information about the flavor of final state neutrinos for DM masses above 300 GeV. In particular, we see that the ν_τ final state can be discriminated from the ν_μ and ν_e final states at a significant level for DM masses as heavy as 800 GeV. Distinguishing the neutrino final states and discriminating the flavor of neutrinos may be achieved with multi-year data from IC/DC.

This paper is organized as follows. The DM signal in neutrino telescopes is explained in section II. In section III, we discuss the motivation for models where DM annihilates mainly into neutrinos. Section IV includes the analysis distinguishing the neutrino final state from the gauge boson and tau final states. We investigate discriminating the neutrino flavor in the former case in section V. Finally, we conclude the paper in Section VI.

6.2 Neutrino Telescopes as Dark Matter Detectors

6.2.1 The Sun as a Source of Dark Matter Neutrinos

DM annihilation in the sun produces a neutrino flux that can be probed by neutrino telescopes like IC. This neutrino flux is modeled by calculating the number of gravitationally captured DM particles in the sun and then considering the propagation and detection of the neutrinos produced in DM annihilation. The number of captured DM particles as a function of time is governed by a differential equation that balances the capture of particles from elastic scattering on nucleons with the annihilation rate; see [91] for details. The total rate of annihilation in the sun is given by [103]

$$\Gamma_A = \frac{C}{2} \tanh^2 \left(\frac{t}{\tau_{eq}} \right) , \tag{6.1}$$

where C is the capture rate of DM particles. The number of particles captured will saturate at $\Gamma_A \approx C/2$ as long as the length of time for the process has exceeded the equilibration time, $\tau_{eq} \equiv (\sqrt{CA})^{-1}$.

With a nominal freeze-out annihilation rate of 3×10^{-26} cm^3/s, DM readily achieves equilibrium within the lifetime of the solar system, 4.5 Gyr, for spin-independent elastic scattering cross sections compatible with the limits set by the XENON100 experiment: $\sigma_{\rm SI} = {\rm few} \times (10^{-9} - 10^{-8})$ pb for the mass range 100 GeV$-$1 TeV [104]. The spin-dependent cross section needed to reach equilibrium is larger by a factor of about 300 [91], which is well below the current experimental limit of $\sigma_{\rm SD} \leq 2.5 \times (10^{-4} - 10^{-3})$ pb for the 100 GeV $-$ 1 TeV mass range [29].

The difference between the equilibrium constraints on $\sigma_{\rm SI}$ and $\sigma_{\rm SD}$ comes from the fact that $\sigma_{\rm SI} \propto M^4$ while $\sigma_{SD} \propto J(J+1)$; M and J are the mass and spin of target nuclei inside the sun respectively. Heavy elements such as iron account for only a thousandth of the sun's mass and suffer a two order of magnitude form-factor suppression in capturing WIMP-scale DM masses [91]. On the other hand, hydrogen dominates the sun's composition and does not suffer a form factor suppression. Thus, the ratio of the spin-independent contribution from iron to the spin-dependent contribution from hydrogen is on the order of $(56)^4/10^5 \sim \mathcal{O}(100)$. Since equilibrium is easily achieved in the sun, the neutrino signal will depend solely on C, or equivalently $\sigma_{\rm SI}$ and/or $\sigma_{\rm SD}$.[1]

Once neutrinos are produced from DM annihilation in the sun, their spectra undergo a number of changes before detection. Scattering via neutral current interactions results in neutrino energy loss, while charged current interactions result in absorption of neutrinos. These effects are proportional to the energy of the neutrino and will therefore have the greatest effect on the high energy part of the spectrum. Neutrinos are also affected by oscillations on the way to the earth. Since the oscillation length is proportional to energy, $L_{\rm osc} \propto E_\nu$, the effect is more important for the low energy part of the spectrum.

6.2.2 Neutrino Background, Energy Reconstruction and Thresholds

Neutrino telescopes access the neutrino signal from DM annihilation by recording Cerenkov light from relativistic charged particles in their volume. Muon neutrinos produce muons via charged current interactions in the detector. Cosmic ray showers create a muon background that can be controlled by selecting for upward-going events since muons are stopped in the earth. This limits observation of a DM signal from the sun to half the year, when the sun is below the horizon. However, a

---

[1] The neutrino signal from DM annihilation in the earth is negligible assuming a standard DM velocity distribution in the halo.

portion of the detector may be used as a veto to observe contained muon events with a conversion vertex of ν_μ to μ inside the instrumented volume. The veto procedure virtually eliminates the contribution to the background from through-going atmospheric muons by selecting for contained vertices. This increases the potential observation time to the full year when the sun is both above and below the horizon. With through-going muons eliminated as a background, the most significant contribution to the remaining background comes from atmospheric neutrinos. The spectrum of the atmospheric neutrino background from cosmic rays is understood theoretically to within 20% [105] and is measured above 100 GeV to within 10% [106], but individual atmospheric neutrino events cannot be distinguished from neutrinos from DM annihilation.

The DM neutrino signal can be further enhanced over the background by allowing for an angular cut in the direction of the sun. The cut will be made on the muon track, and not the incoming neutrino. A smaller angle between the track and incident neutrino occurs for muons with an energy closer to that of the neutrino.[2] That is, the muon events that deflect little from the incoming neutrino path are the highest energy events. While the smallest possible angular cut is desirable to eliminate background, more accommodating cuts on the angle between the track and the sun provide information about lower energy events.

Energy reconstruction of events can be approximated in two regimes. Above 1 TeV, the light generated by an event is proportional to the muon energy since Bremsstrahlung radiation, nuclear interactions and pair production create charged particles each of which contribute to the Cerenkov radiation. Energy reconstruction in this regime will be logarithmic in energy with an error of $\log_{10}\sigma_E \sim 0.3$ [107]. Meanwhile, below ~ 300 GeV the length of the track is proportional to the energy of the incident particle since the majority of energy loss in this range is governed

---

[2] For an elastic collision, the dependence of the angle $\theta_{\nu\mu}$ on the muon energy E_μ angle is approximately given by $\theta_{\nu\mu} \lesssim 5.7^\circ\ (100\ \mathrm{GeV}/E_\mu)^{1/2}$.

by ionization. In this case reconstruction will likely be more accurate for contained tracks, and reconstruction algorithms are currently in development [108]. Events between these regimes call for a more complicated reconstruction algorithm.

Whereas the IC design is focused on event energies above a TeV, IC/DC achieves an energy threshold as low as 10 GeV. IC/DC consists of eight more densely instrumented strings with high quantum-efficiency digital optical modules (DOMs). Surrounding IC strings veto through-going muons so IC/DC records muon-neutrino vertex events inside its volume. IC/DC increases the IC effective volume at energies below 65 GeV and accounts for the majority of events recorded below 100 GeV. Further infills of the IC array, such as PINGU, could extend the energy threshold to a few GeV and further increase the effective volume by a factor of two at 10 GeV [109].

6.3 Primary Neutrinos from Dark Matter Annihilation: Theoretical Motivation

DM particles can in principle annihilate into any of the SM particles. The annihilation rate to a final state is given by $\sigma_{\rm ann} v = a + bv^2$, where v is the relative velocity of annihilating particles. The two terms in this expression represent the S-wave and P-wave contributions respectively. For DM annihilation inside the sun the thermalized velocity is very low ($v \sim 10^{-4}$ for a 100 GeV DM particle). Therefore channels that proceed through the S-wave dominate annihilation (unless a is extremely small).

For the popular and extensively studied neutralino DM in the MSSM, annihilation is mainly into gauge boson and charged fermion final states. For example, in the stau-neutralino coannihilation region of minimal supergravity (mSUGRA) models [110], where DM is mostly Bino, annihilation in the S-wave of DM particles is typically dominated by the tau final states. Taus produce relatively soft neutrinos via three-body decay. In the focus point region of mSUGRA models [111], where DM particles have a large Higgsino fraction, S-wave annihilation is predominantly into W bosons (and t-quarks if kinematically allowed). W's produce neutrinos with a harder spectrum via two-body decay. As a result, annihilation of neutralino DM typically yields secondary neutrinos from W and tau final states. The neutrino signal that is produced inside the sun in this way has been studied in various cases [112]. Because of the existence of charged particles in the final state, annihilation of neutralino DM also results in a gamma-ray signal. This implies that one can also obtain constraints by using data from the Fermi gamma-ray space telescope [31].

Neutralino annihilation to primary neutrinos happens via gauge interactions where neutrinos are produced through the $Z\nu\bar{\nu}$ vertex. It therefore produces a left-handed (LH) neutrino and a right-handed (RH) antineutrino. Considering that the neutralino is a Majorana fermion, the S-wave contribution to such a final state is extremely small due to the tiny masses of neutrinos. We note that the P-wave contribution to neutrino final states is also very small because of velocity suppression. In consequence, production of primary neutrinos with a hard spectrum from neutralino annihilation is highly suppressed.

However, it is possible to enhance DM annihilation into primary neutrinos by going beyond neutralino DM. If DM annihilation produces a $\nu\nu$ pair, instead of a $\nu\bar{\nu}$ pair, it can proceed in the S-wave without any mass suppression. A detailed analysis of settings in which DM annihilation into neutrinos is enhanced has been given in [113]. This can happen when DM is related to the neutrino sector (for some specific models, see [114]).

One particular model that can produce hard monochromatic neutrinos is the $B-L$ extension of the MSSM (B and L are baryon and lepton number respectively). A minimal extension of the SM gauge group, motivated by the nonzero neutrino masses, includes a gauged $U(1)_{B-L}$ gauge symmetry [66]. Anomaly cancellation then implies the existence of three RH neutrinos (N), the lightest superpartner of which ($\widetilde{N}$) makes a viable DM candidate [2]. Thermal freeze-out of the sneutrinos can yield the correct dark matter abundance if the $B-L$ symmetry is broken around the TeV scale [68]. The sneutrinos can annihilate in the S-wave to RH neutrinos, which in turn decay to LH neutrinos and the SM Higgs. The energy of the resulting neutrinos will be close to monochromatic as long as the difference between the masses of the RH sneutrino and RH neutrino is much less than the RH sneutrino mass. The prospects for DM detection for this model using IC is considered in [3].[3]

The neutrino signal is the main channel of indirect searches for models with DM annihilation to primary neutrinos. These models result in a highly suppressed gamma-ray signal, which escapes the bounds set by Fermi [31]. It is worth pointing out that neutrinos from DM annihilation in the galactic center provide complementary information to those from annihilation inside the sun: the former constrains the DM annihilation cross section [115], while the latter bounds the DM scattering cross section off nucleons [29]. The signature of DM annihilation to neutrinos at the galactic center should be distinctive with a hard cutoff (for example, see [117]).

---

[3] This model has other interesting cosmological and phenomenological implications. The Tevatron [70] and LEP [71] limits on the Z' mass bound the RH sneutrino-nucleon scattering cross section to be $\sigma < 7 \times 10^{-9}$ pb, which is just below the bound from the XENON experiment [104]. Significant DM annihilation to taus is also possible [2] (also see [1]), which could provide an explanation for the positron excess in the cosmic rays reported by PAMELA [32]. In addition, this model can accommodate inflation [67], provide a unified picture of inflation and dark matter [68], and give rise to interesting predictions for neutrinoless double beta decay experiments [116].

6.4 Distinguishing Neutrino Final State from W and Tau Final States

MSSM neutralino annihilation predominantly produces gauge bosons and charged fermions, each of which in turn produce secondary neutrinos via two-body or three-body decays. In this work, we adopt a model-independent approach and consider interesting neutrino spectra from DM annihilation to prompt ν's, W's, and τ's.

For charged fermions, we investigate only annihilation to τ's for the following reasons. e's and μ's are stopped immediately in the sun, so μ decay will occur at low energy and result in a very soft spectrum. When DM annihilation produces quarks, all quarks except the t-quark hadronize before their subsequent decay. The t-quark decays to a W boson and a b-quark before hadronization, and the subsequent W decay produces a neutrino spectrum comparable to that from the W final state. For the remaining hadronizing quarks, the lighter the quark the longer it will take to decay, and hence the lower its energy will be. The b-quark produces neutrinos via three-body decay, which has a softer spectrum than that from τ. All other quarks decay effectively at rest and have unmeasurable spectra at low energies that cannot compete with the atmospheric background [91].

With regard to gauge boson final states, W and Z spectra are relatively similar; we consider only W final states in our analysis. Finally, the Higgs boson final states also result in a soft neutrino spectrum that is negligible compared to that from W and τ final states. The Higgs mainly decays to b-quarks, thus yielding a neutrino spectrum similar to that from the b-quark final state.

In the following, we therefore focus on secondary neutrinos from DM annihilation to W and τ final states vs primary neutrinos and their corresponding spectra. Previous investigations have shown that measuring the spectrum can allow the reconstruction of the DM mass and its annihilation branching ratios [118]. We perform an analysis for reconstructing the DM elastic scattering cross section and its annihilation channels, including experimental error in energy reconstruction and assuming that its mass can be determined from other experiments (notably by the LHC).

6.4.1 Neutrino & Contained Muon Spectra

In this analysis, we consider the spectrum of contained muon tracks so that the vertex at which ν_μ is converted to a μ is within the detector volume. Hadronic and electromagnetic cascade events in the ice also carry useful information about low energy neutrinos and may show tau neutrino appearance from oscillations [119]. IC/DC is uniquely suited to measure these low energy events and recently confirmed the observation of neutrino-induced cascades [109]. For our purposes, since cascades are localized in the ice and thus suffer from an angular resolution of about 60 degrees at 100 GeV, too much background is admitted to perform a meaningful DM search with cascades [120].

We use DarkSUSY to calculate the spectrum for any given final state [73]. To the extent that the energy of the event may be well reconstructed in this range, we also assume that the muon track itself is fully contained, ending inside the detector. We do not account for any loss of events or poor energy reconstruction at the edges of the fiducial volume.

As an example, Fig. 6.1 depicts the theoretical prediction for neutrino and muon spectra that result from the annihilation of 100 GeV DM particles in the sun to prompt ν_μ's, W's and τ's. The flux is given in events per km^3 effective volume of the detector at earth per year. Only a half-year of data is taken for each calendar year, since we assume the neutrino telescope requires the sun to be below the horizon to observe the DM neutrino signal above the atmospheric muon background. For a

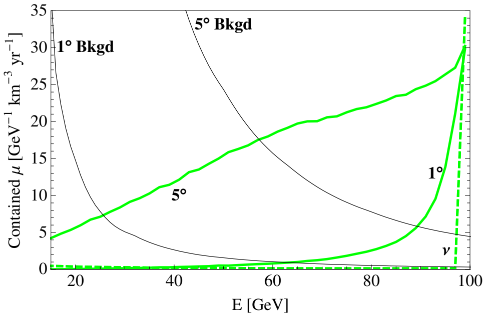

(a) **Annihilation to ν final state**

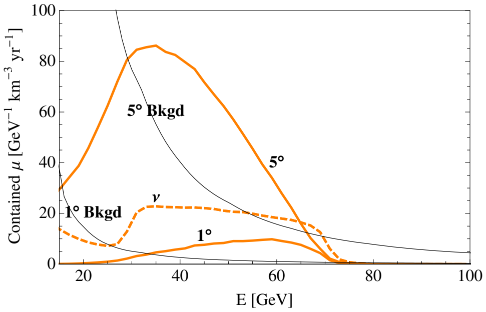

(b) **Annihilation to W final state**

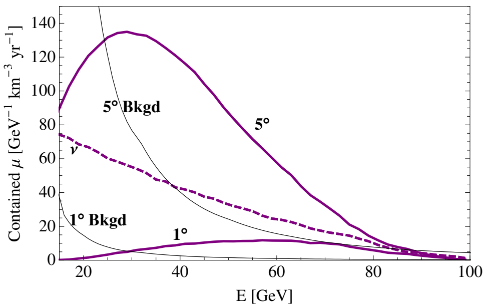

(c) **Annihilation to τ final state**

Figure 6.1: Energy spectra of contained muon events (solid) and incident neutrinos (dashed) at the earth from a 100 GeV DM particle for various annihilation channels. Relative to the sun 1°, 5° angular cuts have been placed on the signal and atmospheric background muons (thin black lines). The top plot for annihilation to neutrinos is for $\sigma_{\rm SD} = 10^{-41}$ cm^2, while the other plots are for $\sigma_{\rm SD} = 10^{-40}$ cm^2, all of which are below the current experimental bounds. Normal mass hierarchy and $\theta_{13} = 10°$ have been chosen here, but the spectra are largely insensitive to the oscillation parameters.

DM mass of 100 GeV the muons will be fully contained and accessible in IC. The qualitative features of the neutrino and muon spectra (such as peaks and kinematic cutoffs) are the same for higher DM masses.

The prompt neutrinos, Fig. 6.1a, result in a monochromatic peak at the DM mass in the neutrino spectrum. The contained muon spectrum is plotted along with the neutrino spectrum to emphasize the effect of the charged current conversion of neutrinos to muons. The conversion demonstrates the weak scale reduction in events relative to the incident neutrinos and is proportional to energy, so the peak from the neutrino annihilation channel is well preserved. The spectra are largely insensitive to the choice of neutrino oscillation parameters and annihilating neutrino flavor. Here we depict $\theta_{13} = 10^\circ$, normal mass hierarchy and annihilation to ν_μ, but scenarios with inverted mass hierarchy, $0 \leq \theta_{13} < 10^\circ$ and other neutrino flavors in the final state only slightly change the height of the peak.[4]

The W bosons produce neutrinos via two-body decay, which are softer than the previous case. For a highly boosted W (whose energy is equal to the DM mass), the energy of secondary neutrinos is between $M_W^2/4M_{DM}$ and $M_{DM}/\sqrt{2}$. This is the reason for the relatively sharp kinematic edges in the neutrino spectrum in Fig. 6.1b. We note that W's also decay to b-quarks, which in turn produce tertiary neutrinos. This results in additional contributions to the neutrino spectrum lower than the kinematic cutoff mentioned above. The muon spectrum has a peak at energies well below the DM mass resulting from charged current interactions whose cross section is proportional to the neutrino energy.

The τ's produce neutrinos via three-body decays, which results in a much softer neutrino spectrum that rises toward lower energies as seen in Fig. 6.1c. Thus the peak of the resulting muon spectrum is located at a lower energy than that in Fig. 6.1b.

---

[4] Recent results from T2K [121] and MINOS [122] experiments suggest nonzero θ_{13} at 2.5σ and 89% confidence respectively. The results are consistent with $\theta_{13} = 10^\circ$.

However, there is no kinematic cutoff in the neutrino spectrum in this case, and hence the muon spectrum extends smoothly to the DM mass.

The important point is that there is a distinct separation in energy between the contained muon peak of prompt neutrinos at the DM mass and the W and τ peaks at lower energies. This indicates that scenarios with DM annihilation to primary neutrinos can be distinguished from those with DM annihilating to W bosons or τ's. Moreover, were a model to contain both a neutrino final state and a W or τ final state, the neutrino signal may be used to determine the corresponding branching ratios.

6.4.2 Reconstruction of Annihilation Channels

The theoretical predictions shown in the previous subsection are subject to experimental error. Individual muon events from a particular annihilation channel cannot be tagged as such, nor can individual signal and background events be distinguished. A more realistic picture is shown in Fig. 6.2 for a 100 GeV DM particle, where two channels along with background events have been added together and subjected to a 5° angular cut. The branching ratios are 90% to W bosons and 10% to neutrinos with $\sigma_{\rm SD} = 10^{-40}{\rm cm}^2$. This is a factor of a few below the current bounds from IC [29] and just at the current bounds of Super Kamiokande (SuperK) for annihilation to W's [123].[5]

Angular cuts on the muon tracks relative to the position of the sun lower the relevant atmospheric contained muon background relative to the signal. Lower energy events are preferentially scattered at higher angles relative to the incoming neutrino;

---

[5] For a purely spin-independent cross section, the same result is obtained for $\sigma_{\rm SI} \approx 3 \times 10^{-43}$ cm^2. However, such a large value of $\sigma_{\rm SI}$ is already ruled out by direct detection experiments [104]. For this reason we focus on the spin-dependent cross sections in this analysis.

therefore, angular cuts disproportionately remove low energy events. A 1° cut leaves the majority of the high energy muons from primary neutrinos, which are clearly separated from a reduced background. Meanwhile, a 5° cut admits more lower energy muons that are indicative of the pronounced peaks from W and τ final states. Different angular cuts will optimize the signal to background ratio for different annihilation channels. We have found a 5° cut to be optimal, where the background does not overwhelm the signal in the regime above 40 GeV and a significant portion of the W peak remains. The contribution from neutrinos is still easily distinguished in the peak cutoff.

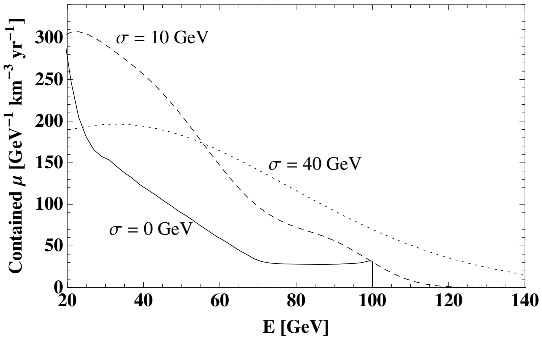

Figure 6.2: Total contained muon spectrum from a 100 GeV DM particle with $\sigma_{\rm SD} = 10^{-40}$ cm^2 annihilating to W's (90%) and ν's (10%) with the atmospheric background added. A 5° cut has been placed on the events. Smeared spectra for energy reconstruction errors of 10 GeV (dashed) and 40 GeV (dotted) are also shown.

The realistic energy reconstruction for a contained muon spectrum at IC for these energies is not certain. Energy reconstruction for through-going TeV muons is approximately $\sigma_{\log_{10} E} = 0.3$ [107]. Energy loss of the muon is described by

$$\frac{dE}{dx} = a + bE \ , \tag{6.2}$$

where a quantifies muon loss via ionization, and b quantifies loss from pair productions, Brehmsstrahlung radiation and nuclear interactions. For ice at energies above 1 TeV, enough Brehmsstrahlung and pair production occurs to ensure that the light deposited in the detector is proportional to the muon energy. However, for contained muon events less than one kilometer in extent, the track length is proportional to the muon energy. Reconstruction in this regime will be better than in the regime above 1 TeV but will depend on the geometry of the detector.

The energy resolution error of the IC detector for contained muon events below 100 GeV should be linear with energy, in that the track length is proportional to the energy of the incoming muon. In Fig. 6.2, we recreate a Gaussian energy reconstruction with an error, or width, equal to 10 or 40 GeV. This is equivalent to claiming that the track length can be known to within $50 - 200$ m, a resolution that seems feasible for IC/DC to IC-like telescopes since IC/DC DOMs are spaced at 7 m vertically and strings are 72 m apart while IC DOMs are spaced at 17 m vertically and strings are 125 m apart.

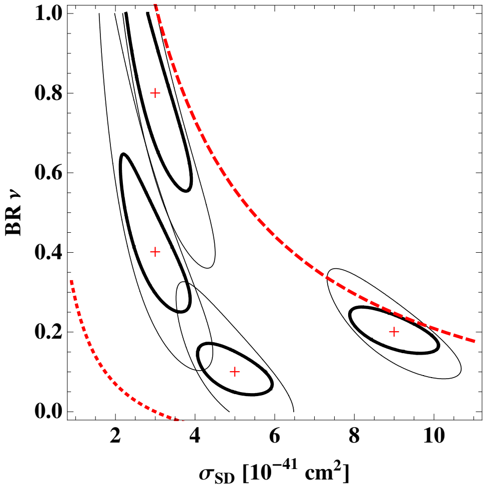

Figure 6.3: Contours of 2σ confidence for reconstructing spin-dependent cross section $\sigma_{\rm SD}$ and branching ratio to prompt neutrinos BR_ν for a 100 GeV DM particle annihilating to ν's and W's. One year of data is used with energy reconstruction errors of 10 or 40 GeV (thick or thin contours). The region of interest is between the current SuperK upper bound (dashed) [123] and the future IC86 sensitivity bound (dotted) [115].

It is seen that the smoothing of the spectrum considerably suppresses the distinct channel features, especially for a 40 GeV error in energy reconstruction. Nevertheless, it is still possible to reconstruct the total spin-dependent scattering cross section $\sigma_{\rm SD}$ and the branching ratio for annihilation to primary neutrinos $\rm BR_\nu$.

In Fig. 6.3 we show the 2σ confidence contours for a 100 GeV DM particle annihilating to ν and W final states, using one year of data and applying energy reconstruction errors of 10 GeV and 40 GeV. These contours account for Poisson errors, the addition of background and a 40 GeV energy cut; we have used the χ^2 analysis in [124] to obtain these results.

The plot in Fig. 6.3 also shows the current SuperK bound [123] and the future IC sensitivity bound [115] on $\sigma_{\rm SD}$ (dashed and dotted curves respectively). For 100% DM annihilation to W's, the experiments have derived bounds on $\sigma_{\rm SD}$ by applying appropriate energy and angular cuts on the muon spectrum. No limit has been placed yet for DM annihilation to primary neutrinos by either experiment. In the absence of a thorough analysis, we have used a simple criterion to find an approximate bound on $\sigma_{\rm SD}$ for the neutrino final states. We compared the total number of contained muon events with a 40 GeV energy threshold and 5° angular cut for the two final states. In the case of primary neutrinos, the flux of μ's is about eight times larger than the flux from W's, as expected from the harder neutrino spectrum. We assumed the limit on $\sigma_{\rm SD}$ in this case is also tighter by the same factor. A dedicated analysis for the neutrino final state, with optimized angular and energy cuts, would result in a more precise bound. Indeed, theoretical motivation for models with DM annihilation to primary neutrinos warrants such a study by experimental collaborations. In the presence of both ν and W final states, the limits are approximately given by

$$\sigma_{\rm SD}\,(1 + 7\ {\rm BR}_\nu) \leq \sigma_{\rm max}\,. \tag{6.3}$$

The current bound from SuperK [123] and the future IC sensitivity bound [115] correspond to $\sigma_{\rm max} \approx 2.5 \times 10^{-40}$ and 4×10^{-41} cm^2 respectively.

It is seen from the shape of the contours that higher $\sigma_{\rm SD}$ and smaller BR_ν are difficult to distinguish from lower $\sigma_{\rm SD}$ and larger BR_ν. The number of muon events at the DM mass mainly comes from the peak of primary neutrinos, which is determined by BR_ν. This holds after smoothing of the spectrum because of the kinematic cutoff that appears well below the DM mass for annihilation to W's, see Fig. 6.1b. This implies that after smearing the main contribution to the total spectrum at energies around and above the DM mass still comes from primary neutrinos. On the other hand, the main contribution to lower energy muons comes from secondary neutrinos produced by W decay. For small values of $\sigma_{\rm SD}$ or large values of BR_ν, this contribution is small and overwhelmed by the Poisson error from the atmospheric background. Therefore, one can compensate for a change in $\sigma_{\rm SD}$ by a corresponding change in BR_ν and obtain spectra that are statistically indistinguishable. For larger values of $\sigma_{\rm SD}$ or smaller values of BR_ν, the contribution of secondary neutrinos becomes significant, which limits simultaneous variations in $\sigma_{\rm SD}$ and BR_ν that keep the peak height unchanged. As a result, the 2σ contours are tighter for reconstruction points toward the right and bottom of the plot in Fig. 6.3. As expected, an energy reconstruction error of 40 GeV does a poorer job because it further suppresses the features discussed above.

In Fig. 6.4 we show the 2σ confidence contours from a similar analysis for annihilation to ν's and τ's. The contours are wider in this case, which implies the reconstruction is significantly more difficult. This is due to the different shapes for the W and τ final state spectra, see Figs. 6.1b and 6.1c. In the case of the τ final state, the spectrum resulting from secondary neutrinos is softer and extends all the way to the DM mass. Therefore secondary neutrinos can make a significant contribution to the total spectrum at energies around and above the DM mass after energy reconstruction and are also affected more by the background at lower energies. Both of these effects imply a poorer reconstruction of the branching ratios in this case.

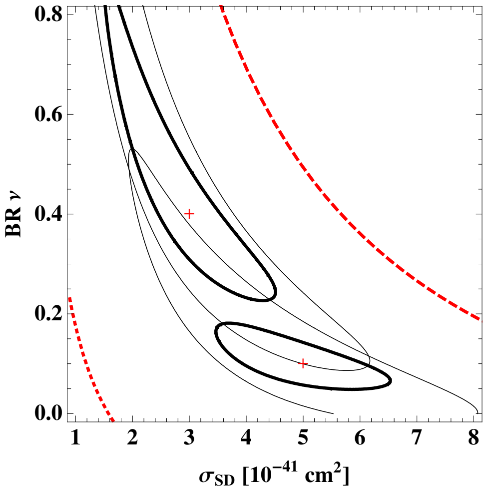

Figure 6.4: The same as Fig. 6.3, but for annihilation to ν and τ final states.

Some comments are in order. In producing these figures, a scan of angular cuts in 1° increments within the $1° - 10°$ range was made. While visually a 1° cut may be optimal in distinguishing the presence of the neutrino channel, a 5° cut was optimal in reconstructing the branching ratios in the presence of the broad, low energy W or τ spectrum.

We also note that the muon event rates for both the signal and background must be convolved with the effective volume of the detector for contained muon events, which is a function of energy. IC/DC maintains significant volume above 10 GeV [109]. While the geometric volume for IC/DC is about 3% of the volume of IC, the more dense spacing of DOMs in IC/DC make it more efficient at event detections for energies below 100 GeV [109]. The effective volume in this range increases with energy as longer muon tracks are more likely to produce detectable light. This can make the effect of the peak at the DM mass from primary neutrinos even more distinctive above the smeared W or τ spectrum. The reconstruction can therefore be better than shown here after accounting for the energy dependence of the effective volume.

Finally, one year results for a km^3 effective volume, with the sun below the horizon, translate to roughly ten years of a 0.05 km^3 detector capable of operating for a full year. Thus, in the region of IC and IC/DC sensitivity that would yield a discovery of prompt neutrinos after one year, 10 years of data could allow reconstruction of the branching ratios for the IC/DC effective volume. A larger detector with the same capabilities can significantly improve these prospects.

6.5 Distinguishing Neutrino Flavors

Once the presence of direct DM annihilation to neutrinos is confirmed, it is desirable to also learn the flavor of the final state neutrinos. This will provide specific information about models that connect DM to the neutrino sector. For example, in the $U(1)_{B-L}$ extension of MSSM where the lightest RH sneutrino is the DM candidate [2], flavor composition of final state neutrinos is related to the neutrino Yukawa couplings. Therefore, knowledge of the neutrino flavors will yield useful information pertaining to the underlying neutrino mass model and leptogenesis.

Here we show how regeneration of ν_τ inside the sun and its effect on the muon spectrum may be used as a novel method to distinguish the flavor of primary neutrinos in the final state.[6]

6.5.1 The ν_τ Regeneration Effect

DM annihilation produces neutrinos in flavor eigenstates in the sun. Neutrinos then undergo charged current interactions with matter as they propagate through the sun. These interactions convert ν_e, ν_μ, ν_τ to e, μ, τ respectively. e's and μ's are

---

[6] It has been proposed that seasonal variation of the neutrino signal may also be used to extract information about the flavor of primary neutrinos [125].

stopped immediately due to electromagnetic interactions. On the other hand, the τ decays quickly before losing too much energy because of its very short lifetime of 3×10^{-13} s [126]. This decay produces a ν_τ, which has a lower energy than the original one. Charged current interactions therefore suppress the peak of the neutrino spectrum at the DM mass for all flavors.[7] However, in the case of the ν_τ, the regeneration of neutrinos via three-body decay populates the spectrum at energies well below the DM mass.

The cross section for charged current interactions is proportional to the energy of primary neutrinos produced at the center of the sun, which is essentially equal to the DM mass. Neutrino absorption becomes significant when the absorption length of neutrinos $L_{\rm abs}$ is roughly equivalent to the core size of the sun $R_C \sim 70,000$ km. Using the charged current neutrino-nucleon cross section [127] and a core density of 150 g/cm^3, we find that $L_{\rm abs} \sim 70,000$ km at energies $E_\nu \sim 300$ GeV. Oscillations among different flavors should be taken into account as neutrinos travel through the sun. We note that for ν_e the flavor and mass eigenstates are the same deep inside the sun. This implies that upon production at the center of the sun ν_e's propagate through the core without changing their flavor. Thus absorption via charged current interactions start to suppress the flux of ν_e for DM masses above 300 GeV as discussed above.

On the other hand, ν_μ and ν_τ are not mass eigenstates inside the sun, and hence undergo oscillations. Since matter effects are the same for these two flavors, the $\nu_\mu - \nu_\tau$ oscillation length inside the sun is set by the atmospheric mass splitting $L_{\rm osc} = E_\nu / 4\pi \Delta m^2_{\rm atm}$. As long as $L_{\rm abs} \gtrsim L_{\rm osc}/4$, oscillations mix ν_μ and ν_τ efficiently before the absorption becomes important. As a result, ν_μ final states also feel the

---

[7] Neutrinos also have neutral current interactions with matter inside the sun. Scatterings via neutral current interactions result in energy loss of the neutrinos and further suppress the peak at the DM mass. However, the cross section for neutral current interactions is a factor of 3 smaller than that for charged current interactions, which makes them subdominant. More importantly, neutral current scatterings affect all flavors equally.

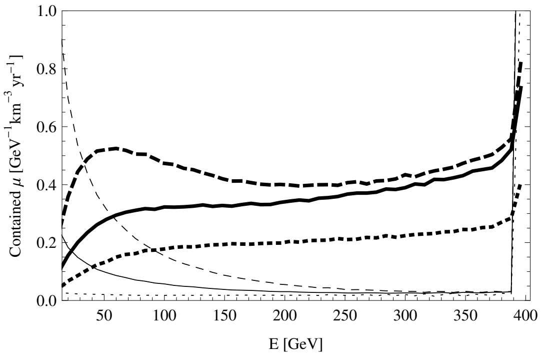

(a) **400 GeV DM mass**

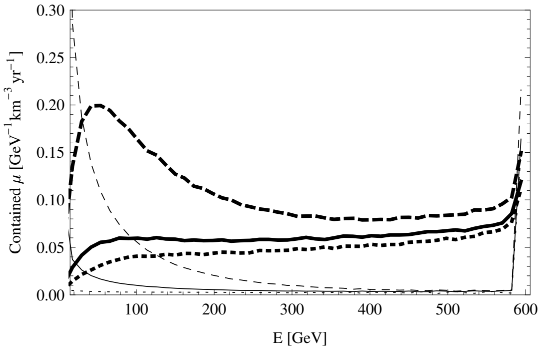

(b) **600 GeV DM mass**

Figure 6.5: Contained muon spectra for DM annihilation to ν_e (dotted), ν_μ (solid) and ν_τ (dashed) for 400 (Fig. 6.5a) and 600 GeV (Fig. 6.5b) DM masses and $\sigma_{\rm DM} = 10^{-41}$ cm^2. Normal mass hierarchy and $\theta_{13} = 10°$ are chosen here, but substantive features of the spectra do not depend on the neutrino oscillation scenario. A 5° cut has been placed on the events. Corresponding neutrino spectra are shown in thin lines. The regeneration effect is evident for the ν_τ final state and results in a peak in the muon spectrum at low energies. For a 400 GeV DM particle, regeneration also affects the ν_μ final state due to efficiency of $\nu_\mu - \nu_\tau$ oscillations inside the sun.

regeneration effect. Since $L_{\rm abs} \propto E_\nu^{-1}$ and $L_{\rm osc} \propto E_\nu$, at sufficiently high energies $L_{\rm abs}$ drops below $L_{\rm osc}/4$. This happens for a DM mass of about 500 GeV. Starting at this point, $\nu_\mu - \nu_\tau$ oscillations cease to be effective. Hence ν_μ gets absorbed through charged current interactions similar to ν_e. In consequence, only the ν_τ final state retains a significant regeneration signature for DM masses above 500 GeV.

In Fig. 6.5 we show the muon and neutrino spectra for different flavors of primary neutrinos. As we see in Fig. 6.5a, the ν_μ channel shows some regeneration effect for a 400 GeV particle, which makes it distinguishable from the ν_e channel. For a 600 GeV DM particle, see Fig. 6.5b, the $\nu_\mu - \nu_\tau$ oscillations are inefficient. Therefore, only the ν_τ channel shows significant regeneration, which makes it distinguishable from the ν_μ and ν_e channels. The regeneration effect results in a peak in the muon spectrum at low energies, which becomes more pronounced as the DM mass increases. These figures are for the normal hierarchy of neutrinos and $\theta_{13} = 10°$, but variations in the neutrino oscillation scheme do not change the substantive features of the spectra.

6.5.2 Signals of Neutrino Flavor

As we saw, the ν_τ regeneration effect becomes significant at DM masses above 300 GeV. The background from atmospheric neutrinos is relatively small at such energies due to the power law decrease in cosmic ray background. However, the neutrino signal from DM annihilation is also kinematically suppressed for heavier DM masses. This leaves few events to detect in the interesting range of the spectrum where a regeneration peak is evident. Additionally, energy reconstruction for the contained muon spectrum above 300 GeV begins to suffer from logarithmic error in energy since the reconstruction also depends on the amount of light produced in Brehmsstrahlung radiation and pair production. Events cannot be fully contained at these energies, so reconstruction efforts based on track length are imprecise.[8]

To mitigate these experimental challenges, we integrate the contained muon events above a threshold to consider if the cumulative effect of the regeneration is visible. In Fig. 6.6 we show the integrated events above 60 GeV with a 5° angular cut, which readily retains the low energy regeneration effect. One can see the separation between the ν_e channel and the ν_μ, ν_τ channels above 300 GeV, and between

---

[8] If the energy of the corresponding cascades accompanying the muon event can also be captured, energy reconstruction would be improved.

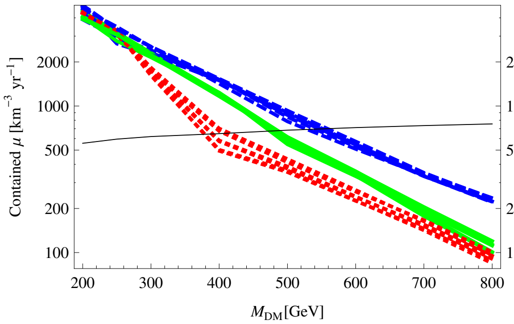

Figure 6.6: Integrated muon spectra from 60 GeV to the DM mass with a 5° angular cut as a function of DM mass for $\sigma_{\rm SD} = 10^{-40}$ cm^2. The dotted, solid and dashed lines denote the ν_e, ν_μ and ν_τ final states respectively. The bands of lines for each flavor depict different oscillation scenarios (normal and inverted mass hierarchy as well as $0 \leq \theta_{13} \leq 10°$). The separation between the ν_τ and ν_e exceeds the Poisson error of the signal and background (black line) for DM masses above 300 GeV, and the ν_τ becomes distinguishable from ν_μ above 600 GeV as well.

the ν_τ channel and the ν_e, ν_μ channels above 500 GeV (as discussed above). Separation between signals from different channels is typically larger than the Poisson error of the background and signal together. The background and signal are shown separately since the background may be subtracted from the signal by observing away from the sun, off-source, as is done in galactic center DM searches [115]. We also note that the oscillation scenario does not significantly affect these results. The bands of lines depicting the normal and inverted hierarchies as well as θ_{13} ranging from 0 to 10° for each flavor do not overlap at DM masses above 300 GeV. These results assume $\sigma_{\rm SD} = 10^{-40}$cm^2, which is compatible with the current bounds from IC for heavier DM, and is within the reach of IC/DC sensitivity limits [115].

If the elastic scattering cross section of the DM is known, then a simple integration as in Fig. 6.6 will be sufficient to distinguish the flavor of primary neutrinos by using the regeneration effect. However, a confirmation of annihilation to primary neutrinos would likely come from the presence of a monochromatic peak alone, the height of which depends on the scattering cross section. In the absence of information about

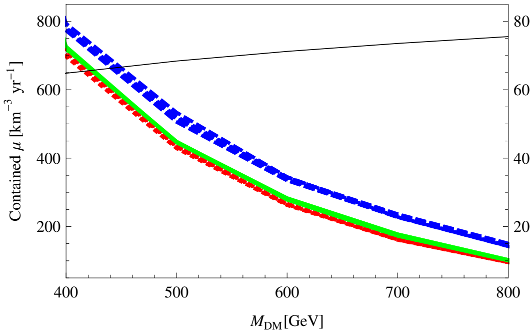

Figure 6.7: The same as in Fig. 6.6 after normalization to account for unknown value of the DM elastic scattering cross section. The normalized spectra give the same number of events (when integrated from 200 GeV to the DM mass for a 1° angular cut) as the ν_μ final state for normal mass hierarchy and $\theta_{13} = 10°$. The separation between the ν_τ and other flavors still exceeds the Poisson error of the signal and background (black line).

the cross section, we then need to normalize the signal to extract information about the neutrino flavor. The height of the peak in the muon spectrum is closely related to the height of the neutrino peak. However, for DM masses above 300 GeV, for which the regeneration effect becomes important, muon events at the peak are not fully contained. It will be most difficult to reconstruct the energy of these events without track-length information. Instead, we integrate muon events above 200 GeV, which are essentially the through-going muons, using a 1° angular cut on the muon spectrum in order to best capture the monochromatic peak. We then use this to normalize the integrated muon flux above 60 GeV with a 5° cut to retain the maximum effect of regeneration at low energies.

The normalization accounts for the lack of knowledge in the value of the DM elastic scattering cross section, and to a lesser extent the oscillation parameters. After normalization, see Fig. 6.7, the separation between the ν_τ channel and the ν_e, ν_μ channels remains and is still larger than the statistical error of the background and signal together. Using the regeneration effect, the IC/DC effective volume could reasonably yield a determination of the neutrino flavor after 10 full years of operation.

6.6 Conclusion

We have investigated prospects of determining DM annihilation final states with neutrino telescopes by using the spectrum of contained muon tracks from conversion of neutrinos that are produced in the annihilation of DM particles trapped inside the sun. Our focus was on distinguishing neutrino final states from gauge boson and tau final states and on discriminating the flavor of final state neutrinos. Gauge boson and tau final states are typically the dominant annihilation channels in supersymmetric models with neutralino DM, while direct annihilation into neutrinos can occur in models that connect DM to the neutrino sector. The theoretical motivation for the latter could provide the grounds for a dedicated analysis by the IceCube Collaboration to put stringent bounds on annihilation to primary neutrinos, similar to what has been done for annihilation to gauge bosons [29].

Primary neutrinos from DM annihilation result in a distinct peak in the muon spectrum at the DM mass. For DM masses below 300 GeV we can expect that the peak will be accessible to a detector the size of IC. The spectrum is smeared as a result of the experimental error in energy reconstruction, but primary neutrinos may be distinguished from gauge boson and tau final states after this effect is taken into account. We showed that for an energy resolution of 10 GeV (as in IC/DC) and by making an optimal angular cut on the muons (which we found to be 5°), the branching ratios may be determined in the parameter space within the reach of the one-year sensitivity limits of IC/DC with a km^3/yr of data. This is roughly equivalent to 10 years of data for a detector with the same capabilities and effective volume as IC/DC.

The regeneration of ν_τ inside the sun may be used to distinguish the flavor of final state primary neutrinos. This effect becomes important for DM masses above 300 GeV and populates the spectrum with muons whose energy is well below the energy of primary neutrinos. For DM masses up to about 500 GeV, oscillations mix ν_μ and ν_τ effectively, which implies that regeneration affects final states with ν_μ and ν_τ similarly. Final states with ν_e are therefore distinguishable within this mass range. For heavier DM particles, the $\nu_\mu - \nu_\tau$ oscillation becomes inefficient. As a result, ν_τ final states are picked out by the regeneration effect for DM masses above 500 GeV. We showed that final states with ν_τ stand out at a statistically significant level for DM masses as heavy as 800 GeV, even after normalizing the muon spectrum to the total event count (to account for the unknown DM-nucleon elastic scattering cross section). Again, such a distinction may be achieved with 10 years of data from IC/DC.

In summary, using the the IC results in tandem with independent measurements of the DM mass (for example, from the LHC), will allow us to identify the annihilation channels of DM with multi-year data. Improved energy resolution and increased effective volume of the detector will greatly help in achieving this goal.

6.7 Acknowledgements

The authors wish to thank Bernard Becker, Tyce DeYoung, Arman Esamili, Yasaman Farzan, Alexander Friedland, Francis Halzen, Spencer Klein, Robert Lauer, Irina Mocioiu, and Carsten Rott for valuable discussions.

Chapter 7

Conclusion

7.1 Summary of Major Results

In Chapters 3 and 4 we have fit the PAMELA and ATIC positron excesses with an s-wave Sommerfeld enhanced leptophilic WIMP. While many models can achieve this fit with the same characteriscs, a $U(1)_{B-L}$ extension of the MSSM, theoretically motivated by the need to explain neutrino masses and mixings, produces two novel dark matter candidates: the new neutralino, a mixture of the new Higgsino charged under $B-L$ and the new zino, and the right handed sneutrino. Both of these candidates can produce the correct relic density in a thermal history and can generate a positron excess and no anti-proton excess thanks to the leptophilic bias of the $B-L$ charges. The Sommerfeld effect from exchange of a light $B-L$ Higgs enhances the signal between three and four orders of magnitude, creating the enhanced positron flux needed to match the data.

As the work of Chapters 3 and 4 was completed three years ago, a few updating remarks are in order. First, new upper bounds from Fermi in the diffuse signal show that DM annihilation to taus would produce too many photons and is excluded by the diffuse flux measurements [30]. Annihilation to muons may soon be excluded as well. The FERMI-LAT collaboration has demonstrated that this is a robust prediction for Einasto, Isothermal and NFW profiles alike. Additionally, bounds from a joint analysis of a few close galactic clusters are rapidly approaching the region of interest for the Fermi and PAMELA data. These results cast doubt on a DM annihilation interpretation of the PAMELA and ATIC positron excesses [47]. The concerns expressed in Chapter 2 regarding the velocity dependence and uncertainties in the velocity dispersion may relax these bounds slightly.

Pulsars are also expected to expend some spin-down energy in the emission of positrons and electrons and may adequately describe the signal [128]. In fact, ten Fermi pulsars contribute signficantly to the positron flux and may explain the Fermi measurements with older and closer pulsars contributing as much as one percent or more to the measured $e^+ + e^-$ flux at 100 GeV [129].

Finally, limits on Sommerfeld enhancement indicate that including resonant enhancement both at the time of freeze-out as well as today means that S cannot exceed 100 [43], whereas three or four orders of magnitude are needed to explain the PAMELA data for a thermally produced WIMP. Furthermore, Sommerfeld enhancement would also distort light elemental abundances, and bounds from Lithium in particular begin to encroach on a total annihilation rate of $O(10^{-24}\ \mathrm{cm}^3/\mathrm{s})$ depending on the annihilation final states [82]. Additionally, limits from the ellipticity of the halo of galaxy cluster NGC 720 exclude mediators less than 30 GeV. However, as mentioned in Chapter 2, modifications in substructure assumptions may relax some of these constraints. Regardless of whether the positron excess is ultimately interpreted as a signature of annihilating dark matter, the work of Chapters 3 and 4 demonstrate how data encourage an examination of physical assumptions and the exploration of models beyond the simplest supersymmetric dark matter.

In Chapter 5, we demonstrated that annihilation of sneutrino DM in this model results in a signal detectable above background by neutrino telescopes and distinguishable from mSUGRA hyperbolic branhc/focus point models. Furthermore, if a DM disc exists, the density of dark matter accumulated in the earth is great enough to achieve equilbrium, and annihilation is enhanced so that an earth signal is detectable over a wide range of possible DM velocity dispersion parameters, all while not exceeding current bounds from annihilation in the sun.

In Chapter 6, we took a model independent approach and showed that even with realistic energy reconstruction it is possible to detect DM annihilaton to νs even in the presence of Ws/τs assuming that IC makes a DM discovery in the spin-dependent scattering cross section. Additionally, we found that the tau regeneration effect presents the possibility of distinguishing between DM annihilation to the three different neutrino flavors for masses above about 400 GeV.

7.2 Upcoming experiments & Projected Sensitivities

A host of upcoming experiments and results indicate that the cosmologically relevant region of DM parameter space will continue to be pressured.

The AMS-02 (Alpha Magnetic Spectrometer) detector aboard the International Space Station is set to place unprecedented limits on a host of charged cosmic rays, including protons, antiprotons and other nuclei. AMS-02 will be able to produce an order of magnitude improvement after just one year in the measurement of the annihilation rate. AMS-02 will be able to confirm or reject models of heavy DM in the region of $1 - 4$ TeV as considered in Chapters 3 and 4 [130]. The HESS Cerenokov telescope has indicated that the positron fraction increase seen by PAMELA and Fermi in fact downturns near a TeV [131]. AMS-02 presents the promising opportunity to confirm these results with greater sensitivity; see Fig. 7.1 for a comparison of current measurements of the positron spectrum.

Future lines of inquiry for dark matter indirect detection include observations in the X-ray and radio wavelengths. The Absolute Radiometer for Cosmology, Astrophysics and Diffuse Emission-2 (ARCADE-2) detected diffuse and isotropic emission of radio waves in excess of expectations from galactic sources and even unresolved galactic radio sources. The emission is consistent with leptonically annihilating dark matter [133]. The hard X-ray band encompasses the peak of Inverse Compton scattering from electrons and positrons from a wide-array of annihilating dark matter models. While NuSTAR will achieve Fermi-type sensitivity after long observations, Athena WFI could exceed Fermi sensitivity for low mass models if it were placed in

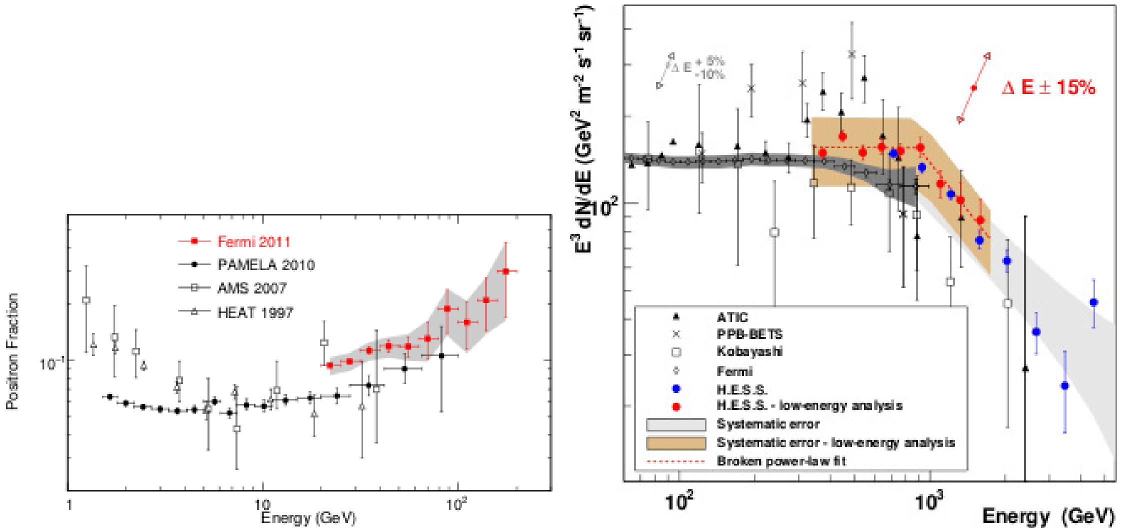

Figure 7.1: Left panel: Fermi and PAMELA measurements of the positron fraction are in statistical agreement [132]. Right panel: HESS positron fraction as compared to the Fermi measurements indicates a broken power-law fit to the spectrum [131].

a low background orbit [134].

Annihilation rates aside, the Planck satellite has ten times the sensitivity of WMAP and will be able to probe the power spectrum of the CMB to smaller scales. It will deliver measurements of the polarization of the CMB that have implications for inflation. Planck will discover new galaxy clusters by measuring the Sunyaev-Zel'dovich effect that lowers CMB photon temperatures after hot electrons from the intercluster medium inverse Compton scatter [135]. The discovery of new, high redshift clusters will provide concrete observations of the growth of structure and inform N-body simulations.

Future lensing surveys such as the Large Scale Synoptic Telescope promise to discover more spheroidal satellites than those found by SDSS and to better constrain the growth of structure as they probe mass structure through lensing beyond z=1. This will have profound implications for limits on dark matter self-interaction, will provide confirmation of dark matter density measured by WMAP and Planck and

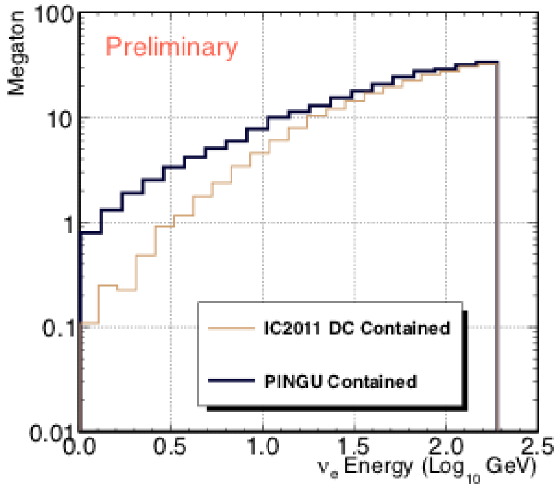

Figure 7.2: Effective volume comparison of DeepCore and the proposed PINGU extension to IceCube [109].

will ultimately measure the dark energy equation of state parameter and its time derivative to within a few and ten to twenty percent respectively.

With regard to the spin-dependent WIMP-nucleon cross section, the IceCube Collaboration is considering a Phased IceCube Next Generation Upgrade, or PINGU, an extension to its DeepCore instrumentation in which about twenty new strings with high quantum efficiency detectors as used in DeepCore would be added to the array. PINGU would extend the IC/DC sensitivity by a factor of a few, see Fig. 7.2, and could detect neutrinos of a few GeV [109]. A European collaboration is also working on Km3net, a deployment of PMTs in the Mediterranean, that could place constraints for galactic substructure. If such a project also involved a DeepCore like component, it is expected to exceed IceCube sensitivities by a factor of ten for measurements of cascades [136].

Additionaly, constraints on the spin-independent elastic scattering cross section are projected to improve as the next generation of detectors is completed Fig. 7.3. The one ton version of Xenon will provide two orders of magnitude improvement

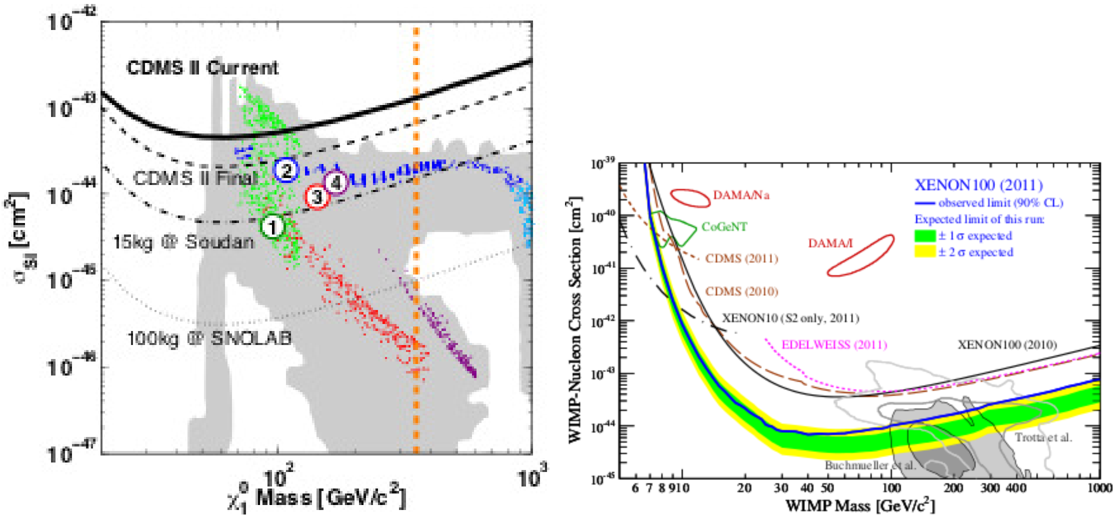

Figure 7.3: σ_{SI} current sensitivity of CDMS II and projected sensitivity of SuperCDMS (left) [137] and current sensitivity of Xenon100 (right) [138]. The orange line in the left panel indications the upper mass limit of the LHC search.

on the Xenon100 upgrade [139], while CDMS predicts two orders of magnitude improvement in the construction of SuperCDMS compared to projected final CDMS II results [137], see Fig. 7.4 for a comparison of projected sensitivities.

Recent LHC 7 TeV searches for the Standard Model Higgs have yielded exclusions above 128 GeV in CMS [143] and 129 GeV in the case of the ATLAS collaboration [144]. An excess of events is seen by both collaborations in the 125 and 126 GeV regions; whether these events are statistical pile ups or represent the discovery of the Standard Model Higgs should be resolved by the end of 2012 at which time the statistical signficance could approach a five sigma discovery confirmation. At the same time, ongoing searches for supersymmetry have failed to yield positive discoveries from CMS and ATLAS [145, 146] and in particular have not observed multi-jet or multi-lepton plus missing energy signals. The implication is that squarks and gluinos are excluded up to 1.4 TeV if their masses are equal, or squarks are excluded up to 0.8 TeV in the case of squarks heavier than gluinos. See [147] and references therein for

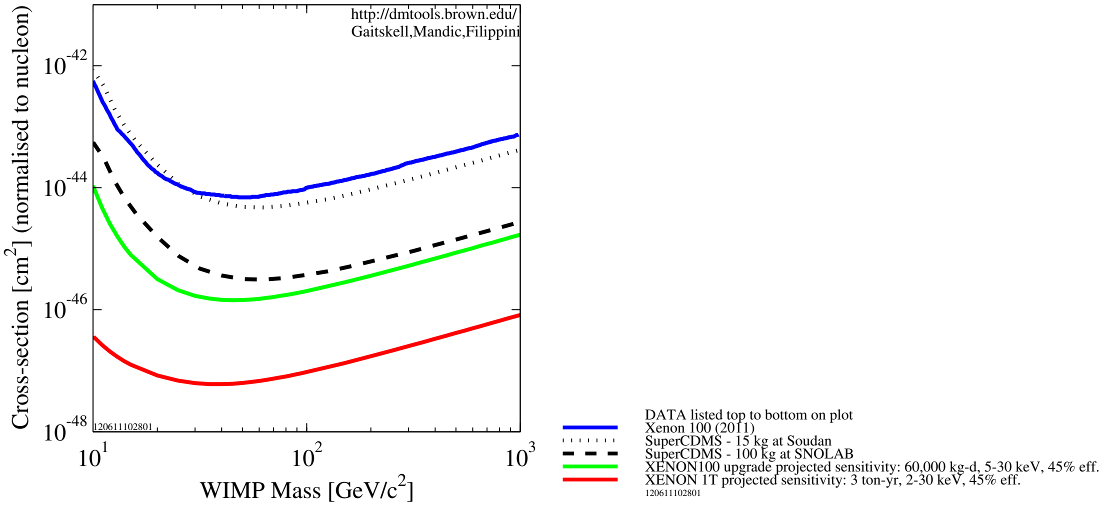

Figure 7.4: σ_{SI} sensitivity of Xenon 100 [104], SuperCDMS[140], Xenon upgrade and Xenon1T [141]. Plot made using DMTools [142].

a treatment of the implications for supersymmetric theories. Theories with Lightest Supersymmetric Partners as candidate WIMPs will have to evade these new limits.

7.3 Low mass dark matter

Direct detection experiments DAMA/Libra and COGENT have reported 8 σ and greater annular modulation signals at relatively low dark matter masses of a few GeV. These results are actually excluded by low/no background experiments like CDMS and Xenon. Annual modulation experiments expect background in their measurements but depend on the annual sinusoidal change in the WIMP-nucleon scattering to distinguish the signal as the earth goes in a direction parallel or anti-parallel to the sun through the DM halo. Unfortunately, there may be sources of background that change seasonally with the signal. There have been proposals to lower a NaI 250 kg detector into the IceCube array where seasonal changes in the background would be out of phase with the Northern hemisphere [148] and could confirm or deny the DAMA/Libra results.

However, there remains significant theoretical interest in non-traditional dark matter models that may explain this region of dark matter masses. In separate work, we have produced the expected neutrino fluxes for low mass dark matter particles [149]. While IceCube would not be sensitive to these fluxes, Kamland would be able to measure the electron neutrino fluxes from such light dark matter particles. Additionally, this work relaxed one of the assumptions implicit in Chapters 5 and 6: that the WIMP-nucleon cross section may be approximated as an elastic scattering cross section. The paper explores the effects of inelastic contact interactions (relevant to composite dark matter scenarios) and elastic interactions collisions mediated by a particle with a mass smaller than the momentum transfer in the elastic collision. The paper is in submission to PRD. We find that the Long-Baseline Neutrino Experiment (LBNE) could easily exceed the sensitivity of CDMS to models with inelastic collisions.

7.4 Final Remarks

The search for dark matter hopes to do nothing less than discover the nature of five out of every six units of matter in our universe. Indirect detection experiments in the past few years have begun exploring the viability of DM models with an annihilation rate today equal to that predicted for thermal production of dark matter at freeze-out. Meanwhile, direct detection experiments and neutrino telescopes such as IceCube/DeepCore are setting the world's best spin-independent and spin-dependent WIMP-nucleon scattering cross section limits. This work has pursued a DM annihilation explanation of the exciting prospect of the positron excess observed by the PAMELA satellite (Chapters 3 and 4). We have also engaged in the phenomenological preparation for a discovery of dark matter and what will eventually become a rush to discriminate among dark matter final states, which in turn may reveal the underlying dark matter model (Chapters 5 and 6). In this era of increased experimental sensitivity, formulating a model that obeys all the current bounds demands ever more creativity, and these bounds drive phenomenologists to more carefully scrutinize the assumptions surrounding substructure and the DM velocity dependence of indirect and direct detection signals (Chapter 2). With the promised improvements of future experiments, phenomenological work will continue requiring new model fits to incoming data and discovering predictive and discriminating signals in upcoming experiments.

References

[1] R. Allahverdi, B. Dutta, K. Richardson-McDaniel, and Y. Santoso, Phys.Rev. **D79**, 075005 (2009).

[2] R. Allahverdi, B. Dutta, K. Richardson-McDaniel, and Y. Santoso, Phys.Lett. **B677**, 172 (2009).

[3] R. Allahverdi, S. Bornhauser, B. Dutta, and K. Richardson-McDaniel, Phys.Rev. **D80**, 055026 (2009).

[4] R. Allahverdi and K. Richardson, Phys.Rev. **D85**, 113012 (2012).

[5] E. Komatsu *et al.* [WMAP Collaboration], Astrophys. J. Suppl. **192**, 18 (2011) [arXiv:1001.4538 [astro-ph.CO]].

[6] K. G. Begeman, A. H. Broeils, and R. H. Sanders, Mon.Not.Roy.Astron.Soc. **249**, 523 (1991).

[7] NASA, ESA, E. Jullo, P. Natarajan and J-P. Kneib. (2010). http://www.spacetelescope.org/images/heic1014a/

[8] F. Zwicky, Helv.Phys.Acta **6**, 110 (1933).

[9] M. Markevitch *et al.*, Astrophys.J. **567**, L27 (2002).

[10] M. Markevitch *et al.*, Astrophys.J. **606**, 819 (2004).

[11] C. Mastropietro and A. Burkert, Mon.Not.Roy.Astron.Soc. (2007).

[12] WMAP Science Team (2010).

[13] D. Larson, J. Dunkley, G. Hinshaw, E. Komatsu, M. R. Nolta, C. L. Bennett, B. Gold and M. Halpern *et al.*, Astrophys. J. Suppl. **192**, 16 (2011) [arXiv:1001.4635 [astro-ph.CO]].

[14] K. Hagiwara *et al.* [Particle Data Group Collaboration], B. D. Fields and S. Sarkar, Phys. Rev. D **66**, 010001 (2002).

[15] E. Kolb and M. Turner, *The Early Univers* (Addison-Wesley, 1990).

[16] M. Milgrom, Astrophys. J. **270**, 365 (1983).

[17] L. Wyrzykowski, J. Skowron, S. Kozłowski, et al. Mon.Not.Roy.Astron.Soc., 416, 2949 (2011).

[18] P. Tisserand, L. Le Guillou, C. Afonso, et al. Astron. & Astrophys., 469, 387 (2007).

[19] G. Bertone, D. Hooper and J. Silk, Phys. Rept. **405**, 279 (2005) [hep-ph/0404175].

[20] Abazajian, K. N., Calabrese, E., Cooray, A., et al. Astroparticle Physics, 35, 177 (2011).

[21] J. R. Bond, G. Efstathiou and J. Silk, Phys. Rev. Lett. **45**, 1980 (1980).

[22] P. J. E. Peebles, Astrophys. J. **277**, 470 (1984).

[23] S. Dodelson and L. M. Widrow, Phys. Rev. Lett. **72**, 17 (1994) [hep-ph/9303287].

[24] K. Abazajian, G. M. Fuller and M. Patel, Phys. Rev. D **64**, 023501 (2001) [astro-ph/0101524].

[25] L. D. Duffy and K. van Bibber, New J. Phys. **11** (2009) 105008 [arXiv:0904.3346 [hep-ph]].

[26] S. J. Asztalos *et al.* [ADMX Collaboration], Phys. Rev. Lett. **104**, 041301 (2010) [arXiv:0910.5914 [astro-ph.CO]].

[27] J. L. Feng and J. Kumar, Phys. Rev. Lett. **101**, 231301 (2008) [arXiv:0803.4196 [hep-ph]].

[28] M. Drees and G. Gerbier, arXiv:1204.2373 [hep-ph].

[29] R. Abbasi *et al.* [IceCube Collaboration], e-Print: arXiv:1112.1840 [astro-ph.HE].

[30] M. Ackermann *et al.* [LAT Collaboration], arXiv:1205.2739 [astro-ph.HE].

[31] M. Ackermann *et al.* [Fermi-LAT Collaboration], Phys. Rev. Lett. **107**, 241302 (2011) [arXiv:1108.3546 [astro-ph.HE]].

[32] O. Adriani *et al.* [PAMELA Collaboration], Nature **458**, 607 (2009) [e-Print: arXiv:0810.4995 [astro-ph]].

[33] O. Adriani, G. C. Barbarino, G. A. Bazilevskaya, R. Bellotti, M. Boezio, E. A. Bogomolov, L. Bonechi and M. Bongi *et al.*, Phys. Rev. Lett. **102**, 051101 (2009) [arXiv:0810.4994 [astro-ph]].

[34] A. A. Abdo *et al.* [Fermi LAT Collaboration], Phys. Rev. Lett. **102**, 181101 (2009) [arXiv:0905.0025 [astro-ph.HE]].

[35] R. Abbasi *et al.* [IceCube Collaboration], Phys. Rev. D **84**, 022004 (2011) [arXiv:1101.3349 [astro-ph.HE]].

[36] D. Hooper and L. Goodenough, Phys. Lett. B **697**, 412 (2011) [arXiv:1010.2752 [hep-ph]].

[37] G. Dobler, D. P. Finkbeiner, I. Cholis, T. R. Slatyer and N. Weiner, Astrophys. J. **717**, 825 (2010) [arXiv:0910.4583 [astro-ph.HE]].

[38] G. Dobler, I. Cholis and N. Weiner, Astrophys. J. **741**, 25 (2011) [arXiv:1102.5095 [astro-ph.HE]].

[39] T. Bruch, A. H. G. Peter, J. Read, L. Baudis and G. Lake, Phys. Lett. B **674**, 250 (2009) [arXiv:0902.4001 [astro-ph.HE]].

[40] I. Cholis and L. Goodenough, JCAP **1009**, 010 (2010) [arXiv:1006.2089 [astro-ph.HE]].

[41] A. Sommerfeld, Annalen der Physik, **403**, 257 (1931).

[42] M. Cirelli, M. Kadastik, M. Raidal and A. Strumia, Nucl. Phys. B **813**, 1 (2009) [arXiv:0809.2409 [hep-ph]].

[43] J. L. Feng, M. Kaplinghat and H. -B. Yu, Phys. Rev. Lett. **104**, 151301 (2010) [arXiv:0911.0422 [hep-ph]].

[44] S. Campbell and B. Dutta, Phys. Rev. D **84**, 075004 (2011) [arXiv:1106.4621 [astro-ph.HE]].

[45] X. -l. Chen, M. Kamionkowski and X. -m. Zhang, Phys. Rev. D **64**, 021302 (2001) [astro-ph/0103452].

[46] M. Fornasa, J. Zavala, M. A. Sanchez-Conde, F. Prada and M. Vogelsberger, arXiv:1110.0324 [astro-ph.CO].

[47] X. Huang, G. Vertongen and C. Weniger, JCAP **1201**, 042 (2012) [arXiv:1110.1529 [hep-ph]].

[48] A. Geringer-Sameth and S. M. Koushiappas, Phys. Rev. Lett. **107**, 241303 (2011) [arXiv:1108.2914 [astro-ph.CO]].

[49] D. Hooper, M. Kaplinghat, L. E. Strigari and K. M. Zurek, Phys. Rev. D **76**, 103515 (2007) [arXiv:0704.2558 [astro-ph]].

[50] T. R. Slatyer, N. Toro and N. Weiner, arXiv:1107.3546 [hep-ph].

[51] W. B. Lin, D. H. Huang, X. Zhang and R. H. Brandenberger, Phys. Rev. Lett. **86**, 954 (2001) [astro-ph/0009003].

[52] A. L. Erickcek and K. Sigurdson, Phys. Rev. D **84**, 083503 (2011) [arXiv:1106.0536 [astro-ph.CO]].

[53] E. Komatsu *et al.* [WMAP Collaboration], Astrophys. J. Suppl. **180**, 330 (2009) [arXiv:0803.0547 [astro-ph]].

[54] J.R. Ellis, J.S. Hagelin, D.V. Nanopoulos, K.A. Olive and M. Srednicki, Nucl. Phys. B **238**, 453 (1984).

[55] J. Chang, *et al.*, Nature 456, 362 (2008).

[56] S. Torii, *et al.*, arXiv:0809.0760.

[57] D. Hooper, P. Blasi and P.D. Serpico, arXiv:0810.1527.

[58] V. Barger, W. Y. Keung, D. Marfatia and G. Shaughnessy, Phys. Lett. B **672**, 141 (2009) [arXiv:0809.0162 [hep-ph]].

[59] L. Bergstrom, T. Bringmann and J. Edsjo, Phys. Rev. D **78**, 103520 (2008) [arXiv:0808.3725 [astro-ph]].

[60] N. Afshordi, R. Mohayaee and E. Bertschinger, Phys. Rev. D **79**, 083526 (2009) [arXiv:0811.1582 [astro-ph]].

[61] F. Donato, D. Maurin, P. Brun, T. Delahaye and P. Salati, Phys. Rev. Lett. **102**, 071301 (2009) [arXiv:0810.5292 [astro-ph]].

[62] N. Arkani-Hamed, D. P. Finkbeiner, T. R. Slatyer and N. Weiner, Phys. Rev. D **79**, 015014 (2009) [arXiv:0810.0713 [hep-ph]].

[63] P. Grajek, G. Kane, D.J. Phalen, A. Pierce and S. Watson, arXiv:0807.1508; M. Pospelov and A. Ritz, arXiv:0810.1502; I. Cholis, D.P. Finkbeiner, L. Goodenough and N. Weiner, arXiv:0810.5344; J.H. Huh, J.E. Kim and B. Kyae, arXiv:0809.2601; M. Fairbairn and J. Zupan, arXiv:0810.4147; A.E. Nelson and C. Spitzer, arXiv:0810.5167; D. Feldman, Z. Liu and P. Nath, arXiv:0810.5762; Y. Nomura and J. Thaler, arXiv:0810.5397; K. Ishiwata, S. Matsumoto and T. Moroi, arXiv:0811.0250; P.J. Fox and E. Poppitz, arXiv:0811.0399; R. Harnik and G.D. Kribs, arXiv:0810.5557; C.R. Chen, F. Takahashi and T.T. Yanagida, arXiv:0811.0477; S. Baek and P. Ko, arXiv:0811.1646.

[64] C.R. Chen, M.M. Nojiri, F. Takahashi and T.T. Yanagida, arXiv:0811.3357; K. Hamaguchi, E. Nakamura, S. Shirai and T.T. Yanagida, arXiv:0811.0737; P.f. Yin, Q. Yuan, J. Liu, J. Zhang, X.j. Bi and S.h. Zhu, arXiv:0811.0176; A. Ibarra and D. Tran, arXiv:0811.1555.

[65] I. Cholis, G. Dobler, D. P. Finkbeiner, L. Goodenough and N. Weiner, Phys. Rev. D **80**, 123518 (2009) [arXiv:0811.3641 [astro-ph]].

[66] R. N. Mohapatra and R. E. Marshak, Phys. Rev. Lett. **44**, 1316 (1980) [Erratum-ibid. **44**, 1643 (1980)].

[67] R. Allahverdi, A. Kusenko and A. Mazumdar, JCAP **0707**, 018 (2007) [e-Print: hep-ph/0608138].

[68] R. Allahverdi, B. Dutta and A. Mazumdar, Phys. Rev. Lett. **99**, 261301 (2007) [e-Print: arXiv:0708.3983 [hep-ph]].

[69] S. Khalil and H. Okada, arXiv:0810.4573 [hep-ph]; S. Khalil and A. Masiero, Phys. Lett. B **665**, 374 (2008).

[70] T. Aaltonen *et al.* [CDF Collaboration], Phys. Rev. Lett. **99**, 171802 (2007). [arXiv:0707.2524 [hep-ex]].

[71] M. S. Carena, A. Daleo, B. A. Dobrescu and T. M. P. Tait, Phys. Rev. D **70**, 093009 (2004) [arXiv:hep-ph/0408098].

[72] M. Kawasaki, K. Kohri and T. Moroi, Phys. Rev. D **71**, 083502 (2005).

[73] P. Gondolo, J. Edsjo, P. Ullio, L. Bergstrom, M. Schelke and E.A. Baltz, JCAP **0407**, 008 (2004).

[74] E.A. Baltz and J. Edsjo, Phys. Rev. D **59**, 023511 (1999).

[75] J.F. Navarro, C.S. Frenk and S.D.M. White, Astrophys. J. **462**, 563 (1996).

[76] T. Delahaye, R. Lineros, F. Donato, N. Fornengo and P. Salati, Phys. Rev. D **77**, 063527 (2008).

[77] T.G. Guzik, *et al.*, in ICRC 2007 Proceedings.

[78] I. Hinchliffe, F.E. Paige, M.D. Shapiro, J. Soderqvist and W. Yao, Phys. Rev. D **55**, 5520 (1997).

[79] H. Goldberg, Phys. Rev. Lett. **50** (1983) 1419.

[80] S. Profumo, arXiv:0812.4457.

[81] W. de Boer, arXiv:0901.2941.

[82] J. Hisano, M. Kawasaki, K. Kohri, T. Moroi and K. Nakayama, Phys. Rev. D **79**, 083522 (2009) [arXiv:0901.3582 [hep-ph]].

[83] T.E. Jeltema, J. Kehayias and S. Profumo, arXiv:0812.0597; P. Meade, M. Papucci and T. Volansky, arXiv:0901.2925.

[84] J. Hisano, M. Kawasaki, K. Kohri and K. Nakayama, arXiv:0812.0219.

[85] J. Yoo [CDMS Collaboration], arXiv:0810.3527.

[86] L. Baudis, arXiv:0711.3788; T. Saab, talk at Dark2009 Conference, Christchurch, New Zealand.

[87] J. R. Ellis, G. Ridolfi and F. Zwirner, Phys. Lett. B **257**, 83 (k1991); R. Arnowitt and P. Nath, Phys. Rev. D **46**, 3981 (1992).

[88] Y. Fukuda *et al.* [Super-Kamiokande Collaboration], Phys. Rev. Lett. **81**, 1562 (1998), hep-ex/9807003.

[89] S. P. Martin, Phys. Rev. D **54**, 2340 (1996) [arXiv:hep-ph/9602349].

[90] B. Dutta, L. Leblond and K. Sinha, arXiv:0904.3773 [hep-ph].

[91] G. Jungman, M. Kamionkowski and K. Griest, Phys. Rept. **267** (1996) 195 [arXiv:hep-ph/9506380].

[92] C. Delaunay, P. J. Fox and G. Perez, JHEP **0905**, 099 (2009).

[93] A. Rizzo [IceCube Collaboration], "Search For Neutralino Dark Matter With The Amanda Neutrino Telescope And Prospects For Icecube," *In *Heidelberg 2007, Dark matter in astroparticle and particle physics* 122-131*

[94] M. Ackermann *et al.* [AMANDA Collaboration], Astropart. Phys. **24** (2006) 459 [arXiv:astro-ph/0508518].

[95] M. Blennow, J. Edsjo and T. Ohlsson, JCAP **0801** (2008) 021 [arXiv:0709.3898 [hep-ph]].

[96] Gould, A. 1987, Ap.J., 321, 571

[97] C. De Clercq for the IceCube Collaboration, "Search for Dark Matter with the AMANDA and IceCube Neutrino Detectors", Presented at the Identification of Dark Matter 2008, Stockholm, Sweden, 18-22 August 2008; Proceedings of Science PoS (idm2008) 034.

[98] R. Abbasi *et al.* [ICECUBE Collaboration], Phys. Rev. Lett. **102** (2009) 201302 [arXiv:0902.2460].

[99] J. I. Read, G. Lake, O. Agertz and V. P. Debattista, arXiv:0803.2714 [astro-ph].

[100] J. I. Read, L. Mayer, A. M. Brooks, F. Governato and G. Lake, arXiv:0902.0009 [astro-ph.GA].

[101] J. Ellis, K. Olive, Y. Santoso, and V. Spanos, Phys. Lett. B**565**, 176 (2003); R. Arnowitt, B. Dutta, and B. Hu, arXiv:hep-ph/0310103; H. Baer, C. Balazs, A. Belyaev, T. Krupovnickas, and X. Tata, JHEP **0306**, 054 (2003); B. Lahanas and D.V. Nanopoulos, Phys. Lett. B**568**, 55 (2003); U. Chattopadhyay, A. Corsetti, and P. Nath, Phys. Rev. D**68**, 035005 (2003); E. Baltz and P. Gondolo, JHEP **0410**, 052 (2004).

[102] F. Jegerlehner and A. Nyffeler, Phys. Rept. **477**, 1 (2009) [arXiv:0902.3360 [hep-ph]].

[103] H. Baer, A. Belyaev, T. Krupovnickas and J. O'Farrill, JCAP **0408**, 005 (2004) [e-Print: hep-ph/0405210].

[104] E. Aprile *et al.* [XENON100 Collaboration], Phys. Rev. Lett. **107**, 131302 (2011) [e-Print: arXiv:1104.2549 [astro-ph.CO]].

[105] M. Honda, T. Kajita, K. Kasahara, S. Midorikawa and T. Sanuki, Phys. Rev. D **75**, 043006 (2007) [e-Print: astro-ph/0611418].

[106] R. Abbasi *et al.* [IceCube Collaboration], Phys. Rev. D **83**, 012001 (2011) [e-Print: arXiv:1010.3980 [astro-ph.HE]].

[107] J.D. Zornoza, D. Chirkin, "Muon energy reconstruction and atmospheric neutrino spectrum unfolding with the IceCube detector", in Proc. of 30th ICRC (2007).

[108] R. Abbasi *et al.* [IceCube Collaboration], e-Print: arXiv:1111.2731 [astro-ph.IM].

[109] T. DeYoung [for the IceCube Collaboration], e-Print: arXiv:1112.1053 [astro-ph.HE].

[110] J. R. Ellis, T. Falk and K. A. Olive, Phys. Lett. B **444**, 367 (1998) [e-Print: hep-ph/9810360]; J. R. Ellis, T. Falk, K. A. Olive and M. Srednicki, Astropart. Phys. **13**, 181 (2000) [e-Print: hep-ph/9905481]; M. E. Gomez, G. Lazarides and C. Pallis, Phys. Rev. D **61**, 123512 (2000) [e-Print: hep-ph/9907261]; M. E. Gomez, G. Lazarides and C. Pallis, Phys. Lett. B **487**, 313 (2000) [e-Print: hep-ph/0004028]; A. B. Lahanas, D. V. Nanopoulos and V. C. Spanos, Phys. Rev. D **62**, 023515 (2000) [e-Print: hep-ph/9909497]; R. L. Arnowitt, B. Dutta and Y. Santoso, Nucl. Phys. B **606**, 59 (2001) [e-Print: hep-ph/0102181].

[111] K. L. Chan, U. Chattopadhyay and P. Nath, Phys. Rev. D **58**, 096004 (1998) [e-Print: hep-ph/9710473]; J. L. Feng, K. T. Matchev and T. Moroi, Phys. Rev. Lett. **84**, 2322 (2000) [e-Print: hep-ph/9908309]; J. L. Feng, K. T. Matchev and T. Moroi, Phys. Rev. D **61**, 075005 (2000) [e-Print: hep-ph/9909334]; H. Baer, C.-h. Chen, F. Paige and X. Tata, Phys. Rev. D **52**, 2746 (1995) [e-Print: hep-ph/9503271]; H. Baer, C.-h. Chen, F. Paige and X. Tata, Phys. Rev. D **53**, 6241 (1996) [e-Print: hep-ph/9512383]; H. Baer, C.-h. Chen, M. Drees, F. Paige and X. Tata, Phys. Rev. D **59**, 055014 (1999) [e-Print: hep-ph/9809223].

[112] R. C. Cotta, K. T. K. Howe, J. L. Hewett and T. G. Rizzo, [e-Print: arXiv:1105.1199 [hep-ph]]; J. Ellis, K. A. Olive, C. Savage and V. C. Spanos, Phys. Rev. D **81**, 085004 (2010) [e-Print: arXiv:0912.3137 [hep-ph]]; J. Ellis, K. A. Olive, C. Savage and V. C. Spanos, Phys. Rev. D **83**, 085023 (2011) [e-Print: arXiv:1102.1988 [hep-ph]].

[113] M. Lindner, A. Merle and V. Niro, Phys. Rev. D **82**, 123529 (2010) [e-Print: arXiv:1005.3116 [hep-ph]].

[114] Y. Farzan, S. Pascoli and M. A. Schmidt, JHEP **1010**, 111 (2010) [e-Print: arXiv:1005.5323 [hep-ph]]; Y. Farzan, Phys. Rev. D **80**, 073009 (2009) [e-Print: arXiv:0908.3729 [hep-ph]]; C. Boehm, Y. Farzan, T. Hambye, S. Palomares-Ruiz and S. Pascoli, Phys. Rev. D **77**, 043516 (2008) [e-Print: hep-ph/0612228].

[115] R. Abbasi *et al.* [IceCube Collaboration], arXiv:1111.2738 [astro-ph.HE].

[116] R. Allahverdi, B. Dutta and R. Mohapatra, Phys. Lett. B **695**, 181 (2011) [e-Print: arXiv:1008.1232 [hep-ph]].

[117] A. E. Erkoca, G. Gelmini, M. H. Reno and I. Sarcevic, Phys. Rev. D **81**, 096007 (2010) [e-Print: arXiv:1002.2220 [hep-ph]]; R. Allahverdi, S. Campbell and B. Dutta, Phys. Rev. D (in press)) [e-Print: arXiv: 1110.6660 [hep-ph]].

[118] M. Cirelli, N. Fornengo, T. Montaruli, I. A. Sokalski, A. Strumia, F. Vissani, Nucl. Phys. B **727**, 99 (2005) [Erratum-ibid. B 790, 338 (2008)] [e-Print: hep-ph/0506298].

[119] G. Giordano, O. Mena and I. Mocioiu, Phys. Rev. D **81**, 113008 (2010) [e-Print: arXiv:1004.3519 [hep-ph]].

[120] E. Middell, J. McCartin and M. DAgostino for the IceCube Collaboration, "Improved Reconstruction of Cascade-like Events in IceCube," Proceedings of the 31st International Cosmic Ray Conference, 2009.

[121] K. Abe *et al.* [T2K Collaboration], Phys. Rev. Lett. **107**, 041801 (2011) [arXiv:1106.2822 [hep-ex]].

[122] P. Adamson *et al.* [MINOS Collaboration], Phys. Rev. Lett. **107**, 181802 (2011) [arXiv:1108.0015 [hep-ex]].

[123] T. Tanaka *et al.* [Super-Kamiokande Collaboration], Astrophys. J. **742**, 78 (2011) [e-Print: arXiv:1108.3384 [astro-ph.HE]].

[124] A. de Gouvea, A. Friedland and H. Murayama, Phys. Rev. D **60**, 093011 (1999) [e-Print: hep-ph/9904399].

[125] A. Esmaili and Y. Farzan, JCAP **1104**, 007 (2011) [e-Print: arXiv:1011.0500 [hep-ph]]; Y. Farzan, e-Print: arXiv:1111.1063 [hep-ph].

[126] K. Nakamura *et al.* [Particle Data Group], J. Phys. G **37**, 075021 (2010).

[127] A. Cooper-Sarkar and S. Sarkar, JHEP **0801**, 075 (2008) [e-Print: arXiv:0710.5303 [hep-ph]].

[128] V. Barger, Y. Gao, W. Y. Keung, D. Marfatia and G. Shaughnessy, Phys. Lett. B **678**, 283 (2009) [arXiv:0904.2001 [hep-ph]].

[129] L. Gendelev, S. Profumo and M. Dormody, JCAP **1002**, 016 (2010) [arXiv:1001.4540 [astro-ph.HE]].

[130] C. Evoli, I. Cholis, D. Grasso, L. Maccione and P. Ullio, arXiv:1108.0664 [astro-ph.HE].

[131] F. Aharonian *et al.* [H.E.S.S. Collaboration], Astron. Astrophys. **508**, 561 (2009) [arXiv:0905.0105 [astro-ph.HE]].

[132] M. Ackermann *et al.* [Fermi LAT Collaboration], Phys. Rev. Lett. **108**, 011103 (2012) [arXiv:1109.0521 [astro-ph.HE]].

[133] D. Hooper, A. V. Belikov, T. E. Jeltema, T. Linden, S. Profumo and T. R. Slatyer, arXiv:1203.3547 [astro-ph.CO].

[134] T. E. Jeltema and S. Profumo, arXiv:1108.1407 [astro-ph.HE].

[135] P. A. R. Ade *et al.* [Planck Collaboration], Astron. Astrophys. **536** (19??) [arXiv:1101.2024 [astro-ph.CO]].

[136] B. Dasgupta and R. Laha, arXiv:1206.1322 [hep-ph].

[137] T. Bruch and f. t. C. Collaboration, arXiv:1001.3037 [astro-ph.IM].

[138] L. Baudis and f. t. X. Collaboration, arXiv:1203.1589 [astro-ph.IM].

[139] E. Aprile [XENON Collaboration], astro-ph/0502279.

[140] Akerib, D. S., Attisha, M. J., Bailey, C. N., et al. 2006, Nuclear Instruments and Methods in Physics Research A, 559, 411

[141] Kaixuan Ni, private communication 16 May (2009).

[142] dmtools.brown.edu (2012).

[143] M. Pieri [CMS Collaboration], arXiv:1205.2907 [hep-ex].

[144] P. Mal [for ATLAS Collaboration], arXiv:1206.1174 [hep-ex].

[145] S. A. Koay and C. Collaboration, arXiv:1202.1000 [hep-ex].

[146] O. Igonkina, arXiv:1201.5886 [hep-ex].

[147] H. Baer, V. Barger, P. Huang and X. Tata, JHEP **1205**, 109 (2012) [arXiv:1203.5539 [hep-ph]].

[148] J. Cherwinka, R. Co, D. F. Cowen, D. Grant, F. Halzen, K. M. Heeger, L. Hsu and A. Karle *et al.*, Astropart. Phys. **35**, 749 (2012) [arXiv:1106.1156 [astro-ph.HE]].

[149] J. Kumar, J. G. Learned, S. Smith and K. Richardson, arXiv:1204.5120 [hep-ph].